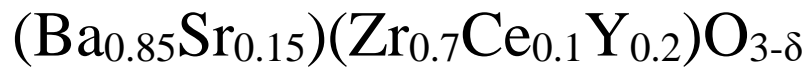


Sintering Behavior and Conductivity of



Doped with ZnO as Sintering Aid

Henry Chen



M.Sc. Thesis

Materials Science for Energy and Nanotechnology

60 credits

Department of Chemistry

Faculty of Mathematics and Natural Sciences

UNIVERSITY OF OSLO

May 2022

© Henry Chen

2022

Sintering Behavior and Conductivity of $(\text{Ba}_{0.85}\text{Sr}_{0.15})(\text{Zr}_{0.7}\text{Ce}_{0.1}\text{Y}_{0.2})\text{O}_{3-\delta}$

Doped with ZnO as Sintering Aid

Henry Chen

<http://www.duo.uio.no/>

Printed: Reprosentralen, University of Oslo

Acknowledgements

This thesis constitutes part of the required work for the master's degree in Materials Science for Energy and Nanotechnology at the Department of Chemistry, University of Oslo. The work was accomplished in the period between August 2021 and May 2022 at the Electrochemistry Group, part of the Centre for Materials Science and Nanotechnology.

I would first like to thank my supervisors Professor Truls Norby, Professor Reidar Haugrud, and Dr. Amir Masoud Dayaghi. Your guidance and insightful feedback pushed me to sharpen my thinking and brought my work to a higher academic level. I would particularly like to distinguish my supervisor Dr. Amir Masoud Dayaghi. I am grateful to you for your patient support and encouragement throughout my work.

In addition, I would like to acknowledge the people at the Group of Electrochemistry for their guidance. I must thank Stine Roen for helpful discussions in the time when I selected my master project. Thank you, Haider Abbas and Sjur Storhaug, your company in the last two years is greatly appreciated. To Jan and Elisabeth, there's no words needed, thank you guys.

Finally, I would like to thank my parents and sister for their wise counsel and sympathetic ear. You are always there for me.

May 2022

Henry Chen

Summary

This master thesis reports the research on proton-conducting ceramics based on yttria doped barium zirconate.

The yttria doped barium zirconate was doped with Sr and Ce substitutions to obtain the base material $(\text{Ba}_{0.85}\text{Sr}_{0.15})(\text{Zr}_{0.7}\text{Ce}_{0.1}\text{Y}_{0.2})\text{O}_{3-\delta}$ improving the performance of proton-conducting ceramics in a fuel cell. In this thesis, the sintering of the proton-conducting ceramics and its properties are studied. Our approach is to modify experimental conditions to tailor the crystal microstructure for desired properties. More specifically, 1) use yttria-stabilized zirconia instead of ZrO_2 as precursor 2) dope with 2 mol% ZnO as sintering aid, 3) adjust particle size by varying ball-milling parameters, 4) adjust sintering profiles, and 5) adjust oxygen and water partial pressures.

Four different batches were synthesized according to the adjustments mentioned above. Sample pellets were fabricated from these using solid state reactive sintering. Morphological studies were done by scanning electron microscopy, the physical properties were studied by X-ray diffraction, dilatometry, thermal gravimetric analysis and high-temperature X-ray diffraction, and the conductivity were studied by electrochemical impedance spectroscopy and electromotive force measurements.

A phenomenon termed “the sintering shoulder” were observed at the heating stages of the sintering process, which may have a negative effect due to excessive shrinkage and expansion of the sample. The cause of this sintering shoulder has been discussed and concluded due to ZrO_2 transitioning from monoclinic to tetragonal phase at 1200 °C. By using yttria-stabilized zirconia instead of ZrO_2 in $(\text{Ba}_{0.85}\text{Sr}_{0.15})(\text{Zr}_{0.7}\text{Ce}_{0.1}\text{Y}_{0.2})\text{O}_{3-\delta}$ the sintering shoulder is eliminated resulting in less strain and stress on the sample pellets during the sintering. By further doping with 2 mol% ZnO as sintering aid, the success rate of sintering green bodies was increased significantly, even when using more effective sintering profiles with lower sintering temperatures and a shorter sintering time (1600 °C, 1500 °C and 1400 °C for 12 hours). By using yttria-stabilized zirconia instead of ZrO_2 the activation energy for proton transport is lowered at temperatures of 100-350 °C from 0.621 eV to 0.585 eV, doping with ZnO further lowers the activation energy to 0.559 eV. The conductivity is increased for samples with yttria-stabilized zirconia, however further doping with ZnO as sintering aid lowered the conductivity due to

relatively lower hydration rates. Transport number for ions in $(\text{Ba}_{0.85}\text{Sr}_{0.15})(\text{Zr}_{0.7}\text{Ce}_{0.1}\text{Y}_{0.2})\text{O}_{3-\delta}$ were found to be $t_i \approx 1$. High-temperature X-ray diffraction measurements showed a negative thermal expansion coefficient, which was not expected for this kind of materials. Due to the limitation of the facility during this thesis project, the verification of the negative thermal expansion coefficient will have to be investigated in more detail by the next master project.

List of Abbreviations

GHG – Green House Gas

COP – Conference of the Parties

GW – Giga Watt

PCFC – Protonic Ceramic Fuel Cell

SOFC – Solid Oxide Fuel Cells

PCC – Proton-Conducting Ceramics

PCE – Proton-Conducting Electrolyte

BZY – Yttria-doped Barium Zirconate

YSZ – Yttria-Stabilized Zirconia

XRD – X-ray Diffraction

PXRD – Powder X-ray Diffraction

HT-XRD – High-Temperature X-ray Diffraction

HT-PXRD – High-Temperature Powder X-ray Diffraction

SEM – Scanning Electron Microscopy

ETD – Everhart-Thornley Detectors

BSE – Back Scatter Electrons

SE – Secondary Electrons

EDS – energy dispersive X-ray spectroscopy

Wt% – Weight Percentage

HArMix – 5% Hydrogen and Argon Mixture

TEC – Thermal Expansion Coefficient

SSRS – Solid-State Reactive Sintering

PM – Planetary Mill

RM – Roll Mill

BSZCY151020 – $(\text{Ba}_{0.85}\text{Sr}_{0.15})(\text{Zr}_{0.7}\text{Ce}_{0.1}\text{Y}_{0.2})\text{O}_{3-\delta}$

SUT – Sample Under Test

Table of Contents

1 INTRODUCTION	1
1.1 The Era for Energy Revolution	1
1.2 Hydrogen as Energy Carrier	2
1.3 Proton Ceramic Fuel Cell	4
1.4 Current State of the Arts by Literature Review and Objectives of the Project	6
1.4.1 Tailoring TEC of Proton-Conducting Ceramics	6
1.4.2 Increased Sintering Ability by Ce Dopant	7
1.4.3 Increased Proton Conductivity and Chemical Stability	7
1.4.4 Objectives of the Project	8
2 THEORY	9
2.1 Perovskite Structure	9
2.2 Defect Chemistry	10
2.2.1 Kröger-Vink Notation for Point Defects	11
2.2.2 Defect Equilibrium Coefficient	12
2.2.3 Atmospheric Dependency of Defect Formation in BSZCY151020 ($\text{Ba}_{0.85}\text{Sr}_{0.15}$)($\text{Zr}_{0.7}\text{Ce}_{0.1}\text{Y}_{0.2}$) $\text{O}_{3-\delta}$	14
2.2.4 Brouwer Diagram	17
2.3 Conductivity in Oxides	19
2.3.1 Electronic Conductivity	19
2.3.2 Ionic Conductivity	20
2.3.3 Total Conductivity	21
2.3.3 Temperature Dependency of Conductivity	21
2.4 Electrochemical Impedance Spectroscopy (EIS)	23
2.4.1 Impedance	24
3 EXPERIMENTAL SETUP	28
3.1 Ball Mill for Grinding and Mixing Materials	28
3.2 Muffle Furnace for High Temperature Experiments	28

3.3 Dilatometer for Investigation of Sintering Process	29
3.4 X-Ray Diffraction for the Crystallographic Study	30
3.5 Thermal Gravimetric Analysis for Water Uptake study	31
3.6 Scanning Electron Microscopy for Surface Morphology Study	32
3.7 Gas Mixer for Providing Specific Atmosphere	33
3.8 ProboStat for Measurement at High Temperature and Controlled Atmosphere	34
4 TECHNICAL APPROACHES AND EXPERIMENTAL PROCEDURES	36
4.1 Synthesis and Fabrication of PCCs	36
4.2 Investigation of Physical Properties	40
4.2.1 Dilatometer Experiment	40
4.2.2 XRD	41
4.2.3 Thermal Gravimetric Analysis	43
4.3 Morphological study	45
4.4 Electrochemical performance study	46
4.4.1 EIS	46
4.4.2 Transport Number Measurement by Electromotive Force	48
5 RESULTS AND DISCUSSIONS	51
5.1 Investigation of Sintering Behavior	51
5.1.1 Sintering Shoulder Discovered by DIL Experiments	52
5.1.2 The Causes of Sintering Shoulder	53
5.1.2.1 HT-PXRD for Identifying the Phase Formation	53
5.1.2.2 BaCO ₃ Decomposition Analysis	55
5.1.2.3 The Impact of ZrO ₂ Phase Transition	56
5.1.3 Sintering Behavior After the Sintering Shoulder	56
5.1.3.1 CO ₂ Exiting due to BaCO ₃ Decomposition	58
5.1.3.2 Impact of ZnO Evaporation	58
5.1.4 Completion of Sintering Process.	59
5.1.5 Relative densities of PCCs after the sintering	62

5.2 The TEC of the PCCs.	63
5.2.1 Lattice Constants of the Samples at Room Temperature	64
5.2.2 HT-XRD and TEC	65
5.3 The conductivity of the PCCs	68
5.3.1 Defect Concentration Analysis Using TGA	68
5.3.2 Conductivity of PCCs Analyzed by EIS	72
5.3.2.1 Temperature Dependency of EIS	73
5.3.2.2 <i>pO₂</i> Dependency of EIS	75
5.3.2.3 Temperature Dependency of Conductivity	76
5.3.3 Transport Number by EMF	81
6 SUMMARIZING DISCUSSION	83
7 CONCLUSION	85
REFERENCES	86
FIGURES	89
TABLES	91

1 Introduction

In this thesis project, we will focus mostly on experimental work for developing protonic conductive ceramic electrolyte that has been a research activity for many years in the electrochemical group at University of Oslo (UiO). The application of protonic conductive ceramic electrolyte is vast, they are used in sensors, hydrogen separation membranes, steam electrolyzers, membrane reactors, and is the key material in fuel cells. In this thesis the focus will be on how we can utilize the hydrogen to decrease global warming and climate change due to fossil fuels. Therefore, the activity will directly contribute to the application of green hydrogen gas, helping the industrial green energy shift at the moment. This thesis is organized in 7 chapters. After the introduction, in chapter 2, we will present the basic theory of the material structure and properties, which will serve as the guidance for the material synthesis and optimization to meet the requirement for high performance PCFCs. In chapter 3, we describe in detail of our experimental setups and facility used in this project. Both fabrication and characterization facilities used in this project will be introduced. In chapter 4, we present the technological approaches for the investigation of PCCs. The experimental procedures are also described in detail. Followed by chapter 5, I will summarize the tremendous amounts of experimental results and make discussion on our findings in chapter 6. At the last chapter, we conclude the project work and comment on the future research tasks.

1.1 The Era for Energy Revolution

Before the 21st century, human society consumes the energy mostly in the form of fossil fuels (i.e., coal, oil, and natural gas), which are not sustainable. The use of fossil fuels generates carbon dioxide (CO₂) and other greenhouse gases (GHGs) that are the furthestmost significant drivers of global warming, leading to an increase in extreme weather events, thereby threatening human society. In addition, fossil fuel combustion emits air pollutants, such as carbon monoxide (CO), sulphur dioxide (SO₂), nitrogen oxides (NO_x), and particulate matter. Exposure to these pollutants can cause health problems and damage to aquatic life due to acid rain and ocean acidification. Current CO₂ emission data predict that irreversible damage might occur in the ecosystem if the current trajectory of GHG emissions continues.

In 2022, present time, the CO₂ concentration in the atmosphere reached a new record high. In addition, the ocean has had about 30% increase in acidity due to absorbed CO₂ [1]. As for global

warming, a new temperature record was reached on average every three years in the period from 1981 to 2019 [2]. The United Nations Paris Climate Agreement (COP21) in 2015, set a goal for the international community to limit global warming to well below 2 degrees Celsius by the end of the century. At the Glasgow climate summit last year (COP26), these ambitions were lifted further. Ensuring the transition to a society with net-zero GHG-emissions requires a fundamental change in our energy systems. This motivates us to look for alternative energy sources, which must be environment friendly, renewable, and sustainable. Harvesting solar energy, wind energy, and ocean-wave energy, as well as using biofuels are the start of an energy revolution. Academic communities across different continents have devoted vast efforts to developing technology for more efficient solutions to harvest energy and using biofuels. The European Union has targeted becoming the world's first carbon-neutral society by 2050. For example, most European countries such as Norway, Denmark, and Germany have installed large scale renewable energy capacity (hydro, wind, and solar power systems). Large hourly variations of solar and wind, as well as seasonal variations create peaks in electricity generation, which do not normally match the power demand in consumption. Therefore, periodic surplus electricity needs to be stored to maintain balance of the electrical grid load. In Norway, surplus electricity is being used to pump the water back to the reservoir so that hydroelectricity can be utilized when electricity demand is peaking. Alternatively, this surplus electricity could be stored as a chemical bond in power-to-X technology. For example, carbon-free hydrogen gas with high energy density can be produced by electrolysis. These emerging power-to-X technologies can therefore be used for storing periodic power surplus in a high energy density form of hydrogen gas, which are crucial in scaling up the use of variable renewable energy sources, as well as a valuable solution for a smart grid.

1.2 Hydrogen as Energy Carrier

Hydrogen plays a key role in the energy conversion because no carbon dioxide is emitted directly when hydrogen is used as energy. Today there are two major technologies used to produce hydrogen. "Green hydrogen" is produced from surplus renewable power, for example through the electrolysis of water. "Blue hydrogen" is produced from natural gas by cracking down its large molecules. However, neither technology for producing hydrogen has been deployed at the scale needed to reach the climate ambitions for net-zero GHG-emissions. Therefore, additional strong policy support is expected. For example, the European Commission's new hydrogen strategy targets 6 GW of electrolyzers by 2024, and 40 GW by 2030.

Some other main advantages of hydrogen versus fossil fuels are listed below.

1. In the liquid state, hydrogen is better as transportation fuel than other fuels such as gasoline, alcohols, and jet fuel [3].
2. Compared to fossil fuels, hydrogen is more versatile. At the user end, hydrogen can be transformed to useful energy forms via five different processes. Fossil fuels on the other hand, can only be converted through flame combustion [3].
3. Hydrogen's utilization efficiency is the highest when it is converted to direct useful energy forms like electrical, thermal, and mechanical. Hydrogen is in total 39% more efficient than fossil fuels [3].
4. Considering fire hazards and toxicity, hydrogen is the safest fuel [3].

Because the energy density of hydrogen is very high comparing to that of lithium-ion batteries, using hydrogen in industry and transportation is emerging. Hydrogen-powered personal cars are running on Norwegian roads, as shown in the picture below (**Fig. 1**).



Fig. 1: Picture of a hydrogen-powered car at Høvik hydrogen fueling station in Norway (pictured 09.04.2022, established in 2019)

Although there are many benefits to using hydrogen as fuel, fossil fuels are still dominating due to the technical challenges hydrogen is facing. Firstly, at room temperature and atmospheric pressure, hydrogen has a much lower energy content per unit volume relative to other fuels. As a result, the hydrogen tanks weigh much more than the hydrogen they can carry. In the hydrogen car, 2014 Toyota Mirai, a full tank only contains 5.7 wt% hydrogen [4]. Secondly, hydrogen tends to leak from tanks. This is because it diffuses into the tank material due to the small molecular size, resulting in degradation of the tank. Finally, infrastructures of producing,

storing, transporting, and selling hydrogen are insufficient compared to the already existing fossil fuel infrastructure.

The rich reserves of hydrogen on earth have a brilliant potential in the global green energy transition. For example, the hydrogen fuel cell technology has been developed for many years and advanced to the level for large scale application. With the right investment and research, hydrogen can potentially become a low cost and widely accessible alternative to fossil fuels.

1.3 Proton Ceramic Fuel Cell

Hydrogen fuel cells convert the chemical energy of hydrogen in reaction with oxygen into electricity, where the only byproducts are water and heat.

The technology progress in developing hydrogen fuel cells in recent years has brought many benefits for its applications. Firstly, hydrogen fuel cells are more efficient than combustion engines because they convert the energy in hydrogen directly to electrical energy with high efficiency, more than 60% [5]. Secondly, since the only by-products are heat and water, hydrogen fuel cells use a carbon free process and that has zero emission of GHGs. Lastly, systems using hydrogen fuel cells are relatively silent due to fewer moving parts are required.

Fuel cell consists of an anode, an electrolyte, and a cathode. The fuel cell typically consumes hydrogen and oxygen at high temperature. The working principle of fuel cells is schematically illustrated in **Fig. 2**, which are generally characterized by the kind of electrolyte employed. When a protonic ceramic electrolyte is used, fuel cells are called Protonic Ceramic Fuel Cells (PCFCs). This ceramic is typically based on BaZrO_3 doped by Y (BZY).

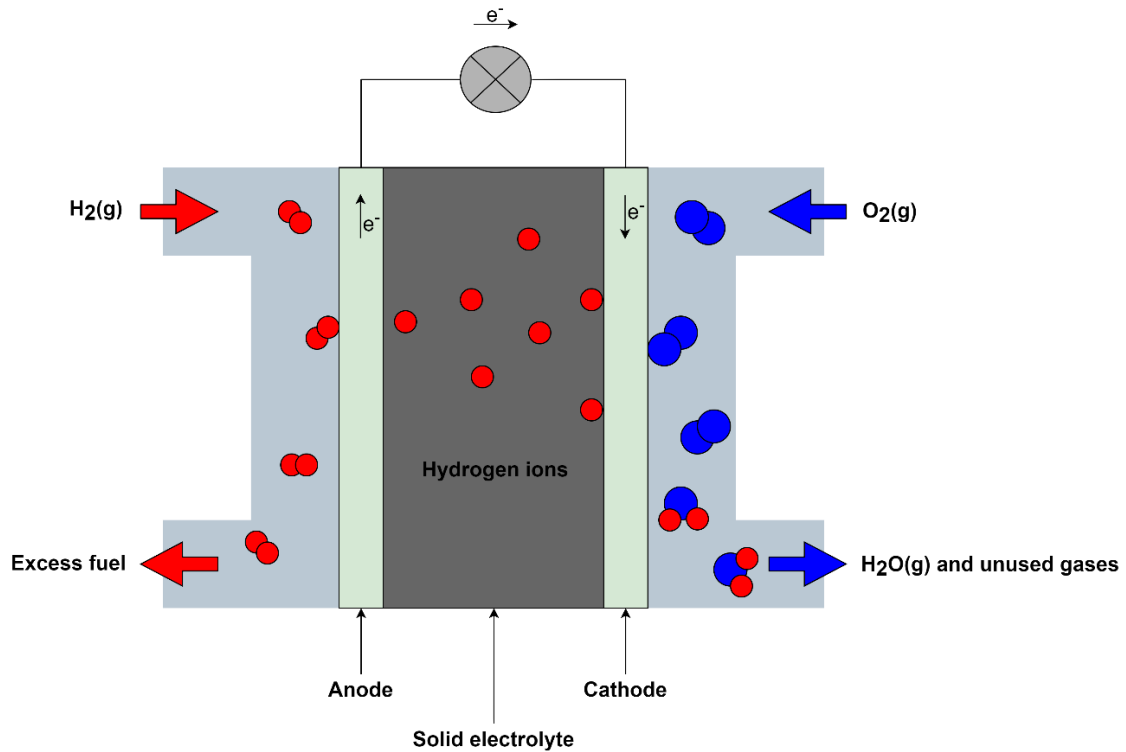
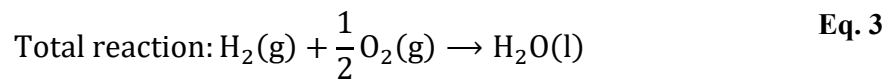
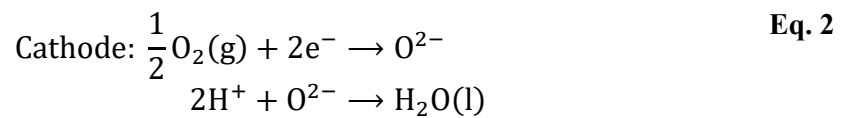
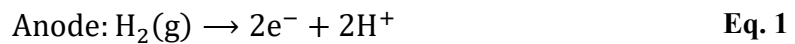


Fig. 2: Schematic of a PCFC in operation

The chemical processes in the PCFC illustrated in **Fig. 2** can be described by the following reaction equations,



During operation, hydrogen is oxidized at the anode (**Eq. 1**) [6]. Only protons migrate through the solid electrolyte to the cathode, the electrons follow through an external circuit, creating a flow of electricity. At the cathode, oxygen is reduced by taking up the electrons, following, the negatively charged oxygen ions combine with the positively charged protons to form water and emit heat (**Eq. 2**). The total reaction is shown in **Eq. 3**. Compared to the conventional SOFCs, PCFCs show advantages such as avoiding fuel dilution since water as the product forms at the “positrode” side. Most importantly, PCFCs can perform at much lower temperatures of 400-600°C without sacrificing the cell performance, this is due to protons lower enthalpy of migration compared to oxide ions [7]. This range of operating temperatures, moreover, gives the opportunity to incorporate less expensive and more conventional engineering materials.

1.4 Current State of the Arts by Literature Review and Objectives of the Project

1.4.1 Tailoring TEC of Proton-Conducting Ceramics

By using proton-conducting ceramics (PCC) many benefits are achieved, however some challenges come with it. It is well known that BZY is a good PCC, it is considered the state-of-the-art electrolyte in fuel cells. However, PCC based on BZY has a lower thermal expansion coefficient (TEC) than the supporting electrode structures in the packaged devices, which bring the problem for high-temperature application. Operating at any elevated temperatures brings the difficulty of using high-temperature sealing of ceramic, glass, and metal components due to the mismatch of the TEC between the components in the packaged device, such as proton-conducting electrolyte (PCE) and metal electrodes. The TEC mismatch phenomenon still causes degradation and shortened lifespan of the device based on PCC. Last year (2021), Dayaghi et al. attempted to reduce this mismatch by doping $\text{BaZr}_{0.8}\text{Y}_{0.2}\text{O}_{3-\delta}$ (BZY20) with Sr and Ce substitutions. $(\text{Ba}_{0.85}\text{Sr}_{0.15})(\text{Zr}_{0.7}\text{Ce}_{0.1}\text{Y}_{0.2})\text{O}_{3-\delta}$ has been sintered. The idea was to increase the TEC by modifying the composition within the stability field of the cubic structure. Both BaCeO_3 and SrZrO_3 contained by $(\text{Ba}_{0.85}\text{Sr}_{0.15})(\text{Zr}_{0.7}\text{Ce}_{0.1}\text{Y}_{0.2})\text{O}_{3-\delta}$ have higher TEC than BZY shown in **Table 1** and **Table 2** [7]. By incorporating them into BZY using partial substitution of Ba and Zr by Sr and Ce respectively, the TEC can be increased while being in the stability field of the cubic structure [8]. Dayaghi et al. report a linear TEC of $\sim 10 \times 10^{-6} \text{ K}^{-1}$ for BSZCY151020, which is higher than the linear TEC of BZY $\sim 8 \times 10^{-6} \text{ K}^{-1}$.

Table 1: Volumetric TEC of SrZrO3, BaCeO3 and BaZrO3

Material	Temperature (°C)	Volumetric TEC (10^{-5} K^{-1})	Source
SrZrO_3	0-700	3.24	[9]
BaCeO_3	27-947	3.37	[10]
BaZrO_3	0-600	2.06	[9]

Table 2: Linear TEC of SrZrO3, BaCeO3 and BaZrO3

Material	Temperature (°C)	Atmosphere	Linear TEC (10^{-6} K^{-1})	Source
SrZrO_3	25-800	-	9.7	[11]
BaCeO_3	25-800	Reducing	11.2	[9]
BaZrO_3	25-800	Reducing	7.13	[9]

1.4.2 Increased Sintering Ability by Ce Dopant

The other main challenges are long sintering time and high sintering temperatures. Conventional dense PCCs were fabricated with elevated temperatures (1700–2100 °C) and long-time sintering process (>24h), which results in a remarkably excessive cost, in addition to barium volatilization [12].

Nikodemski et al. revealed that by substituting Zr^{4+} with Ce^{4+} , the relative density of sintered pellets is significantly increased. In their work, BZY20 and $BaCe_{0.6}Zr_{0.3}Y_{0.1}O_{3-\delta}$ (BCZY63) were both sintered at 1500 °C for 12 h. The pellet without Ce had a relative density of 34.1% while the pellet with Ce had an increased relative density of 60% [12]. The SEM pictures of the two samples cross-section taken by Nikodemski et al. are shown in **Fig. 3** below.

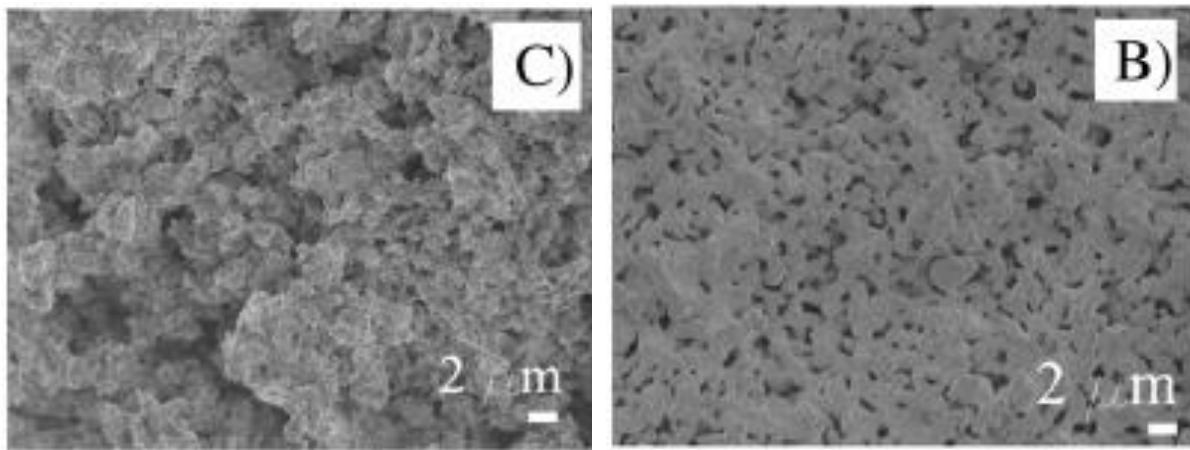


Fig. 3: C) BZY20 after sintering at 1500 °C for 12 h RD ~34.1%, B) BCZY63 after sintering at 1500 °C for 12 h RD ~60%, from the work of Nikodemski et al. [12]

1.4.3 Increased Proton Conductivity and Chemical Stability

From earlier work of Iwahara et al. (1995), it is revealed that $BaCeO_3$ show high proton conductivity, in the order $10^{-2} \frac{S}{cm}$ at 600 °C in hydrogen atmosphere [13]. However, $BaCeO_3$ is not chemically stable in reaction with CO_2 and water vapor [14]. By doping $BaCeO_3$ with acceptor dopants such as Y^{3+} the proton conductivity is increased, and by doping with Zr^{4+} the stability in CO_2 is increased. Ytria doped barium cerate was further doped with Sr on the A-site, this material showed sufficient chemical stability in water vapor rich atmospheres at 80 °C [15].

1.4.4 Objectives of the Project

In this project, by choosing the type of sintering aid, the amount of aid, and the sintering temperature as well as the preparation steps before solid-state reactive sintering (SSRS), the aim is to study the sintering behaviour of PCC and to improve the performance of PCC.

To achieve PCC with high conductivity and increased TEC, we will focus on the effect of various experimental conditions on the crystal structure and morphology, therefore, the material properties such as relative density, total conductivity, and TEC. We believe that the materials structure has a significant effect on their physical properties, especially microstructure including crystalline quality, micro/nano dimension of crystal grain size, and boundary between grains. It is well known that nanoscale materials exhibit significant size-effects due to short diffusion lengths and a high density of interfaces. The boundary thickness and stress therein as well as crystal grain distribution result in the variation of mechanical and thermal mechanical properties. Operating at an elevated temperature, the possible proton transport pathways in PCCs will be 1) bulk transportation and 2) transport along the grain boundaries. The grain boundary acts as a high impedance layer against ionic transport in polycrystalline materials. Thus, our approach will be:

1. To modify experimental conditions to tailor the crystalline microstructure and morphology for desired properties. More specific, 1) adjust concentration of dopants such as Y, 2) add ZnO as sintering aid, 3) adjust particle size by varying ball-milling parameters, 4) adjust sintering temperature and ramp patterns, 5) adjust oxygen and water partial pressures.
2. The full characterization of the as-fabricated PCCs will be conducted by scanning electron microscopy (SEM), X-ray diffraction (XRD), thermal gravimetric analysis (TGA), electromotive force (EMF) and electrochemical impedance spectroscopy (EIS) using ProboStatTM (NORECS) measurement cell under controlled atmospheres, notably p_{H_2O} , p_{Ar} , p_{O_2} , p_{H_2} , and HarMix.
3. Fabrication process will be optimized by analyzing the material structure relating to its performance from step 1 and 2.

2 Theory

In this chapter, knowledge of PCE material structure and properties supporting the main research topics of this project will be briefly introduced to guide our strategy of synthesizing the materials and optimization of the material properties.

2.1 Perovskite Structure

In this thesis work, we will investigate and improve the performance of ceramic PCEs of Perovskite structure. Therefore, more detailed knowledge of Perovskite structure chemical compounds will be briefly discussed in the following paragraph. In general, chemical compounds with Perovskite structure typically have the molecular formula of ABX_3 [16] where,

- A is often a divalent metal cation (A^{2+}), earth-alkali or rare earth-alkali element. The A cation is 12-fold coordinated with the oxygen anions.
- B is often a trivalent metal cation (B^{3+}), 3d, 4d and 5d transition metal elements. The B cation is 6-fold coordinated.
- A is the bigger cation while B is the smaller cation, $r_A > r_B$, where r_i is the ionic radii.
- X is oxygen. The X anion bonds to both cations.

In the ideal perovskite structure, the atoms are chemically bonded to each other and forms a cubic crystal system with space group $Pm\bar{3}m-O_h$ [16]. In this structure the B-O distance is equal to $\frac{a}{2}$ and the A-O distance is equal to $\frac{a}{\sqrt{2}}$ (a is the lattice constant). This results in the following relation:

$$r_A + r_O = \sqrt{2}(r_B + r_O) \quad \text{Eq. 4}$$

In reality, perovskite structures are usually pseudo-cubic and often crystallize in the orthorhombic system. Therefore, they will not follow **Eq.5** completely. The deviation from the ideal situation can be expressed by Goldschmidt's tolerance factor (t):

$$t = \frac{r_A + r_O}{\sqrt{2}(r_B + r_O)} \quad \text{Eq. 5}$$

The ideal cubic perovskite structure is still found when the t-value is close or equal to 1 ($0.75 < t < 1.0$) [16].

The perovskite structure is known for its flexibility towards non-stoichiometries and substitutions. The A and B ions can have oxidation numbers varying from 0 to 3 if $r_A > r_B$ [17]. By choosing atom (varies of A or B) used in the Perovskite structure, properties of PCE including ion conductivity can be tailored to obtain the best performance of PCFC.

2.2 Defect Chemistry

The ideal crystalline compounds having ideal periodicity in their crystal lattice are hardly found in nature and are therefore artificially fabricated. Crystalline compounds always have certain deviations from the ideal case, which is called defects in crystal materials. In defect chemistry, electronic and structural defects are involved. The electrical conductivity of the PCE depends largely on electrical and point defects. Understanding the defect formation, types, and mechanisms for charge transportation is particularly important when we optimize the PCEs.

There are four main types of structural defects in crystalline solids:

1. Point defects: they are also called zero dimensional defects that are limited to the imperfectness at one lattice or structural site and its immediate vicinity.
2. Line defects: they are formed by one-dimensional dislocation, where ions of the crystal lattice are misaligned in certain directions.
3. Plane defects: they are two-dimensional defects consisting of internal and external surfaces, stacking faults, and grain boundaries.
4. 3-dimensional defects: precipitations and inclusions of separate phases.

A material with grain boundary is called a polycrystalline compound that in other words is formed by multi-grains of the single crystalline compound. In general, both crystalline and polycrystalline compounds have varying defects including point defects (vacancies and interstitials), line defects (dislocations), surface defects, and three-dimensional volume defects. Furthermore, crystals can also have electronic defects which can arise in association with point defects or when valence electrons are excited internally. In a crystalline compound under elevated temperatures, some electrons depending on the temperature are thermally released from lowest occupied energy states to higher energy states. From a bonding structure point of view, the thermal excited electron escapes from the chemical bond, which results in an electron without bond confinement and an electron deficient bond. The escaped electron is called a free electron and the electron deficient bond is called a hole. Both the free electron and the hole can move in the crystalline compound structure driven by diffusion and electrical field. The

presence of structural and electrical defects can give rise to many interesting properties of a crystalline compound, such as enhanced conductivity in crystals contributed by ions (ionic conductivity), electron and holes (electronic conductivity). It is also well known that electronic defects are responsible for optical properties.

2.2.1 Kröger-Vink Notation for Point Defects

Kröger-Vink notation is the most widely used system for describing point defects, constituent atoms and charges in a crystal lattice. The types of structural point defects that can exist in the crystal structure are illustrated in **Fig. 4** below.

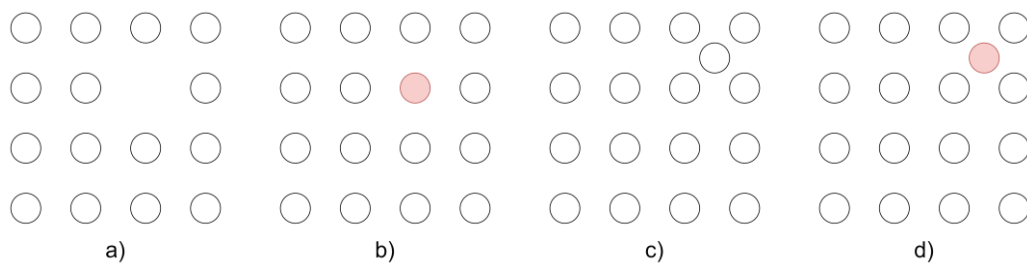


Fig. 4: a) Vacancy, b) substitutional defect, c) host interstitial defect and d) foreign interstitial defect.

All defects shown in **Fig. 4** and electronic defects can be presented by the notation system, A_S^C where,

- **A** tells us what the defect entity is. A can be:
 - Ions of Zr, Y, O or M for metal.
 - Vacancy denoted by v
 - Interstitial denoted by i
 - Electron denoted by e
 - Electron hole denoted by h
- **S** tells us where the entity is in the crystalline. For example:
 - Ion or atom site of Zr, Y or O
 - Interstitial site denoted by i
- **C** tells us about the effective charge of the species. C are denoted as:
 - \cdot for positive effective charge
 - $'$ for negative effective charge
 - \times for neutral effective charge

Defect concentrations are denoted with brackets such as $[A_S^C]$, except electron and electron hole concentrations which are denoted by n and p respectively. The density of states for electrons and electron holes are denoted as N_C and N_V respectively.

Defect concentration varies with temperature and partial pressures of gases in the atmosphere such as p_{O_2} , p_{H_2O} and p_{H_2} . This is understood by combining defect equilibrium coefficient expressions and electroneutrality conditions.

2.2.2 Defect Equilibrium Coefficient

The defect equilibrium coefficient is used to describe chemical reactions involving defects. To balance these reaction equations, the following three rules are applied.

1. **Mass balance** (conservation of mass): the equations must be balanced with respect to mass i.e., the types and amount of atoms that are taking part in a defect reaction must remain the same before and after defect formation or annihilation. Vacancies and electronic defects do not count in the mass balance.
2. **Charge balance** (conservation of charge): all materials are electrically neutral, to maintain electron neutrality the total effective charge must remain constant during the formation of defects.
3. **Site ratio balance** (conservation of the host structure): the ratio between the number of regular anion and cation sites must be constant. Interstitial sites are not lattice sites and do not count in the site ratio balance.

At an equilibrium condition, the chemical reaction is often characterized by the ratio between concentration of reactants and concentration of products, which is also known as the equilibrium coefficient, K . The K value varies with temperature and other process parameters. If we consider **Eq. 6** describing a general chemical reaction for defect formation at equilibrium, the defect equilibrium coefficient, K is expressed as **Eq. 7**. Further, thermodynamic parameters e.g., standard entropy and enthalpy changes ΔS° and ΔH° can be extracted using van't Hoff plot and **Eq. 9**, which is derived from **Eq. 8** for general temperature dependency of K .



$$K = \frac{a_C^z a_D^i}{a_A^x a_B^y} \quad \text{Eq. 7}$$

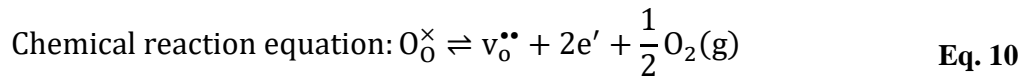
$$K = \exp \frac{(-\Delta G^\circ)}{RT} \quad \text{Eq. 8}$$

$$\ln K = \frac{\Delta S^\circ}{R} + \frac{1}{T} \frac{(-\Delta H^\circ)}{R} \quad \text{Eq. 9}$$

where A and B are the reactants, C and D the products, x, y, z, and i the number of moles of a specific reactant or product, a_C^z , a_D^i , a_A^x , and a_B^y the activity of a specific reactant or product, ΔG° the standard Gibbs energy change, R the universal gas constant, T the temperature in Kelvin.

In this thesis work, we focus on oxygen vacancy which affects the conductivity of PCEs. Therefore, as an examples, the equilibrium coefficient of the chemical reaction for forming $V_O^{\bullet\bullet}$ will be discussed below.

When oxygen content is low in a PCC, oxygen vacancies are created, and charge compensated by electrons. The chemical reaction for defect formation equation (**Eq. 10**) and the equilibrium coefficients is written below.



$$K = \frac{a_{v_O^{\bullet\bullet}} a_{e'}^2 a_{O_2}^{1/2}}{a_{O_O^{\times}}}$$

When writing equilibrium coefficients in defect chemistry, another way is to write the equilibrium coefficients in terms of molarity fractions of reactants and products instead of their activities under the following assumptions.

- 1) $[O_O^{\times}] = 1$. In mol/mol metal oxide at very low defect concentrations.
- 2) $p_{O_2}^0 = 1$ bar. Standard oxygen pressure
- 3) It is common for most purposes to neglect division by density of states.

$$K = \frac{X_{v_{\ddot{O}}} X_{e'}^2 X_{a_{O_2}}^{1/2}}{X_{O_O^x}} \quad \text{Eq. 11}$$

where X presents the site fraction of a reactant or product. For a point defect, X is the concentration of the defect over the concentration of sites.

$$X_{v_{\ddot{O}}} = \frac{[v_{\ddot{O}}]}{[O]}; X_{e'}^2 = \left(\frac{n}{N_C}\right)^2; X_{a_{O_2}}^{1/2} = \left(\frac{p_{O_2}}{p_{O_2}^0}\right)^{1/2}; X_{O_O^x} = \frac{[O_O^x]}{[O]}$$

$$K = \frac{\frac{[v_{\ddot{O}}]}{[O]} \left(\frac{n}{N_C}\right)^2 \left(\frac{p_{O_2}}{p_{O_2}^0}\right)^{1/2}}{\frac{[O_O^x]}{[O]}} = \frac{[v_{\ddot{O}}]}{[O_O^x]} \left(\frac{n}{N_C}\right)^2 \left(\frac{p_{O_2}}{p_{O_2}^0}\right)^{1/2} \quad \text{Eq. 12}$$

Neglect N_C , applying $[O_O^x] = 1$ and $p_{O_2}^0 = 1$, we have

$$K_{v_{\ddot{O}}} = K \cdot N_C^2 = [v_{\ddot{O}}] n^2 p_{O_2}^{1/2} \quad \text{Eq. 13}$$

As a summary,

$$K = \frac{a_{v_{\ddot{O}}} a_{e'}^2 a_{a_{O_2}}^{1/2}}{a_{O_O^x}} = \frac{X_{v_{\ddot{O}}} X_{e'}^2 X_{a_{O_2}}^{1/2}}{X_{O_O^x}} = [v_{\ddot{O}}] n^2 p_{O_2}^{1/2}$$

\downarrow
 In terms of the activity

\downarrow
 In terms of the site fraction

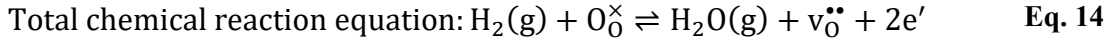
\downarrow
 Simplified notation

Fig. 5: Defect equilibrium coefficient for the defect reaction described by Eq. 10

2.2.3 Atmospheric Dependency of Defect Formation in BSZCY151020 ($Ba_{0.85}Sr_{0.15})(Zr_{0.7}Ce_{0.1}Y_{0.2})O_{3-\delta}$

In BSZCY151020, Ba and Zr are substituted with Sr and Ce respectively. Yttrium is acceptor doped and is denoted by Y'_{Zr} . The acceptor dopant can be charge compensated by protons (OH'_O), oxygen vacancies ($v_{\ddot{O}}$) or electron holes (h^*) which contribute to ionic and electronic conduction, respectively. The dominating charge carriers in BSZCY151020 depend on oxygen partial pressure and water vapor partial pressure in the environment. Both p and n type conduction can occur due to the formation of holes and positive ions at oxidizing atmosphere or electrons at reducing atmosphere.

High hydrogen partial pressure (reducing atmosphere): in a reducing atmosphere consisting of hydrogen gas, O_O^\times are consumed to form water vapor, oxygen vacancies and electrons. This can further result in the humid atmosphere reaction (**Eq. 20**). The total chemical reaction for the formation of defects is presented by **Eq. 14** and the equilibrium coefficient is written as **Eq. 15** below.



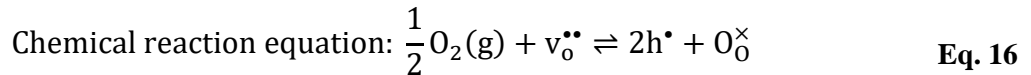
Analog to **Eq.16**, we have

$$\text{Equilibrium coefficient: } K = \frac{a_{H_2O} a_{v_O^{\bullet\bullet}} a_{n'}^2}{a_{H_2} a_{O_O^\times}}, \text{ and}$$

$$K = n^2 [v_O^{\bullet\bullet}] p_{H_2}^{-1} p_{H_2O} \quad \text{Eq. 15}$$

Low oxygen partial pressure: when oxygen content is low, oxygen vacancies are created, and charge compensated by electrons. The chemical reaction for the formation of defects has been discussed in the previous chapter, 2.2.2. The equation of chemical reaction and the equilibrium coefficients were presented by **Eq. 10** and **Eq. 13**.

High oxygen partial pressure: in oxygen rich atmosphere oxygen vacancies are consumed, which results in a p type conductivity due to formation of electron holes. The chemical reaction for the formation of the defects can be presented by equation **Eq. 16** and the equilibrium coefficient is written as **Eq. 17**.

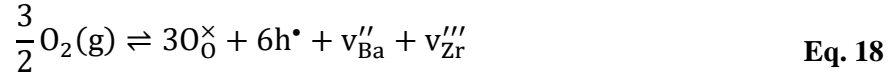


$$\text{Equilibrium coefficient: } K = \frac{a_{h^\bullet}^2 \cdot a_{O_O^\times}}{a_{O_2}^{\frac{1}{2}} a_{v_O^{\bullet\bullet}}}$$

Neglect N_V , apply $[O_O^\times] = 1$ and $p_{O_2}^0 = 1$, we have

$$K = p^2 [v_O^{\bullet\bullet}]^{-1} p_{O_2}^{\frac{1}{2}} \quad \text{Eq. 17}$$

Very high oxygen partial pressure: very oxidizing conditions can result in cation vacancies, which are charge compensated by electron holes. The chemical reaction for the formation of defects is presented by equation **Eq. 18** and the equilibrium coefficient is written in **Eq. 19**.

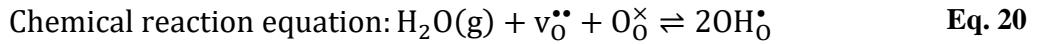


$$\text{Equilibrium coefficient: } K = \frac{a_{O_O^\times}^3 a_{h^\bullet}^6 a_{Ba}'' a_{Zr}'''}{a_{O_2}^{\frac{3}{2}}}$$

Neglect N_V , applying $[O_O^\times]/[O] = 1$, and $p_{O_2}^0 = 1$, we have

$$K = p^6 [v_{Ba}''] [v_{Zr}'''] p_{O_2}^{-\frac{3}{2}} \quad \text{Eq. 19}$$

Humid atmosphere: protons dominate as charge compensators in humid atmospheres. This process is often called “water uptake” or “hydration reaction”. The chemical reaction for the formation of defects is presented by **Eq. 20** and the equilibrium coefficient is written in **Eq. 21** below.



Analog to **Eq. 16**, we have

$$\text{Equilibrium coefficient: } K = \frac{a_{OH_O^\bullet}^2}{a_{H_2O} a_{v_O^{\bullet\bullet}} a_{O_O^\times}}, \text{ and}$$

$$K = [OH_O^\bullet]^2 [v_O^{\bullet\bullet}]^{-1} p_{H_2O}^{-1} \quad \text{Eq. 21}$$

- ❖ **Low oxygen partial pressure in humid atmosphere:** compared to oxygen vacancies and electron defects in dry atmosphere, in humid atmosphere the hydration process takes place, and the oxygen vacancies are consumed to form protons.
- ❖ **High oxygen partial pressure in humid atmosphere:** comparing to oxygen vacancies and acceptor dopants defects in dry atmosphere, in humid atmosphere the hydration process takes place, and the oxygen vacancies are consumed to form protons.

2.2.4 Brouwer Diagram

The Brouwer diagram sometimes is also titled as a Kröger-Vink diagram in literature. It is a practical method to represent the dependency of defect concentrations on changes in the activity of a component of the compound, such as oxygen partial pressure. The Brouwer diagram is a plot of logarithmic values of defect concentration against logarithmic values of p_{O_2} showing changes in defect concentrations at constant temperature. Therefore, by using Brouwer diagrams the concentration of defects in PCEs to some extent can be quantitatively characterized, which is a basis for analyzing the conductivity of the PCEs.

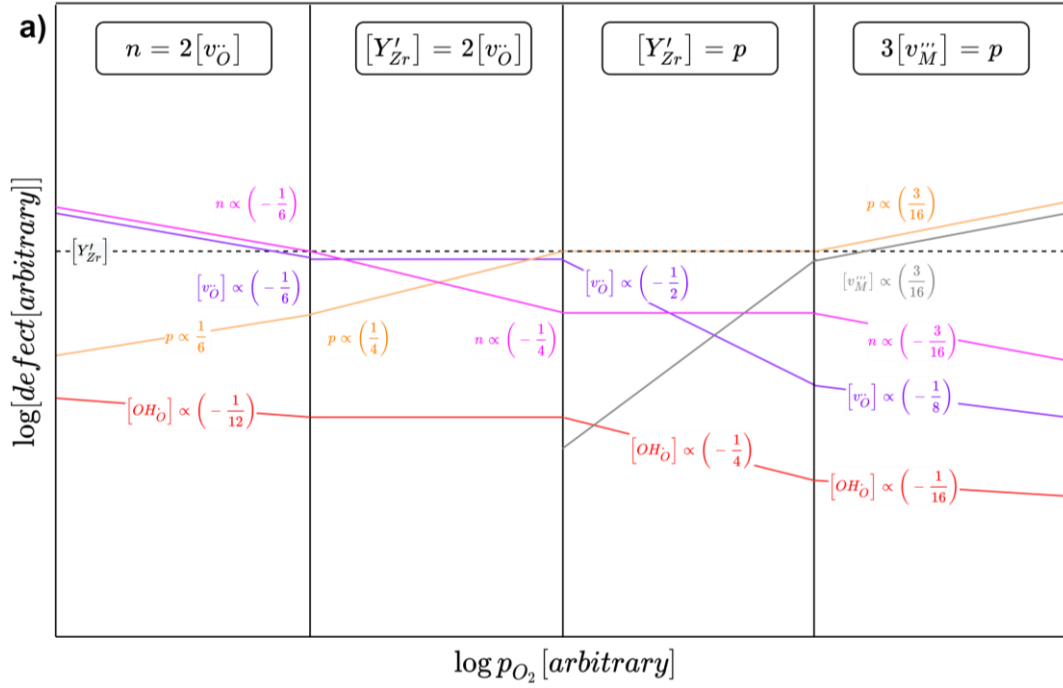
As an example, BZY after sintering, the acceptor dopant concentration stays constant. Depending on atmosphere, different boundary conditions are given by limiting the total electroneutrality condition (**Eq. 22**) to dominating defects see **Table 3**. Together with the equilibrium coefficients (Eq. 13, Eq. 17, Eq. 19, Eq. 21 and **Eq. 15**), p_{O_2} and p_{H_2O} , the Brouwer diagrams of BZY are achieved, see **Fig. 6 a) b) c)**.

$$\text{Total electroneutrality : } n + [Y'_{Zr}] + 2[v''_{Ba}] + 3[v''''_{Zr}] \rightleftharpoons p + 2[v\bullet\bullet_O] + [OH\bullet_O] \quad \text{Eq. 22}$$

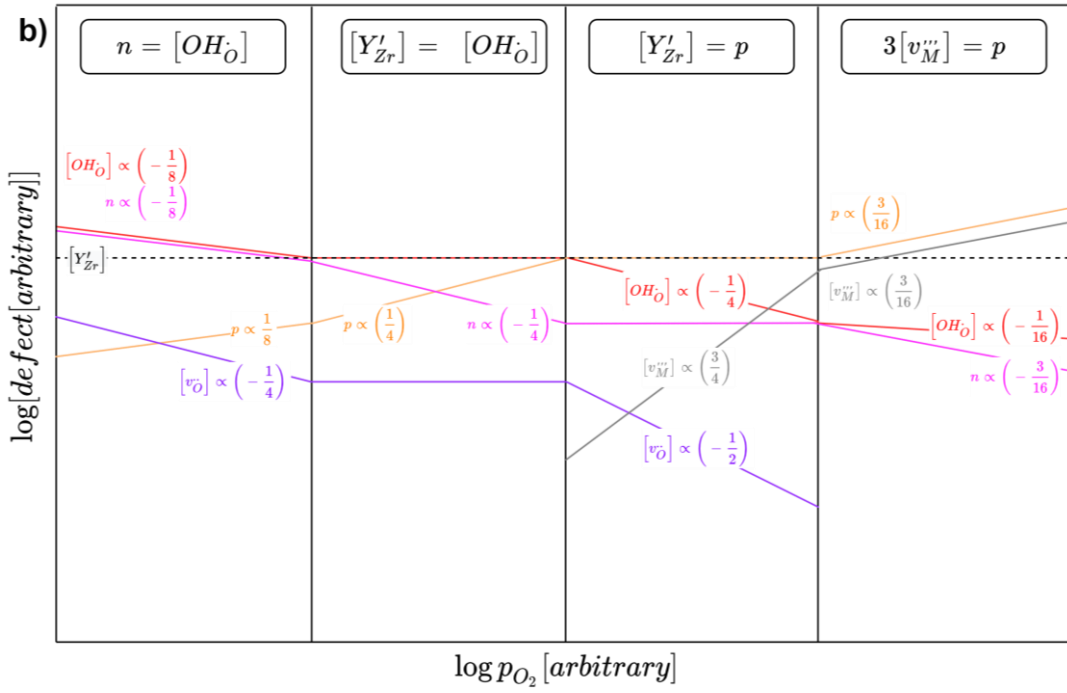
Table 3: Boundary conditions at different atmospheres.

Atmosphere	Partial pressure	Boundary condition
Dry	Hydrogen (no oxygen)	$n = 2[v\bullet\bullet_O]$
	Low oxygen	$[Y'_{Zr}] = 2[v\bullet\bullet_O]$
	High oxygen	$p = [Y'_{Zr}]$
	Very high oxygen	$p = 3[v''_M]$
Humid	Hydrogen (no oxygen)	$n = [OH\bullet_O]$
	Low oxygen	$[Y'_{Zr}] = [OH\bullet_O]$
	High oxygen	$p = [Y'_{Zr}]$
	Very high oxygen	$p = 3[v''_M]$
Dry Humid	Low water vapor	$[Y'_{Zr}] = 2[v\bullet\bullet_O]$
	High water vapor	$[Y'_{Zr}] = [OH\bullet_O]$

Dry Atmosphere



Humid Atmosphere



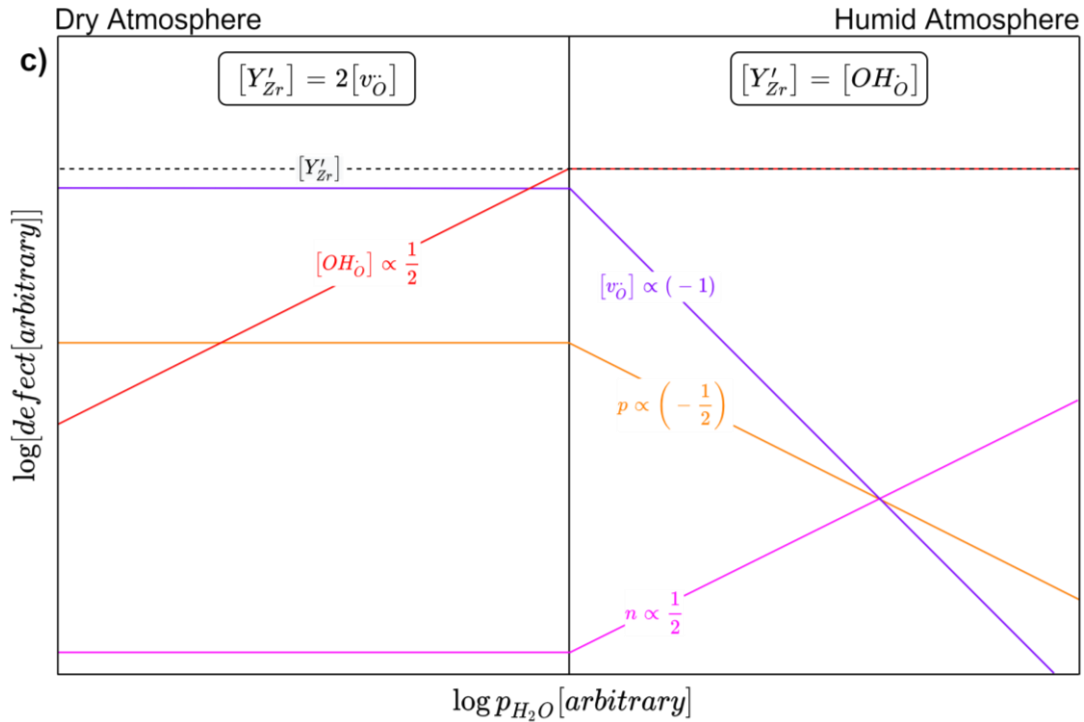


Fig. 6: a) Brouwer diagram describing BZY-defects dependency on p_{O_2} in dry atmosphere b) Brouwer diagram describing BZY-defects dependency on p_{O_2} in humid atmosphere c) Brouwer diagram describing BZY-defects dependency on humidity

2.3 Conductivity in Oxides

In oxides, such as in BZY, the charge carriers are composed of ionic and electronic charges. They are either localized via weaker chemical bonding or as free charge carriers in the crystal structures. Under electrical field, the transportation of those charge carriers will happen depending on both crystal structure and the applied electrical field and environment for example the temperature. In this chapter the theory of conductivity in oxides will be briefly introduced.

2.3.1 Electronic Conductivity

The electronic conductivity in an oxide consists of the transportation of electrons and holes. The electrons and holes are electronic defects in the oxide which are generated by designed chemical reactions and easily move around under electrical field force to carry the current through in the crystal. How easy the electrical field drive the current through the material is quantified by material conductivity, σ . The more charges in the material, the much easier for the electrical field to drive the current through, meanwhile, the less scatter of charges in the material, the easier for the charges to drift under the electrical field. The scatter of charges in the material is defined by the charge ability to move, e.g., mobility of charge, μ . Therefore, the conductivity of a material will be in principle expressed by

$$\sigma = Q\mu \quad \text{Eq. 23}$$

where Q is the total charge in transportation.

For electron conductivity,

$$Q = ne$$

$$\sigma_e = ne\mu_e \quad \text{Eq. 24}$$

Where σ_e is the electron conductivity, e the magnitude of an electron charge, n the electron concentration, and μ_e the electron mobility.

For hole conductivity,

$$Q = pe$$

$$\sigma_h = pe\mu_h \quad \text{Eq. 25}$$

Where σ_h is the hole conductivity, e the magnitude of a hole charge which equals to the magnitude of an electron charge, p the hole concentration, and μ_p the hole mobility.

2.3.2 Ionic Conductivity

Ionic conductivity in an oxide consists of the transportation of cations and anions. The cations and anions are structure defects in the oxide which are generated by designed chemical reactions and weaker localized by chemical bonding in the material. They all can be thermally activated and delocalized at certain temperature, then move under electrical field force to carry the current through in the crystal. Like electron conductivity, the cation and anion conductivity σ_c and σ_a will be used to describe the contribution of cations and anions to the current conduction.

Different from electrons and holes in the material, the cations and anions are localized in the material. They must be thermally activated and hop to the neighbor position under a drift force. If the ion mobility can be noted as μ_c and μ_a .

We have cation conductivity,

$$\sigma_c = z_c e \cdot C_c \mu_c \quad \text{Eq. 26}$$

Where σ_c is the cation conductivity, $z_e e$ the magnitude of a cation charge, c_c the cation concentration, and μ_c the cation mobility.

Anion conductivity,

$$\sigma_a = z_a e \cdot c_a \mu_a \quad \text{Eq. 27}$$

Where σ_a is the anion conductivity, $z_a e$ the magnitude of an anion charge, c_a the anion concentration, and μ_a the anion mobility.

2.3.3 Total Conductivity

The current driven through the material under electrical field results from the sum of all transportations of the different charge carriers. Therefore, the total conductivity σ of the material is simply a sum of conductivity of each charge carrier.

$$\sigma = \sigma_{\text{ionic}} + \sigma_{\text{electr}} = \sigma_c + \sigma_a + \sigma_e + \sigma_h \quad \text{Eq. 28}$$

In another way, the contribution to the total conductivity can be described by the transportation numbers t_i of the individual charge carrier.

$$t_i = \frac{\sigma_i}{\sigma} \quad \text{Eq. 29}$$

So that we can write,

$$\sigma = \sigma(t_c + t_a + t_e + t_h) \quad \text{Eq. 30}$$

2.3.3 Temperature Dependency of Conductivity

Both electron and hole conductivity will be affected by the temperature of the materials because atoms' vibration is enhanced at elevated temperatures, thus the scatter of electrons and holes are temperature dependent. As presented in above section, the ionic transportation is excited by thermal energy and results from ion hopping between the neighbor sites. As a summary, the conductivity must depend on the temperature of the material, which can be found by the Nernst-Einstein relation.

The mobility of a charge is directly determined by the mobility of its carrier, which we call the mechanical mobility of the carrier. It is not difficult to understand the following relationship between the charge mobility and its carrier mechanical mobility,

$$\mu_i = z_i e \cdot B_{mi} \quad \text{Eq. 31}$$

where μ_i is the i charge mobility, $z_i e$ the charge magnitude of i charge carrier and B_{mi} the mechanical mobility of the i carrier.

The mechanical mobility of a carrier relates to its random diffusion coefficient by the Nernst-Einstein relation in case of thermal excited hopping transportation.

$$D_i = kTB_{mi} \quad \text{Eq. 32}$$

Referring to **Eq. 31**, we have,

$$D_i = \mu_i \frac{kT}{z_i e} = \sigma_i \frac{kT}{c_i (z_i e)^2} \quad \text{Eq. 33}$$

Thus,

$$\sigma_i = (z_i e)^2 c_i \frac{D_i}{kT} \quad \text{Eq. 34}$$

Where D_i is the i carrier random diffusion coefficient, k the Boltzmann constant, T the temperature in kelvin, c_i the concentration of i charge carrier. For electrons and holes the **Eq. 32** is only meaningful when they migrate by an activated hopping mechanism.

For electrons and holes in a pure non-polar solid, they behave like free electrons and holes.

Referring to

Eq. 24 and **Eq. 25**, we have

$$\begin{aligned} \sigma_e(T) &= n(T)e\mu_e(T) \\ \sigma_h(T) &= p(T)e\mu_h(T) \end{aligned}$$

$$\text{where } \mu_e(T) \propto T^{3/2}; \mu_h(T) \propto T^{3/2} \quad \text{Eq. 35}$$

For electrons and holes in a polar (ionic) oxide, under weaker localization (large polarons) at high temperatures, they behave much like free electrons and holes too. We have

$$\mu_e(T) \propto T^{-1/2}; \mu_h(T) \propto T^{-1/2} \quad \text{Eq. 36}$$

For electrons and holes in a polar (ionic) oxide, under stronger localization (small polarons) at high temperatures (for oxides above roughly 500 °C), they behave like activated hopping process like that of ionic conduction. Referring to Eq. 32, we have,

$$\mu_e(T) = \frac{e}{kT} D_e(T) \propto T^{-1} \exp\left(-\frac{E_{a_e}}{kT}\right); \mu_h(T) = \frac{e}{kT} D_h(T) \propto T^{-1} \exp\left(-\frac{E_{a_h}}{kT}\right) \quad \text{Eq. 37}$$

where E_{a_e} is the electron activity energy, E_{a_h} is the hole activity energy.

The temperature dependent of electron and hole conductivity can be finally achieved after we find $n(T)$ and $p(T)$ and combine them with **Eq. 35**, **Eq. 36**, and **Eq. 14**. For ionic conductivity, referring to **Eq. 34**,

$$\begin{aligned} \sigma_{\text{ionic}}(T) &= (z_{\text{ion}}e)^2 c_{\text{ion}}(T) \frac{D_{\text{ion}}(T)}{kT} = (z_{\text{ion}}e)^2 c_{\text{ion}} \frac{D_{\text{ion}}(T)}{kT} \\ \sigma_{\text{ionic}}(T) &\propto T^{-1} \exp\left(-\frac{E_{a_{\text{ion}}}}{kT}\right) \end{aligned} \quad \text{Eq. 38}$$

Where c_{ion} is the concentration of the ions, a constant in most case, $E_{a_{\text{ion}}}$ the ion activation energy for hopping.

2.4 Electrochemical Impedance Spectroscopy (EIS)

The famous equation known as ohms law defines resistance as the ratio between voltage and current (**Eq. 39**).

$$R = \frac{E}{I} \quad \text{Eq. 39}$$

It is limited to one circuit element, the ideal resistor, which have many simplifying properties. In reality there are circuit elements that behave in much more complex manners. To adapt to the real world, the concept of resistance is often substituted with impedance.

2.4.1 Impedance

Impedance describes a circuit's ability to resist the flow of electrical current, however unlike resistance it is not limited by the simplifying properties below.

1. Obeys ohms law at any current and voltage altitudes
2. The resistance is independent of frequency
3. AC current and voltage signals that goes through a resistor are in phase with one another

Electrochemical impedance is measured by applying an AC potential to an electrochemical cell and then measuring the current going through the cell. By applying a sinusoidal voltage an AC current signal will arise as a response. The voltage signal is usually small, this is to ensure a pseudo-linear response from the cell and can be described by **Eq. 40**. The respondent current signal can be described by **Eq. 41**.

$$E_t = E_0 \sin(\omega t) \quad \text{Eq. 40}$$

Where E_t is the potential at time t , E_0 the amplitude of the voltage signal, and ω the radial frequency.

$$I_t = I_0 \sin(\omega t + \theta) \quad \text{Eq. 41}$$

Where I_t is the current at time t , I_0 the amplitude of the current signal, and ω the radial frequency, θ is the phase shift.

Eq. 40 and **Eq. 41** gives rise to an expression for impedance (**Eq. 42**), which is similar to that of resistance.

$$Z = \frac{E_t}{I_t} = \frac{E_0 \sin(\omega t)}{I_0 \sin(\omega t + \theta)} = Z_0 \frac{\sin(\omega t)}{\sin(\omega t + \theta)} \quad \text{Eq. 42}$$

Where Z is impedance, Z_0 is the magnitude of the impedance.

Then by using Eulers relationship (**Eq. 43**),

$$\exp(j\theta) = \cos \theta + j \sin \theta \quad \text{Eq. 43}$$

We rewrite **Eq. 40** and **Eq. 41** as,

$$\begin{aligned} E_t &= E_0 \exp(j\omega t) \\ I_t &= I_0 \exp(j\omega t - \theta) \end{aligned}$$

Expression for impedance **Eq. 42** can then also be rewritten as a complex number,

$$Z(\omega) = \frac{E_t}{I_t} = Z_0 \exp(j\theta) = Z_0 (\cos\theta + j\sin\theta)$$

For conductivity studies on our PCC, we use “Nyquist plot”. This is done by plotting $Z(\omega)$ with the real part on the X-axis and the imaginary part on the Y-axis. We look at a simplified Randles cell for bulk contribution as an example.

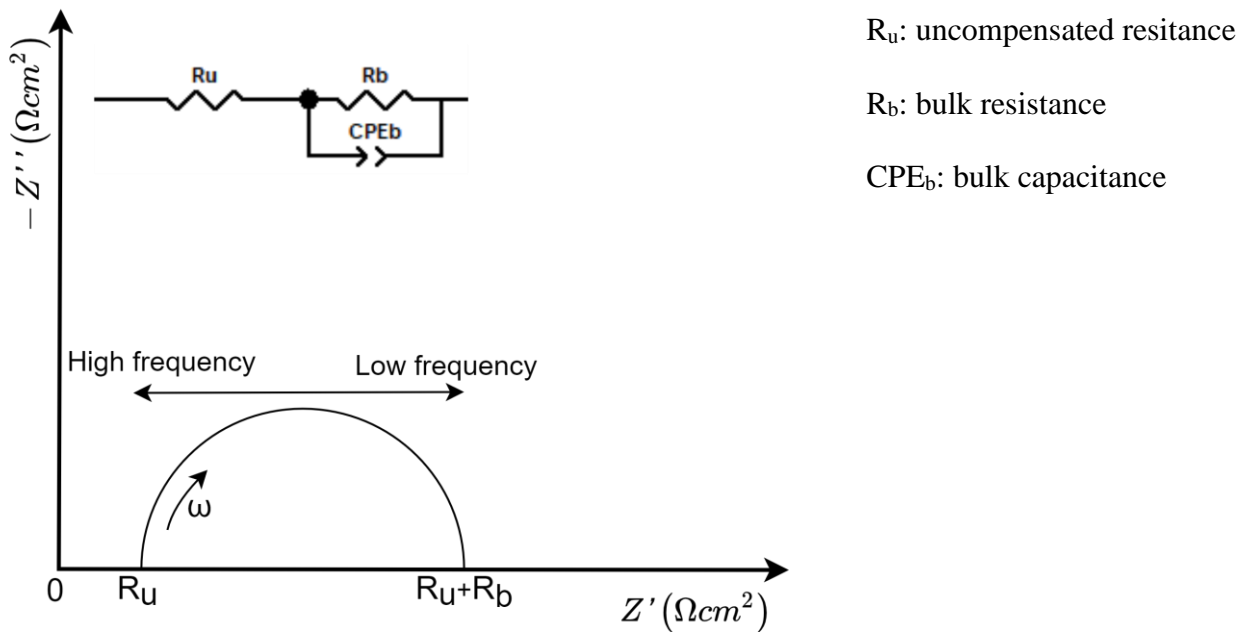


Fig. 7: Nyquist plot with equivalent circuit of a simplified Randles cell

We separate the Nyquist plot into three regions, high frequency, intermediate frequencies, low frequency.

1. At the high frequency limit to the left on **Fig. 7**, we are at 0 on the Y-axis (imaginary part) and all the impedance we are measuring is real. That means that the capacitor has no effective impedance. Therefore, the current goes through the capacitor and then across R_u , while no current is passed through R_b .

2. As we go to lower and lower frequencies, the capacitor starts to have a significant contribution to the impedance. The capacitance pushes the curve up into the negative imaginary direction and the phase angle starts to deflect from 0° and go towards 90° .

3. As we go to very low frequencies, the impedance of R_b does not change, but the impedance of CPE_b gets so high that all current starts flowing through the resistors and we are back to zero on the imaginary part, our real impedance is then the sum of R_u and R_b .

A typical EIS of a PCC has three of these Randles cells, first describing bulk contribution, second describing grain boundary, and a third describing electrode contribution. These can be separated and identified by using classification of capacitance [18], see **Fig. 8**. The capacitance of the CPE are calculated from the fitted CPE terms, CPE-T and CPE-P using equation **Eq. 44**, then this value was normalized to units of $F\text{ cm}^{-1}$ by multiplying with the sample length (L) and dividing with the Pt-ink electrode area (A).

$$C = R \frac{1-CPET}{CPEP} \cdot CPET \frac{1}{CPEP} \quad \text{Eq. 44}$$

When measuring, the different semi circles, they will overlap where they meet, resulting in an experimental curve that looks more like the red dotted line in **Fig. 8**.

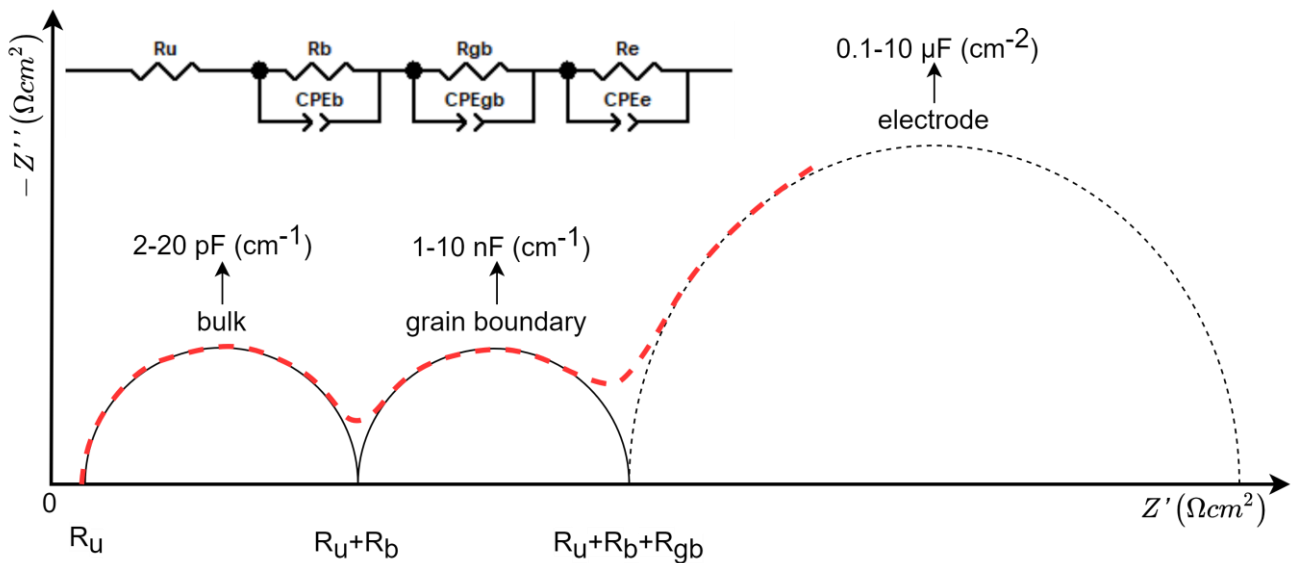


Fig. 8: Typical equivalent circuit and EIS of PCC

From the figure above, we can see that the circuit elements can be decided from the EIS, where the curve intercepts with the x-axis. When the circuit can be used to model the PCC impedance, the resistance of bulk and grain boundary can be found. Therefore, the conductivity can also be found.

3 Experimental Setup

This section the different experimental setups used in this project are described in more detail.

3.1 Ball Mill for Grinding and Mixing Materials

The ball mill is a kind of grinder, which is used to grind or mix materials such as, paint, ores, and ceramic raw materials. The ball mill works by, 1) filling a container with the material that is to be ground in addition to the grinding medium, 2) putting the closed container into the ball mill, which then rotates around a horizontal axis. This process results in an internal cascading effect that reduces the material to fine powders.

Both “CAPCO Ball Mill Model 12VS” and “Retsch® PM100” seen in **Fig. 9** are used in this thesis work. 5 mm YSZ balls were used as grinding medium in the rolling ball mill (RM), while a combination of 5 mm and 10 mm balls were used in the planetary ball mill (PM).

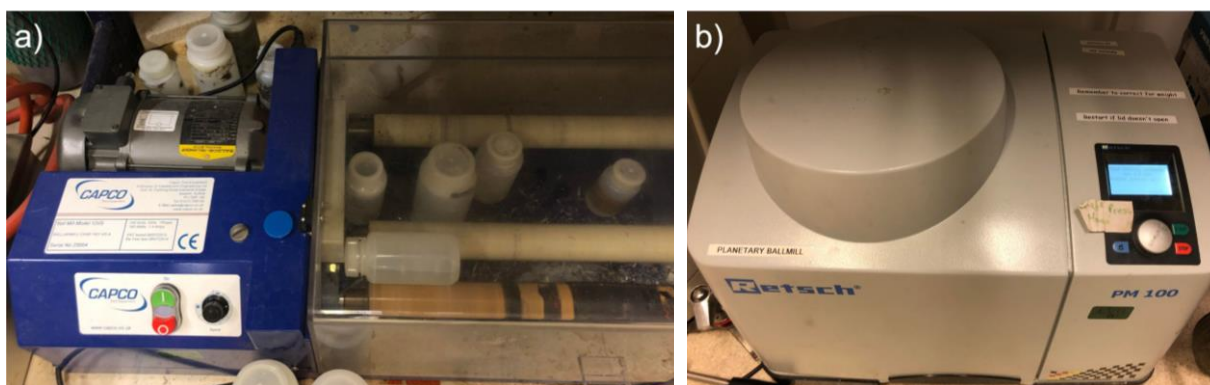


Fig. 9: a) CAPCO Ball Mill Model 12VS b) Retsch® PM 100

We use the RM for mixing to grind and mix the precursors, while the PM also crushes the powders to finer powder while mixing.

3.2 Muffle Furnace for High Temperature Experiments

A muffle-furnace is usually a front-loading box-type oven for high-temperature applications. It offers rapid high-temperature (HT) heating, cooling, and recovery. In a modern furnace, convection energy or radiation is used to apply heat to a chamber by using a HT heating coil inside insulated material. The insulating materials prevents heat from escaping the chamber, thus working as a muffle. Both “Nabertherm LVB524” and “Nabertherm HT LVB533” were available in the lab, each equipped with a temperature controller “P 330” and ”P 310” respectively, as seen in **Fig. 10**.



Fig. 10: Picture of muffle furnaces, a) Nabertherm LVB524 b) Nabertherm HT LVB533

In this master project, we used the muffle furnaces to sinter green bodies, fire Pt-ink contacts for adhesion, and conduct thermal etching.

3.3 Dilatometer for Investigation of Sintering Process

A dilatometer (DIL) is a scientific instrument that measures dimensional changes caused by chemical or physical processes in a material as a function of temperature. A pushrod dilatometer, which was used in this master project, consists of three main parts. A furnace, a pushrod, and the unit for measuring data acquisition and evaluation. The dilatometer used in this master project was a NETZSCH DIL 402C (**Fig. 11**), which was controlled via its computer software “DIL 402C on 18 TASC 414_4”. “Proteus Analysis” was used for analysis.



Fig. 11: NETZSCH DIL 402C Dilatometer

Temperature profiles with different heating and cooling rates as well as holding points can be designed for controlling the temperature of the furnace. Thus, the change in sample length is determined as a function of temperature. During the measurements, the sample is connected to the pushrod, which transmits the length changes to the data acquisition instrument. The absolute

change in length is determined by using known data of the measuring system together with sample dimensions. Using dilatometer, information such as thermal expansion coefficient, phase transitions, and sintering temperature profiles can be extracted.

In this master project, we use the pushrod dilatometer was used to study the sintering behavior of the samples to determine the optimal temperature profiles for sintering the green bodies to dense pellets, and to study chemical and physical processes in the sample material during sintering.

3.4 X-Ray Diffraction for the Crystallographic Study

X-ray diffraction (XRD) are used to determine crystal structure of samples. This is done by irradiating the sample with incident X-rays, followed by measuring the intensities and scattering angles of the X-rays that leave the sample.

An X-ray is an electromagnetic wave. Its wavelength (λ), and angle of incidence (θ) to the sample, and the lattice constant (d) of the sample are related by Bragg's law (**Eq. 45**).

$$2 d \sin \theta = n\lambda \qquad \text{Eq. 45}$$

The diffraction takes place when this equation is fulfilled. Due to the nature of diffraction, wave beams can either cancel each other out by destructive interference or add by constructive interference. This results in a diffracted beam pattern that appears to have stronger energy in some parts and lower energy in other parts. By varying the crystal orientation, beam wavelengths, and incident angles, different diffracted patterns will be achieved. The crystal structure of the sample material can be identified by comparing its diffracted peaks with a library of known crystalline materials.

“Rigaku MiniFlex600”, “RECX-DIFF5”, and “RECX1” are used in this thesis project, seen in **Fig. 12**. For phase identification “Diffrac.eva” software was used to analyze the achieved results from XRD measurements. For finding lattice parameter, Rietveld refinement was conducted by fitting the achieved results from XRD measurements with “Topas” software.

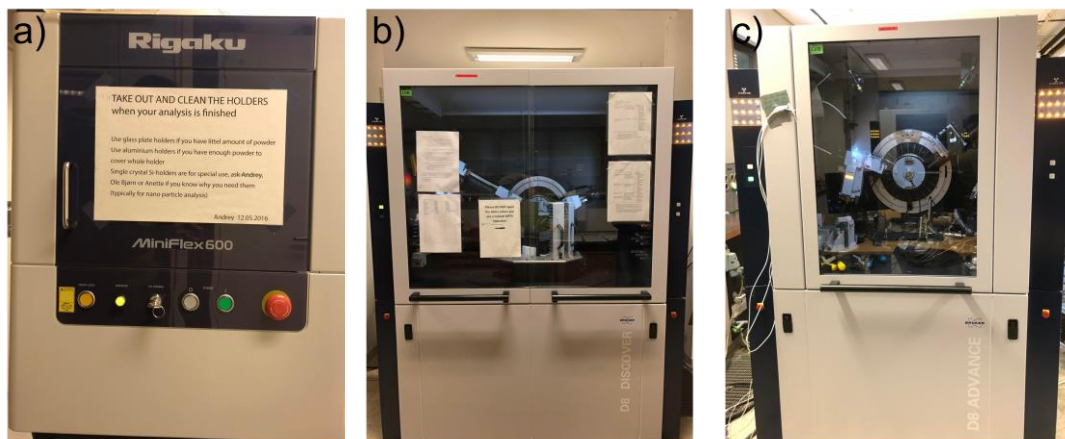


Fig. 12: Picture of XRD instruments, a) Rigaku MiniFlex600 b) RECX-DIFF5 c) RECX1

During our investigation, after each sintering step, samples will be characterized by XRD analysis. We can determine if the sample has been sintered to the wanted composition. To identify the phase formation during the sintering of the pellets, we perform a high-temperature XRD (HT-XRD) analysis using “RECX1” in the temperature range of 30°C to 1200°C.

3.5 Thermal Gravimetric Analysis for Water Uptake study

Thermal gravimetric analysis (TGA) is a type of thermal analysis, by which the sample mass is monitored as temperature changes in a controlled atmosphere. The base measured quantities in TGA are mass, temperature, and time, from which additional quantities can be determined. A TGA comprises a sample holder/pan that is supported by a precision balance inside a furnace. The atmosphere can be controlled by a gas mixer that purges the gas over the sample and exits from an exhaust. We use NETZSCH STA 449 F1 Jupiter[®] (see **Fig. 13**) throughout our project, which was operated via a computer software “NETZSCH-Proteus-6.1”. The “Proteus Analysis” was used for analyses.

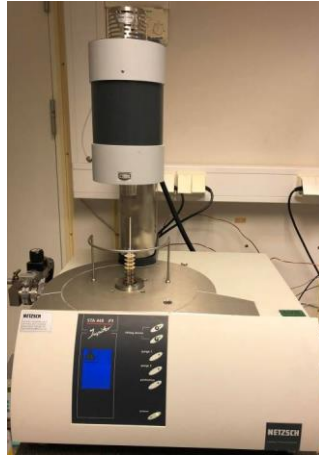


Fig. 13: NETZSCH STA 449 F1 Jupiter® Thermal Gravimetric Analyzer

The water uptake through the hydration reaction in the samples as well as the sintering behavior of PCE in this project will be studied by using the TGA

3.6 Scanning Electron Microscopy for Surface Morphology Study

Scanning electron microscopy (SEM) determines the morphology of a surface in contrast to microstructures or element concentration. SEM uses a focused beam of high energy electrons bombarding the sample and collects the reflections which include a variety of signals at the sample surface. These signals are called electron sample interactions, which can reveal information about the sample, such as surface topography, chemical composition, and crystalline structure and orientation of the sample. We can illustrate micro- to nano-scale features with large magnification and identify elemental composition in or on the surface of the sample. Usually, data are collected over a selected area of the sample surface to generate a 2-dimensional (2D) image that displays spatial variations of the properties of the sample. In general, the SEM uses Everhart-Thornley detectors (ETD) for analyzing the reflected electrons such as secondary electrons (SE) and backscattered electrons (BSE). The SE imaging mode is most effective for studying surface morphology and topography on the sample, while the BSE imaging mode is most effective for showing contrast in composition in a multiphase sample. When an X-ray detector is added to SEM, it can also perform analyses of specific point location on the sample for qualitatively/semi-qualitatively determination of chemical compositions using energy dispersive X-ray spectroscopy (EDS).

In this project, both SE imaging and BSE imaging modes were used to investigate sintered PCC pellets. According to analysis demands, we use “HITACHI SU8230”, “FEI Quanta 200”, and “HITACHI TM3000 Tabletop Microscope”, seen in **Fig. 14**, for different characterizations respectively.

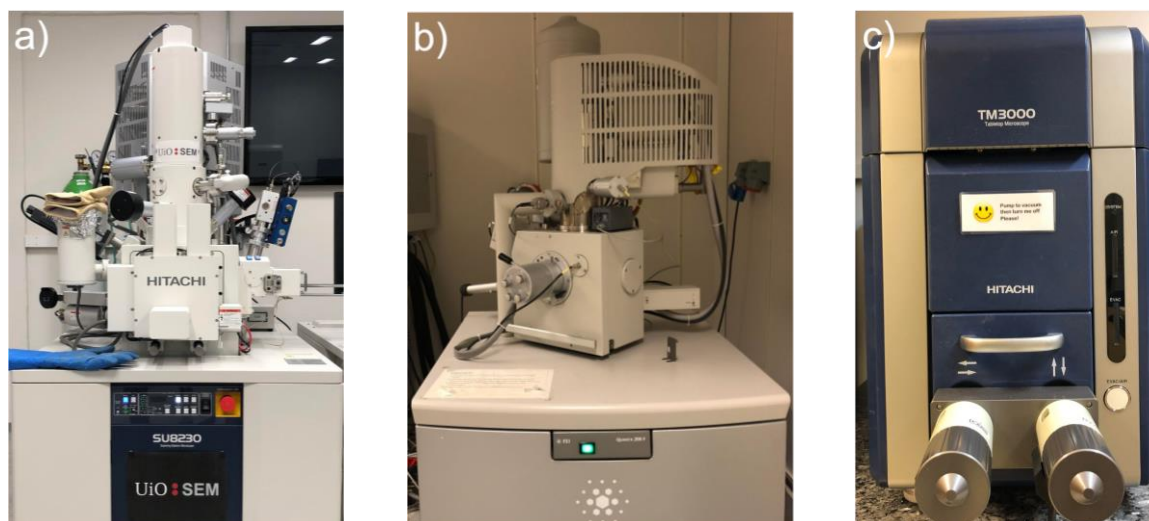


Fig. 14: Picture of SEMs used in this thesis project. a) HITACHI SU8230 SEM b) FEI Quanta 200 c) HITACHI TM3000 Tabletop Microscope

3.7 Gas Mixer for Providing Specific Atmosphere

By using gas mixers, we can provide specific atmospheres for material synthesis and property testing, examining device performance and reliability, study of atmosphere dependence of both materials and devices. Oslo mixer at the University of Oslo has been used in numerous studies of PCC oxide properties as a function of p_{O_2} , p_{H_2O} , etc. Low-flow glass tube flowmeters from Brooks® (**Fig. 15**) are equipped in Oslo mixer. Partial pressures of each gas can be calculated using flowmeter readings via its accompanying software, “ProGasMix software v.0.7.1” from NORECS AS. The Oslo mixer features a wetting stage and a drying stage. In the wetting stage, the gas is passed over a water container followed by bubbling through a KBr



Fig. 15: Brooks® Gas Mixer Flowmeters

saturated water solution, which results in a ca. 80% relative humidity atmosphere to avoid corrosion in the copper tubes. The corrosion in the copper tubes can cause unwanted clogging

over time. The drying stage involves passing the gas over P_2O_5 powder resulting in an atmosphere of p_{H_2O} under 10^{-6} .

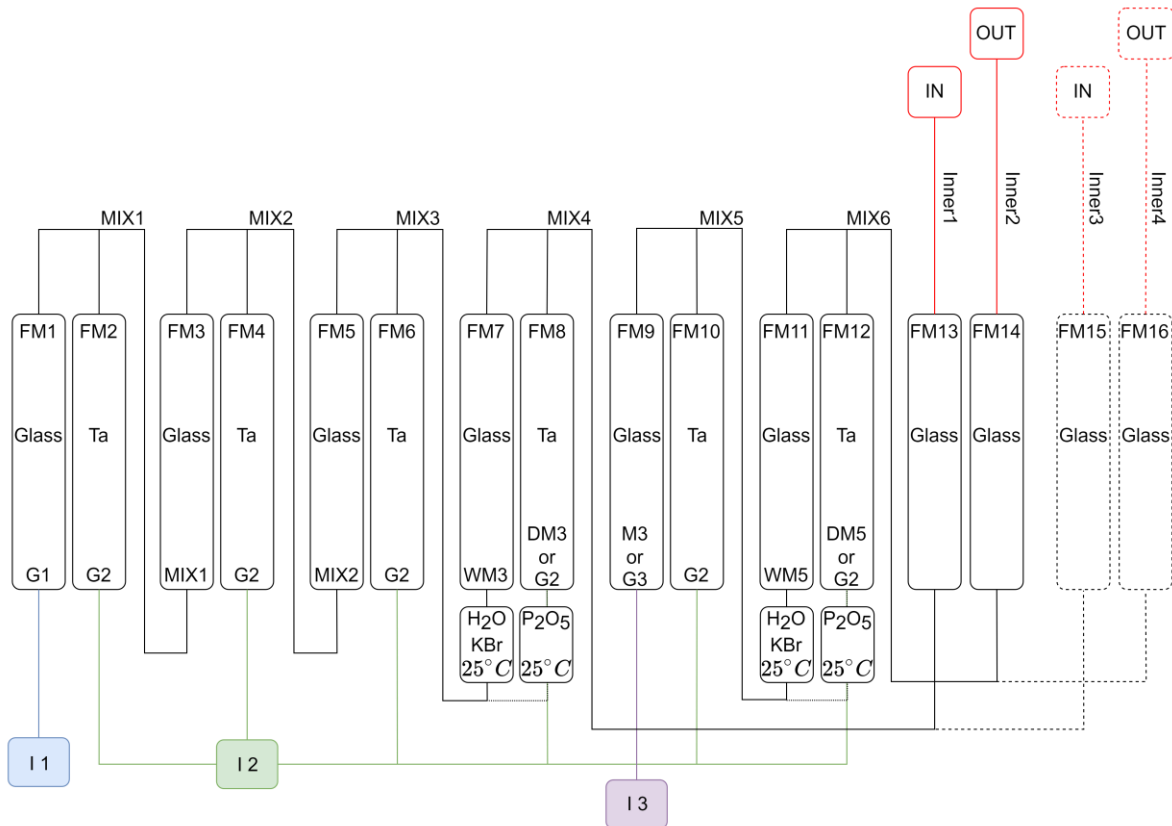


Fig. 16: Schematic of gas mixer setup

In this project, we use Oslo mixer to control the atmosphere in TGA, EIS, and EMF experiments. In TGA, dried air and humid air were supplied to investigate water uptake. In EIS, bottle dry air, humid air, argon, oxygen, HARMix, and hydrogen were used. In EMF, Oslo mixer has the unique ability to deliver two mixtures suitable for transport number measurements.

3.8 ProboStat for Measurement at High Temperature and Controlled Atmosphere

The ProboStat is a cell as the sample holder used for measuring material property at elevated temperatures under controlled atmospheres [19]. It can be applied in measuring the transport parameters, electrical properties, and kinetics of materials, furthermore, the solid/gas interfaces and electrodes. In this thesis work the ProboStat is accompanied by “Novocontrol Alpha” for EIS measurements and a “Solartron 1260” (Zurich Instruments, Switzerland) for EMF measurement.

During operation, the sample rests on top of a support alumina tube of approximately 50 cm in length, which is inside a closed outer alumina tube. The sample is contacted with 2, 3 or 4 electrodes, usually platinum. The sample and electrodes are held in place by a spring-loaded alumina assembly. There are 16 electrical feedthroughs on the ProboStat, which allows the use of 4 shielded electrode leads, up to 3 thermocouples, and surface guard. Electrical connections are achieved by coax cables fit for impedance spectrometer connectors and standard thermocouple compensation cables. Gas supply is made by Swagelok quick-connects. Gas can be supplied in single or dual chamber modes from or onto electrodes, which allows measurements under controlled atmospheres. Setting up with the furnace, Oslo mixer, and electrochemical measuring station, the ProboStat was used for EIS and EMF measurements at designed conditions to study PCC.

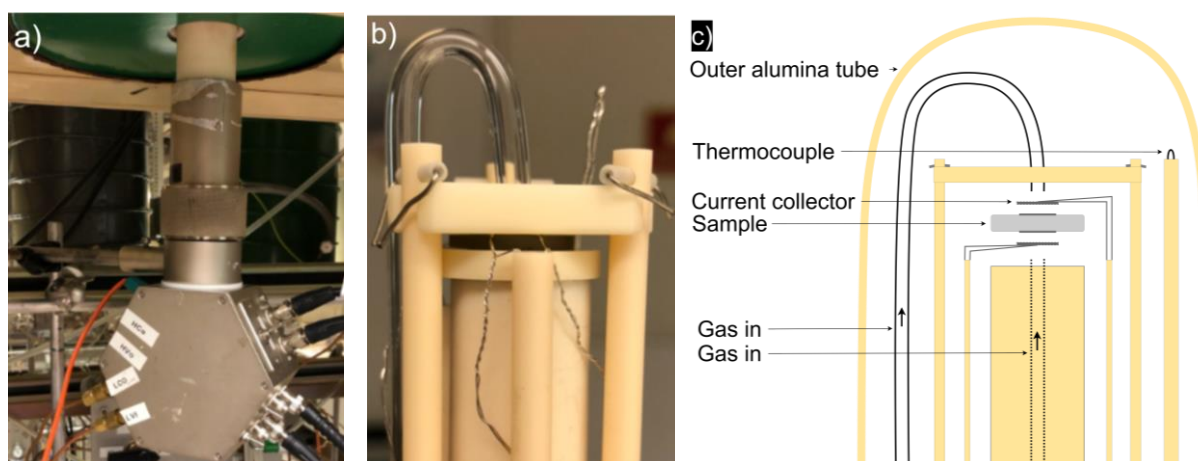


Fig. 17: a) Picture of ProboStat during measurement, b) setup, c) schematic of setup

4 Technical Approaches and Experimental Procedures

In this section the technical approaches and experimental procedures are presented in detail. Because we want to focus on the effect of various fabrication conditions on crystal structure and morphology, thus on the material properties such as relative density, total conductivity, and TEC, we will modify experimental conditions to tailor the crystalline, microstructure and morphology for desired properties.

Thereafter, the full characterization of the fabricated PCCs will be conducted by SEM, XRD, TGA, EMF and EIS using ProboStat measurement cell under controlled atmospheres, notably $p_{\text{H}_2\text{O}}$, p_{O_2} , p_{H_2} , and HArMix. Furthermore, the fabrication process will be optimized by analyzing the material structure according to its achieved performance. Therefore, the total study flow can be illustrated by the following flow chart.

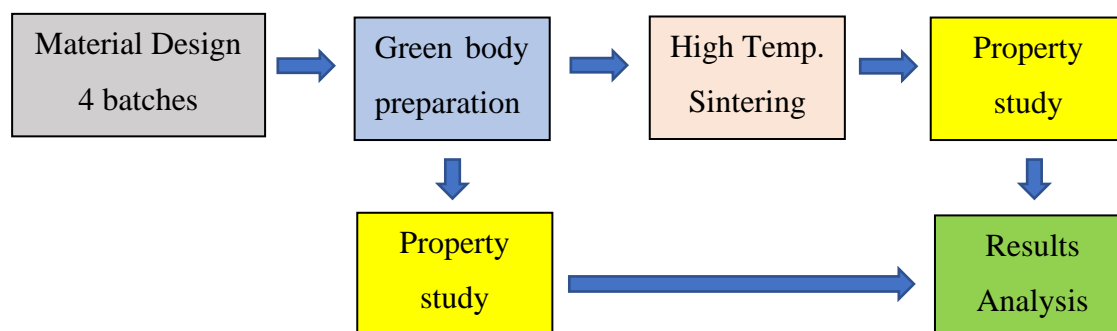


Fig. 18: Flowchart describing the sequence of actions done in this project

This section includes 4 paragraphs that describes all the experimental procedures related to the total study flow above, e.g., 1) Sample fabrication, 2) Study of PCC physical properties, 3) sample microstructure investigation, and 4) Electrochemical performance of the samples.

4.1 Synthesis and Fabrication of PCCs

In this thesis work, after reviewing the typical research work in this field worldwide and the results achieved from our UiO group in the past, we decide to focus on doped BZY materials. BSZCY151020 were synthesized using solid-state reactive sintering (SSRS), which involves mixing precursors and sintering aids, pressing pellets and direct firing at a sufficiently high temperature with the goal of forming a single-phase and dense specimen. As mentioned above, our approach will be 1) adjust precursors, 2) ZnO as additive sintering aid elements, 3) particle

size by varying ball-milling parameters, 4) sintering temperature and temperature profile. Therefore, four batches of material variations are designed as shown in in **Table 4** below. Samples will be made without sintering aid (pristine BSZCY151020) and doped with 2 mol% ZnO (BSZCYZn1510202). Both RM as low energy milling and PM as high energy milling were used.

Table 4: The samples investigated in this thesis project

Batch name	Precursors	Milling condition	Nominal composition (mol fraction)	Total powder weight (g)
PM BSZCY151020	BaCO ₃ SrCO ₃ ZrO ₂ CeO ₂ Y ₂ O ₃	PM	(Ba _{0.85} Sr _{0.15}) (Zr _{0.7} Ce _{0.1} Y _{0.2})O _{2.9}	14.40
RM BSZCY151020	BaCO ₃ SrCO ₃ ZrO ₂ CeO ₂ Y ₂ O ₃	RM	(Ba _{0.85} Sr _{0.15}) (Zr _{0.7} Ce _{0.1} Y _{0.2})O _{2.9}	14.40
RM BSZCY151020 w/ YSZ	BaCO ₃ SrCO ₃ CeO ₂ Y ₂ O ₃ YSZ (TZ-8Y)	RM	(Ba _{0.85} Sr _{0.15}) (Zr _{0.7} Ce _{0.1} Y _{0.2})O _{2.9}	28.74
RM BSZCYZn1510 202 w/ YSZ	BaCO ₃ SrCO ₃ CeO ₂ Y ₂ O ₃ YSZ (TZ-8Y) ZnO	RM	(Ba _{0.85} Sr _{0.15}) (Zr _{0.68} Ce _{0.1} Y _{0.2} Zn _{0.02})O _{2.88}	28.72

The suppliers of the materials are listed in the table below.

Table 5: Information about the precursors

Precursor	Purity	Supplier	CAS-number
BaCO ₃	≥99%	Sigma-Aldrich	513-77-9
SrCO ₃	99%	Alfa Aesar	1633-05-2
ZrO ₂	99%	Sigma-Aldrich	1314-23-4
CeO ₂	99.95%	Siga-Aldrich	1306-38-3
Y ₂ O ₃	99.9%	Alfa Aesar	1314-36-9
ZnO	99.99%	Sigma-Aldrich	1314-13-2
TOSOH-Zirconia TZ-8Y	-	TOSOH	-

The green body samples were prepared by the following steps:

1. The weights of each precursor needed were calculated from the mol fractions.
2. The precursors were weighed by a precision balance with accuracy of 4 decimals.
3. PM or RM was used according to the material designs in **Table 4**.
 - a. PM: powders of raw materials were put into a milling jar together with 5 mm BZY-balls. Isopropanol was added until it covered both powders and BZY-balls. The milling took a total of 12 hours using 350 rpm with an interval of 5 min.
 - b. RM: powders of raw materials were put into milling container together with a combination of 10 mm and 5 mm BZY-balls. Isopropanol was added until it covered both powder and BZY-balls. The milling took a total of 72 hours (3 days).
4. The milled powder was dried on a hotplate with magnet steering.
5. Binder (5 wt% B-60 and 5 wt% B-72 mixed with 90 wt% ethyl acetate) was added to the dried powder and mixed by grinding in mortar with pestle.
6. The well mixed powders containing binder were then pressed into green bodies using a 20 mm diameter dye and a cold press with 2 ton force. Please note, sample for DIL experiment was prepared with 6 mm diameter dye and a cold press with 1.5 ton force.

The picture of a green body sample is shown in **Fig. 19**.

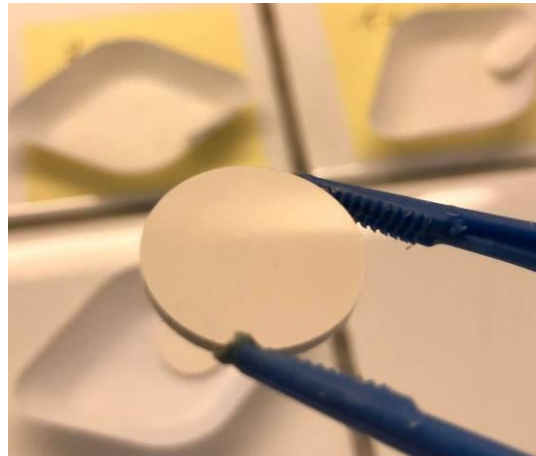


Fig. 19: The picture of a green body sample PM BSZCY151020.

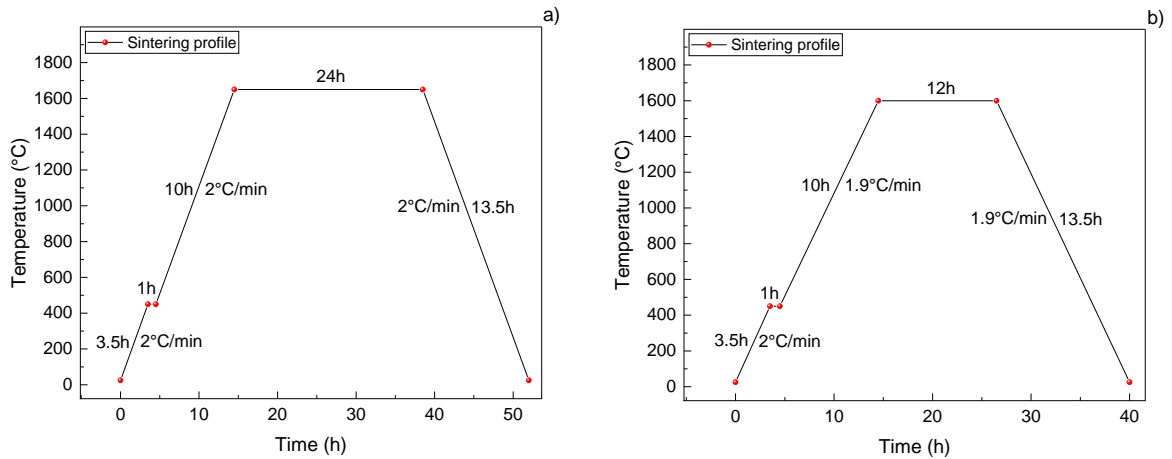
For the sintering process, referring to the past experiments in our research group, we designed the sintering temperature profiles shown in **Table 6**.

Table 6: Temperature profiles for sintering of the four samples.

Sample name	Segment mode	Rate (°C/min)	Temperature (°C)	Time (hh:mm)
PM BSZCY151020	Initial	-	25	-
RM BSZCY151020	Dynamic	2	450	03:30

RM BSZCY151020 w/ YSZ	Isothermal →	0	450	01:00
	Dynamic ↗	2	1650	10:00
	Isothermal →	0	1650	24:00
	Dynamic ↘	2	25	13:30
RM BSZCYZn1510202 w/ YSZ	Initial ○	-	25	-
	Dynamic ↗	2	450	03:30
	Isothermal →	0	450	01:00
	Dynamic ↗	1.9	1600	10:00
	Isothermal →	0	1600	12:00
	Dynamic ↘	1.9	25	13:30
RM BSZCYZn1510202 w/ YSZ	Initial ○	-		
	Dynamic ↗	2	450	03:30
	Isothermal →	0	450	01:00
	Dynamic ↗	1.8	1500	10:00
	Isothermal →	0	1500	12:00
	Dynamic ↘	1.8	25	13:30
RM BSZCYZn1510202 w/ YSZ	Initial ○	-		
	Dynamic ↗	2	450	03:30
	Isothermal →	0	450	01:00
	Dynamic ↗	1.6	1400	10:00
	Isothermal →	0	1400	12:00
	Dynamic ↘	1.7	25	13:30

For simplicity, the table is summarized as the plots shown in **Fig. 20**.



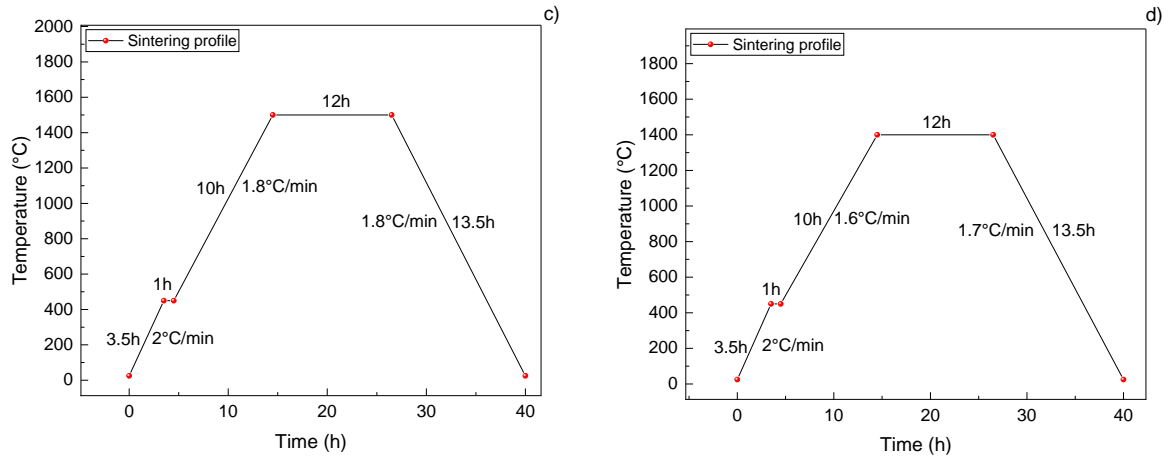


Fig. 20: Plot of sintering profiles, a) PM BSZCY151020 – 1650 °C, RM BSZCY151020 – 1650 °C, RM BSZCY151020 w/ YSZ – 1650 °C, b) RM BSZCYZn1510202 w/ YSZ – 1600 °C, c) RM BSZCYZn1510202 w/ YSZ – 1500 °C, d) RM BSZCYZn1510202 w/ YSZ – 1400 °C.

4.2 Investigation of Physical Properties

In this thesis work, we will focus on monitoring the material properties such as relative density, crystal structures, total conductivity, and TEC. Sintering behavior of PCC will be studied with DIL measurements. The crystal structure of the PCCs will be identified by using XRD methods. The conductivity of the PCCs is related to the concentration of oxygen vacancies which can be measured by water uptake using TGA. The TEC will be investigated by operando HT-PXRD at varying temperatures.

4.2.1 Dilatometer Experiment







1. DIL measurements from 25 °C to 1600 °C

All dilatometer experiments were done in ambient air. For each experiment the green body was placed into the alumina sample holder, the pushrod was then extended such that it was in contact with the sample. The initial length was measured with an electronic ruler and registered in the software. Further, the furnace was closed followed by programming the temperature profile before starting the measurements.

Via DIL experiment, the expansion or shrinkage of a sample with temperature change could be found. Therefore, the green body after DIL experiment goes through a sintering process involving, 1) Initial temperature (the room temperature in this project), 2) dynamic temperature rising, 3) isothermal stage, 4) dynamic temperature rising, 5) isothermal stage, and 6) dynamic

temperature cooling. The process is almost the same as that shown in **Table 6**, with temperature profile summarized below in **Table 7**.

Table 7: Temperature Profile for DIL experiments







Segment mode	Rate (°C/min)	Temperature (°C)	Time (hh:mm)
Initial 	-	25	-
Dynamic 	2	450	03:32
Isothermal 	0	450	01:00
Dynamic 	2	1600	09:35
Isothermal 	0	1600	12:00
Dynamic 	2	25	13:07

All four batches were measured following the same temperature profile in **Table 7**.

2. DIL measurements from 25°C to 1134°C

During sintering, we discovered an unusual phenomenon for samples of batches 1 and 2. The shrinking happens before the expansion, which we define as a sintering shoulder in this thesis. Therefore, we decide to do more experiments to further study the sintering shoulder behaviors. Dilatometry experiments were done at the temperature range in which the sintering shoulder appears. Green bodies of PM BSZCY151020 and BaCO₃ were used for further study. The temperature profiles in the DIL experiments are summarized in the following **Table 8**.

Table 8 : Temperature Profiles

Segment mode	Rate (°C/min)	Temperature (°C)	Time (hh:mm)
Initial 	-	25	-
Dynamic 	2	450	03:32
Isothermal 	0	450	01:00
Dynamic 	2	1134	05:42
Isothermal 	0	1134	00:01
Dynamic 	20	25	00:55

4.2.2 XRD

Due to the polycrystal nature of our PCC, we employ powder X-ray diffraction (PXRD) method in ambient air to find the lattice parameter and to identify the sintered phase in the sintered pellets.

1. PXRD – identification of sintered phase

Phase identifications were done for all 6 sintered pellets. Sample preparation is described below.

1. Sintered pellets were grinded to powders in mortar with pestle.
2. Si powder were added as reference powder.
3. Then some isopropanol was added and mixed with the powder.
4. The mixture of powder and isopropanol were extracted by a pipette and loaded onto sample holders.

The measurement conditions for the PXRD are shown in **Table 9**.

Table 9: Program for PXRD experiment

Measurement conditions	
Scan type	Couples TwoTheta/Theta
Start - end	10.023° - 90.023°
Step size	0.020°
Steps	4001
Total time/step	1 s
Environment	
Humidity	-
Temperature	25 °C (room)
Wavelengths	
$k\alpha_1$	1.54060 Å
$k\beta$	1.39224 Å
Wavelength for display	1.54060 Å

2. HT-PXRD – phase formation during sintering

To find the crystal formation and its lattice parameter versus temperature, we have conducted HT-PXRD experiment using PM BSZCY151020 – 1650 °C samples that are prepared as the following,

1. The raw powder consisting of precursors was grinded to powders in mortar with pestle by hand.
2. The powders were loaded directly onto the HT-PXRD sample holder.




The measurement conditions for the HT-PXRD are shown in **Table 10** and **Table 11**. The operando PXRD is performed every 50°C from room temperature to 900°C, and every 5°C

from 900°C to 1200°C. A large amount of data was achieved from the operando HT-PXRD for sintering behavior study.

Table 10: Program for HT-PXRD experiment

Measurement conditions	
Scan type	Still (Eiger2R_500K (1D mode))
Start - end	10.335° - 29.646°
Step size	0.019°
Steps	1013
Total time/step	120 s
Time/step	120 s
Goniometer Radius	250 mm
Goniometer Radius Primary	280 mm
Goniometer Radius Secondary	220 mm
Wavelengths	
Anode	Mo
Focus orientation	Line Focus
$k\alpha_1$	0.70930 Å
$k\alpha_2$	0.71359 Å
$k\alpha$ ratio	0.5
$k\beta$	0.63229
Wavelength for display	0.70930

Table 11: Temperature profile for HT-PXRD

Segment mode	Segment Rate (°C/min)	Temperature segment (°C)	Temperature step (°C)
Initial 	-	30	-
Dynamic 	2	30 - 900	50
Dynamic 	2	900 - 1200	5

4.2.3 Thermal Gravimetric Analysis

For study of hydration reaction in the samples as well as the sintering behavior of PCC in this project, we performed operando TGA experiments to study the water uptake at temperatures from 800 °C to 100 °C after the samples were dried at 900 °C. Samples of the 4 batches that were made through SSRS were used to discover the information of their oxygen vacancy concentration. The samples were sintered with specific temperature profiles to study the sintering shoulder, and to look for the cause of the sintering shoulder in detail. For all TGA experiments, a 10 ml/min flow of nitrogen was used as protective gas.


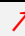



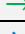




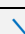
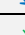

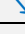




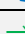

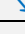





In this operando TGA experiments, all samples are prepared as the following,

1. The sintered pellets were grinded with mortar and pestle by hands.
2. The sample of grinded powders for operando TGA experiment is weighed using a balance.
3. The sample powders are then loaded to an alumina holder for measurements

1. TGA experiments on designed 4 batches PCCs

Each of the samples was heated up to 900°C in dry atmosphere and waiting long enough to drive all water out of the sample, then, we switched from dry atmosphere to wet atmosphere by using the Oslo mixer, the mass loss were continuously recorded at temperatures from 900 °C to 100 °C with a cooling profile shown in **Table 12**. Please note, for sample RM BSZCYZn1510202 w/ YSZ - 1500 °C, TGA measurement was done throughout all temperature steps, but TGA measurements for the rest of the samples were carried out without temperature steps marked in the yellow field in **Table 12**.

Table 12: Temperature profiles for water uptake experiments

Segment mode	Rate (K/min)	Temperature (°C)	Time (hh:mm:ss)	Atmosphere
Initial 		30	-	Dry
Dynamic 	10	900	01:27:00	
Isothermal 	-	900	01:30:00	
Dynamic 	10	800	00:10:00	Wet
Isothermal 	-	800	01:30:00	
Dynamic 	3	750	00:16:40	
Isothermal 	-	750	01:00:00	
Dynamic 	3	700	00:16:40	
Isothermal 	-	700	01:00:00	
Dynamic 	3	650	00:16:40	
Isothermal 	-	650	01:00:00	
Dynamic 	3	600	00:16:40	
Isothermal 	-	600	01:00:00	
Dynamic 	3	550	00:16:40	
Isothermal 	-	550	01:00:00	
Dynamic 	3	500	00:16:40	
Isothermal 	-	500	01:00:00	
Dynamic 	3	450	00:16:40	
Isothermal 	-	450	01:00:00	
Dynamic 	3	400	00:16:40	
Isothermal 	-	400	01:00:00	
Dynamic 	3	350	00:16:40	
Isothermal 	-	350	01:00:00	
Dynamic 	3	300	00:16:40	
Isothermal 	-	300	01:00:00	
Dynamic 	3	250	00:16:40	

Isothermal →	-	250	01:00:00
Dynamic ↘	3	200	00:16:40
Isothermal →	-	200	01:00:00
Dynamic ↘	3	150	00:16:40
Isothermal →	-	150	01:00:00
Dynamic ↘	3	100	00:16:40
Isothermal →	-	100	01:00:00
Dynamic ↘	5	25	00:35:00

Using the experimental data, a fitting of the hydration can be done with “TableCurve 2D” software to find the material property such as mobility parameters and the process activation energy of both OH_0^\bullet and v_0^\bullet will be achieved.

2) TGA experiments for investigating behavior of the sintering shoulder

As we discussed in DIL experiments, the sintering shoulder manifests a special sintering behavior for the samples of batches PM BSZCY151020 and RM BSZCY151020. We, therefore, performed operando TGA measurements on the powder of batch PM BSZCY151020 with temperature profile shown in **Table 13**. The additional information of the sintering behavior around the sintering shoulder have been achieved.

Table 13: Temperature profiles for TGA experiments on raw powders.

Segment mode	Rate (K/min)	Temperature (°C)	Time (hh:mm:ss)
Initial →	25	-	-
Dynamic ↗	450	2	03:32:30
Isothermal →	450	-	01:00:00
Dynamic ↗	1450	2	08:20:00
Isothermal →	1450	-	01:00:00
Dynamic ↘	25	5	04:45:00

4.3 Morphological study

The property of a material is generally determined by its microstructure. The PCCs in this thesis work are fabricated by SSRS starting in the powder phase. They general have a polycrystalline structure with rich grain boundary. The imperfections in the structure result in variations in physical, electrical, and chemical property. Therefore, the microstructure of the PCCs must be investigated to optimize their characteristics in fuel cell applications. In addition to XRD, SEM is another very effective tool to study morphological features, microstructure including crystal grains and grain boundaries, and chemical composition in a PCC made by SSRS. Fractured,

polished, and thermal etched cross-sections have been prepared for SEM measurement. Each sample was mounted on a sample holder of aluminium using carbon tape with the cross-section facing up. The preparation of the samples is described in detail below.

Fractured cross-section: the cross-section of the sample was simply prepared by fracturing the sintered pellet.

Polished cross-section:

The fractured cross-section of the sample was polished with the following polish program,

1. US# 320 for 3 min
2. US# 400 for 3 min
3. US# 500 for 2 min
4. US# 600 for 2 min
5. US# 1000 for 2 min
6. Diamond paste 6 microns for 3 min
7. Diamond paste 3 microns for 3 min

Thermal etched cross-section:

The polished cross-section was heated from room temperature with 2 °C/min rate for 12 hours up to 1475 °C (175 °C below its sintering temperature). Thereafter, the sample was kept at 1475 °C for 3 hours before it was cooled to room temperature again with 2 °C/min cooling rate.

4.4 Electrochemical performance study

Used in hydrogen fuel cells, a PCC will act as the electrolyte and take part in the electrochemical performance. For electrochemical characterization, samples were mounted in a ProboStat cell. The conduction was determined by using EIS. A gas mixer was employed to control the partial pressure of oxygen and water vapor pressure in the atmosphere.

4.4.1 EIS

EIS measurements were done on PM BSZCY151020 – 1650 °C, RM BSZCY151020 w/ YSZ – 1650 °C, and RM BSZCYZn1510202 w/ YSZ – 1600 °C pellets. Sample preparations are described below.

Preparation of Pt-ink electrode

1. The sintered pellet was polished with isopropanol by hand using rough sandpaper US# 320 such that possible contamination on the surface is removed.
2. Pt-ink (Metalor, 6929) was mixed with a little acetone and painted onto the pellet as a circle (5 mm diameter) in the middle. The pellet was put into a heating cabinet at 120 °C for 5 min to dry the Pt-ink, before taking it out and letting it cool down. This was repeated such that both sides of the pellet had 2 layers of Pt-ink.
3. To finish the Pt-electrode, the pellet was fired in a muffle furnace at 750 °C for 1 hour to adhere the Pt-ink to the pellet.

Preparation of current collectors

4. Pt-wire (0.2 mm diameter) was pressed onto Pt-mesh (8 mm diameter) using a cold press with 2 ton force for 1 min.
5. The Pt-wire and Pt-grid was then heated using torch (1400 °C) to strengthen it.

Final setup

6. The pellet was loaded into the ProboStat such that the current collectors were connected on each side of the pellet such that the Pt-mesh was covering the Pt-ink electrodes. Then the pellet was locked in place by springs and alumina tubes.

1. Temperature Dependence of Conductivity

The electronic and ionic conductivity forms the total conductivity of the PCCs. In the hopping process, an activation energy is required to excite the process. For determining the activation energy, conductivity versus temperature dependence measurements, impedance sweeps were done every 50 °C from 700 to 150 °C after reaching equilibrium. By using “Novocontrol Alpha”, sweeps were done from 1 MHz to 0.01 Hz using 10mV rms. The atmosphere was controlled by a gas mixer to be humid Ar with $p_{\text{H}_2\text{O}} = 0.026$ atm. From measured impedances and using **Eq. 46**, the conductivity of different contributions is found and can then be plotted as a function of temperature. The activation energies were determined by using an Arrhenius equation (**Eq. 47**) and the slope of the conductivity plots as shown below.

$$\sigma_i = \frac{L}{(R_i \times A)} \quad \text{Eq. 46}$$

where, i presents the bulk or grain boundary. R_i can be found from the EIS curves.

R_i is the i resistance

From Eq. 38, we have

Eq. 47

$$\begin{aligned}\sigma_i T &= A \exp(-E_{a_i}/RT) \\ \ln \sigma_i T &= \ln A + \left(-\frac{E_{a_i}}{R}\right) \cdot \frac{1}{T} \\ \text{slope}_i &= \left(-\frac{E_{a_i}}{R}\right)\end{aligned}$$

2. p_{O_2} dependency of conductivity

The electronic and ionic conductivity forms the total conductivity of the PCCs. In the hopping process at an operation temperature, the conductivity strongly depends on the operating atmosphere due to the change of the concentration of electronic and structural defects. By changing the oxygen partial pressure, the $v_{\text{O}}^{\bullet\bullet}$ and $\text{OH}_{\text{O}}^{\bullet}$ concentration in a PCC will change, therefore the conductivity of the PCC. The conductivity was, moreover, measured as a function of the oxygen partial pressure at 600 °C by impedance spectra measurements in the humid atmosphere ($p_{\text{H}_2\text{O}} = 0.026$ atm) of HArMix, HArMix+Ar, and then Ar+O₂ with variable O₂. The impedance spectra were recorded at different p_{O_2} and fitted using the Zview software equivalent circuit models with circuit elements resistors R_i and constant phase elements CPE of the form $R_u(R_b \text{CPE}_b)(R_{gb} \text{CPE}_{gb})(R_e \text{CPE}_e)$ for PM BSZCY151020-1650 °C. Subscripts b denotes the bulk, gb the grain boundary and e the electrode contributions, respectively, referred according to their capacitances. Bulk and grain boundaries had capacitances of the order of 10^{-12} and 10^{-9} Fcm⁻¹, respectively, while area specific capacitances for electrodes were of the order of 10^{-6} F cm⁻² [18].

4.4.2 Transport Number Measurement by Electromotive Force

Electromotive force (EMF) experiments were done on the sample PM BSZCY151020 – 1650 °C at 700 °C. This was done by exposing the sample with two different atmospheres on each side. This way a chemical gradient is established, resulting in transport of charged species through the sample. The force driving this charge transfer can be modeled as a voltage, e.g., EMF. By determining the EMF, the transport number could be achieved. To measure the transport of oxygen ions and protons, we used a hydrogen concentration cell to measure the transport of oxygen ions and protons following the steps as below.

1. The sample was loaded into the ProboStat thereafter, we used ceramic sealing to separate the inner tube atmosphere and outer tube atmosphere.
2. The ceramic sealing was made by mixing the ceramic powder (CERAMABOND 571-P POWDER Lot No. 571-P-1217) with a liquid activator (CERAMABOND 571-L LIQUID ACTIVATOR Lot No. 571-L-1217) in a 1.5:1 ratio by weight.
3. The ceramic sealing was applied to seal the connection between the sample pellet and the inner support-tube (**Fig. 21**), before firing it at 750 °C for 3 hours.
4. We connect the ProboStat with 2 inlets and 2 outlets for the different atmospheres, e.g., “IN” for inner tube and “OUT” for outer tube. We supply a humid Ar + H₂ atmosphere in OUT and a humid H₂ atmosphere in IN to make the hydrogen concentration cell, seen in **Fig. 21** below. The humidity was the same in both sides. The voltage was measured across two electrodes indicated as V_{EMF}.

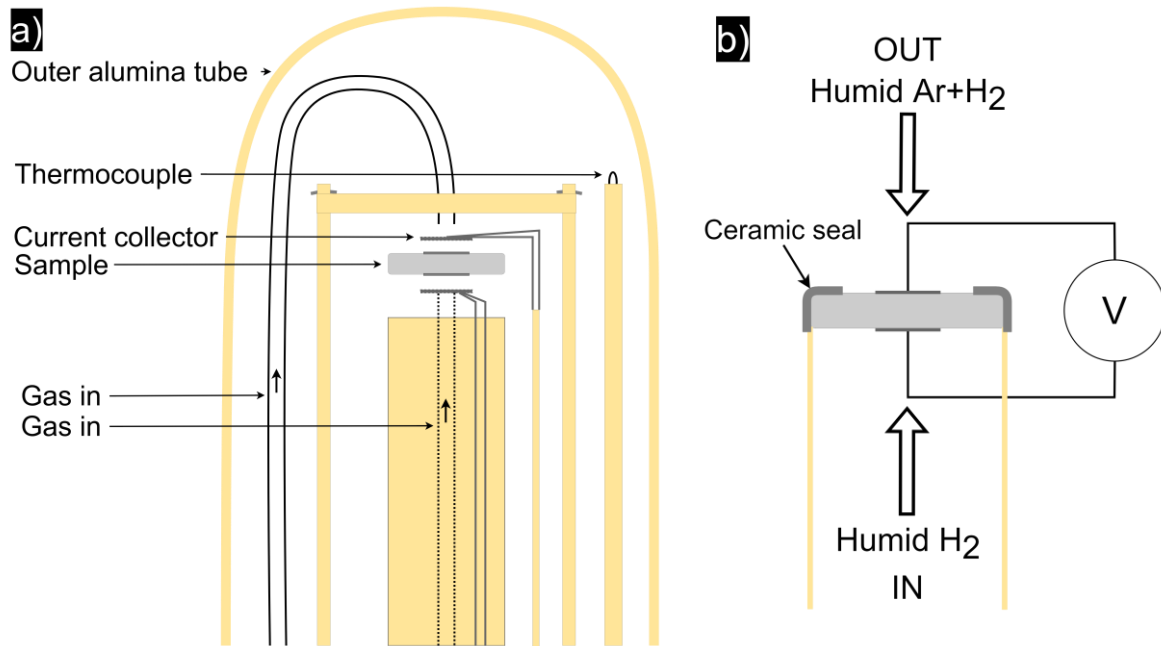


Fig. 21: Schematic plot for the hydrogen concentration cell

The voltage as a function of $\ln\left(\frac{p_{H_2}}{p'_{H_2}}\right)$ were plotted. The transport number of oxide ions and protons can be found following **Eq. 48** [20].

$$V_{EMF} = (t_{H^+} + t_{O^{2-}}) \frac{RT}{2F} \ln\left(\frac{p_{H_2}}{p'_{H_2}}\right) \quad \text{Eq. 48}$$

where,

p_{H_2} = partial pressure of H_2 in IN

p'_{H_2} = partial pressure of H_2 in OUT

From the plot of V_{EMF} versus $\ln\left(\frac{p_{H_2}}{p'_{H_2}}\right)$, we can determine the slope of the curve and thus the transport number as **Eq. 49**,

$$t_{H^+} + t_{O^{2-}} = \frac{\text{slope}}{2F} RT \quad \text{Eq. 49}$$

5 Results and Discussions

In this chapter, we summarize the experimental results and analyze the findings to conclude the sintering behavior and conductivity of PCCs that we are developing. We have designed 4 material batches by varying parameters in the fabrication process, precursors, and sintering additives as dopants. Their chemical compositions, crystal structures, imperfections, material physical properties, electrochemical behavior, and electrical performance are studied by advanced lab analysis tools and methods.

This chapter is organized into three sections. In the first section, we present the results which are from the series study of sintering behavior including DIL, XRD and SEM measurement. We discuss the reasons and mechanisms for the discovered sintering phenomenon. In the second section, we report the achievements which are from operando HT-XRD characterizations. The study of TEC of the materials are described. The optimization concept will be discussed in terms of increasing TEC without scarifying their conductivity. In the last section of this chapter, we analyze the factors and how that affect the conductivity of the PCC materials using their microstructure SEM images and XRD results, water uptake TGA curves, and electrochemical performance EIS and EMF data.

5.1 Investigation of Sintering Behavior

The composition and fabrication process are the key factors that determine the microstructure and property of the materials. The PCCs used in a fuel cell must be mechanically, physically, and chemically stable. The cracks, pinholes, and stress distribution if a PCC will affect the performance and durability of the fuel cell. Through high-temperature sintering process, the green body expansion and shrinkage versus the temperature will give very important information about the sintering of the PCCs. The DIL experiments have been done as an important part of the experimental work at the beginning of the thesis work. The SEM picture below (Fig. 22) present the pinholes in one of our samples.

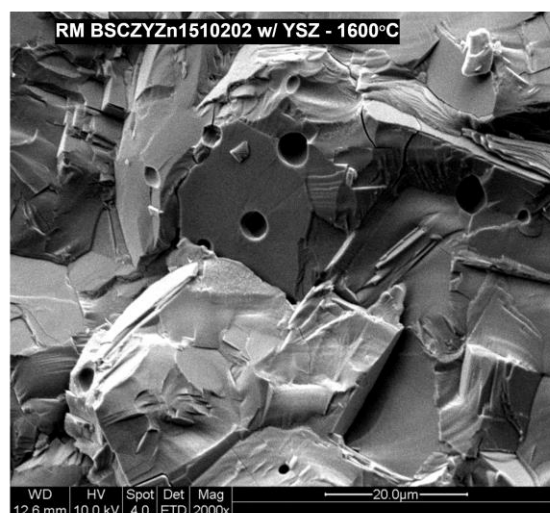


Fig. 22: SEM picture of fractured cross-section that shows pinholes in the structure.

5.1.1 Sintering Shoulder Discovered by DIL Experiments

The recorded data during the DIL experiments are presented by plotting the relative dimension change (dL/L_0) and the temperature ($^{\circ}\text{C}$) versus sintering time (min) as shown in the following figures.

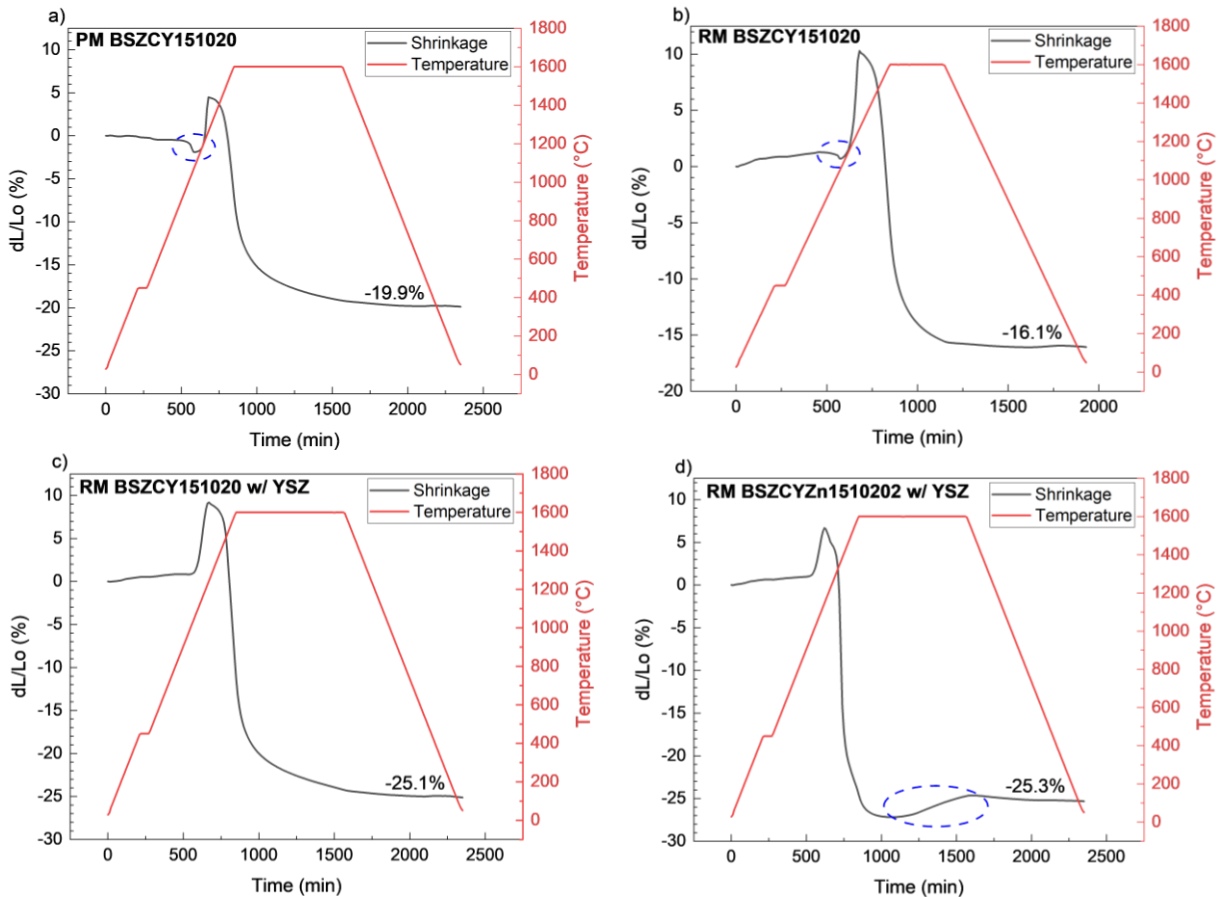


Fig. 23: Results from Dilatometer measurements on the samples, a) PM BSCZY151020, b) RM BSZCY151020, c) RM BSZCY151020 w/ YSZ, and d) RM BSZCYZn1510202 w/ YSZ.

From the figures above, we observe the DIL curves in a large range of temperatures. We can find that above 1100°C , an expansion occurs for all samples. The samples then shrink at different temperatures. We brief the major results in **Table 14** below.

Table 14: Initial Values and Results

Batch Name	Initial length (mm)	Total Shrinkage (%)	Expansion T ($^{\circ}\text{C}$)	Shrinkage T ($^{\circ}\text{C}$)
PM BSZCY151020	5.34	19.9	1084	1265
RM BSZCY151020	5.73	16.1	1066	1266
RM BSZCY151020 w/ YSZ	5.37	25.1	985	1245
RM BSZCYZn1510202 w/ YSZ	5.20	25.3	945	1145

We did not observe any surprises in the samples RM BSZCY151020 w/ YSZ, and RM BSZCYZn1510202 w/ YSZ, shown in **Fig. 23 c) & d)** respectively. However, a new phenomenon was found in both curves shown in **Fig. 23 a) & b)** marked with blue dash-line circles, where we can see that samples PM BSCZY151020 and RM BSZCY151020 start to shrink at a relatively low temperature and thereafter to expand before shrinking again at a relatively high temperature. We name this discovered phenomenon as the sintering shoulder. In addition, the concave region marked by blue circle in **Fig. 23 d)** appears. Obviously, sintered PCC through multi shrink and expansion periods will cause the mechanical defects that have been observed as the cracks in both PM BSCZY151020 and RM BSZCY151020 samples. More experiments therefore have been done to investigate the sintering behavior for material optimization.

5.1.2 The Causes of Sintering Shoulder

The shoulder appears at the beginning of the sintering where the green body experiences temperatures well below 1400 °C. Both temperature and time periods do not support any massive solid-state reaction in the green body. Therefore, a phase change or decomposition of a precursor at such temperature could be the reason for the sintering shoulder.

5.1.2.1 HT-PXRD for Identifying the Phase Formation

To support our analysis, HT-PXRD have been done and the results are given in **Fig. 24**.

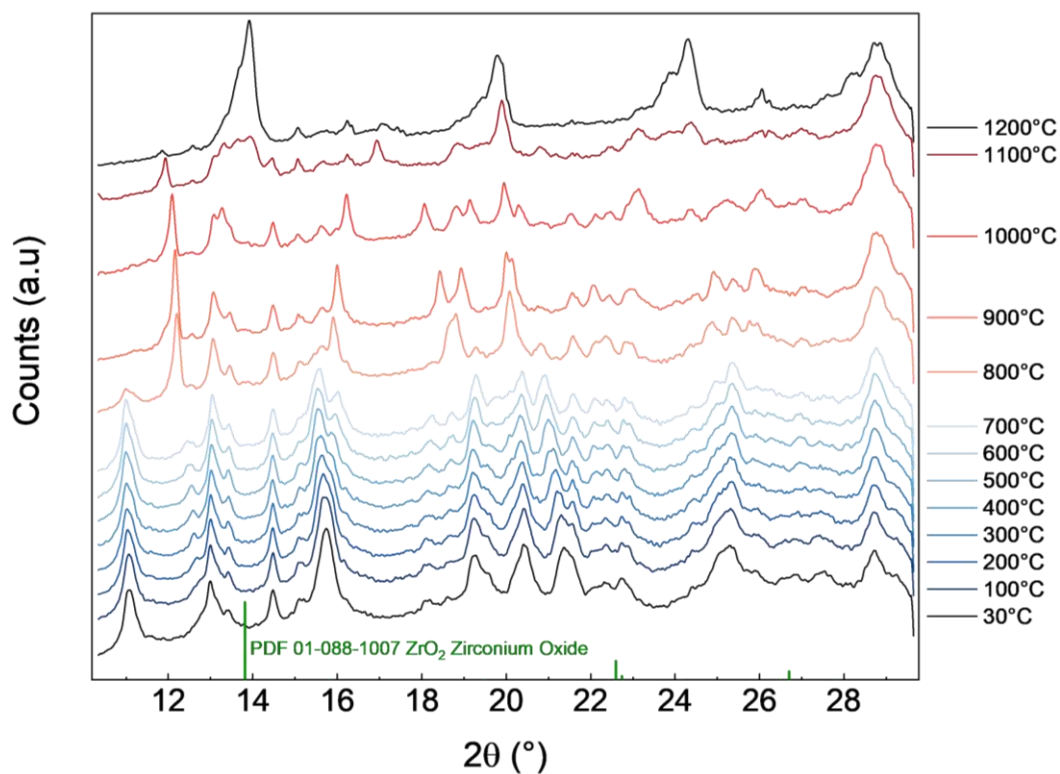


Fig. 24: Diffractograms for HT-PXRD of PM BSZCY151020 - 1650°C

From the results above, we observe no phase change for temperatures below 800 °C. Above 800 °C new phases appear, which do not present the solid-state reaction for the final PCC. We cannot conclude by looking at **Fig. 24** and **Fig. 25** that the XRD pattern at 1200 °C is comparable to the standard XRD of PM BSZCY151020 – 1650 °C.

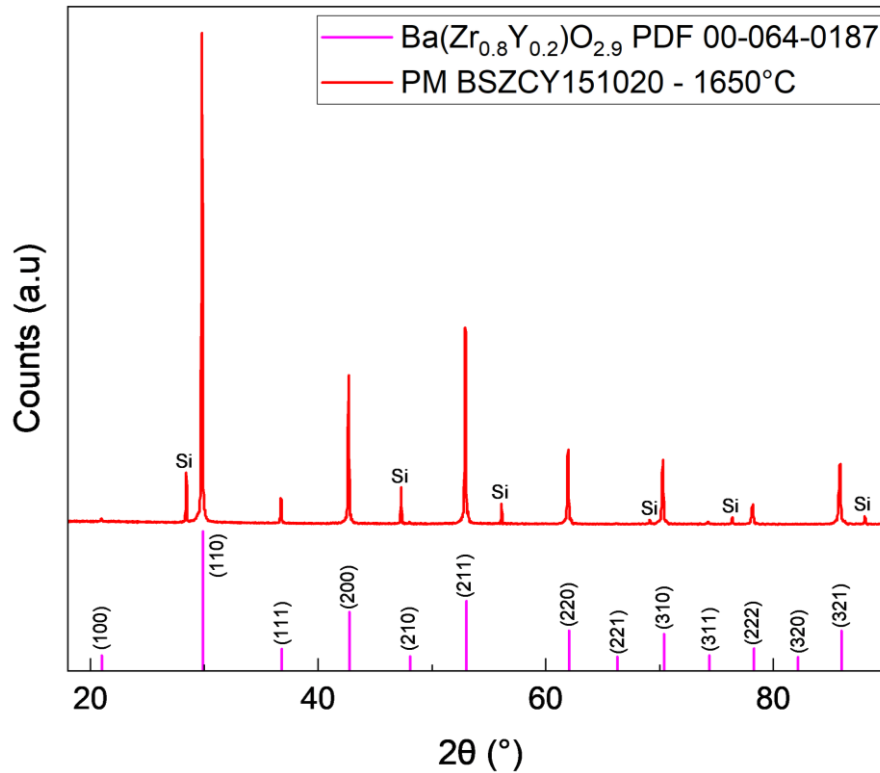


Fig. 25: XRD pattern of PM BSZCY151020 – 1650 °C and BZY pdf from the Diffrac.eva data base

5.1.2.2 BaCO₃ Decomposition Analysis

We have learned from the literature that BaCO₃ has low decomposition temperature [21]. Therefore, we conduct extra DIL experiments on the green bodies PM BSZCY151020 and BaCO₃ up to the temperature of 1134 °C. The results are shown in **Fig. 26**.

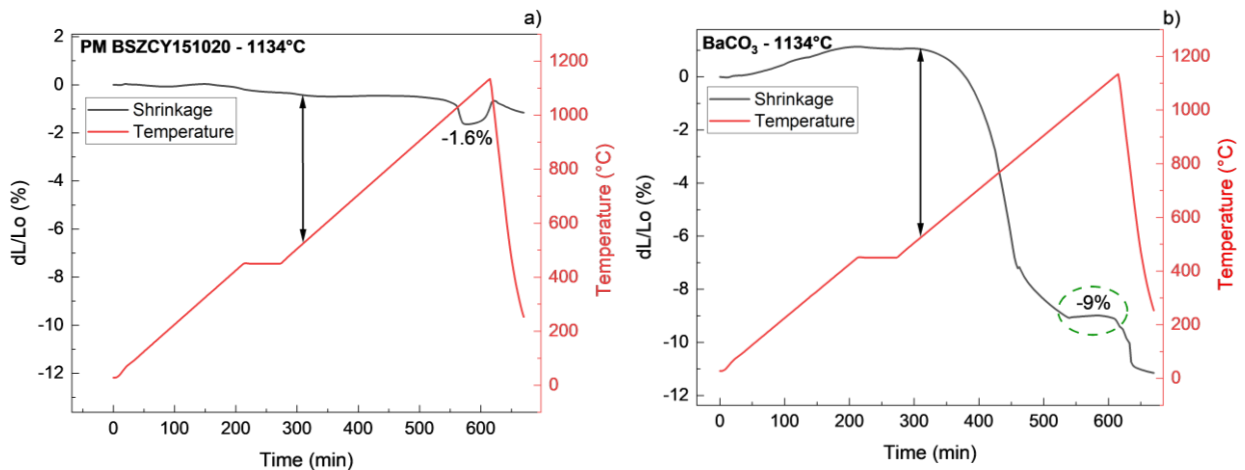


Fig. 26: Results from Dilatometer measurements on the samples, a) PM BSZCY151020 and b) BaCO₃.

From the figures above, the slight shrinkage of the PM BSZCY151020 sample before the sintering shoulder, can be the contribution of BaCO₃ decomposition, see the arrows in **Fig. 26**,

which indicate the shrinkage of PM BSZCY151020 and BaCO₃ at same temperature of about 525 °C. However, in the temperature range where the sintering shoulder appears, the DIL curve of BaCO₃ is flat, see the green dashed-line circle marked in **Fig. 26 b**). Therefore, we can confirm that BaCO₃ cannot be the reason for the sintering shoulder.

5.1.2.3 The Impact of ZrO₂ Phase Transition

The composition of all samples is almost the same, but we notice that samples without the sintering shoulder were made by Y_{0.16}Zr_{0.92}O_{2.03} (YSZ) precursor instead of ZrO₂. We certainly are encouraged to conclude that the sintering shoulder is a result of the earlier phase change of ZrO₂, which is also supported by the fact that ZrO₂ is known to have monoclinic structure below 1170 °C, tetragonal between 1170 °C and 2370 °C [22]. The phase change at 1170 °C coincides well with the temperature of the sintering shoulder. Telling from **Fig. 24** the tetragonal ZrO₂ is well identified by the XRD pattern at 1200 °C. As a conclusion, for optimizing the fabrication of the mechanically durable PCC, Y_{0.16}Zr_{0.92}O_{2.03} should be used as the precursor instead of ZrO₂ in the future investigation.

5.1.3 Sintering Behavior After the Sintering Shoulder

After the sintering shoulder, from **Fig. 23** we find that all samples start a significant expansion sharply above 1100°C. At the final sintering temperature, all samples shrink quickly about 20% to 25% respectively. As discussed above, the time for samples under high temperature to the moment of expansion was not long enough to have significant solid-state reaction, the expansion must be the behavior of the precursors under the elevated temperature in that short period. The operando TGA of precursors at dried air has been performed and the results are presented in **Fig. 27**. The results will be discussed by analyzing behavior of BaCO₃ and ZnO at elevated temperatures.

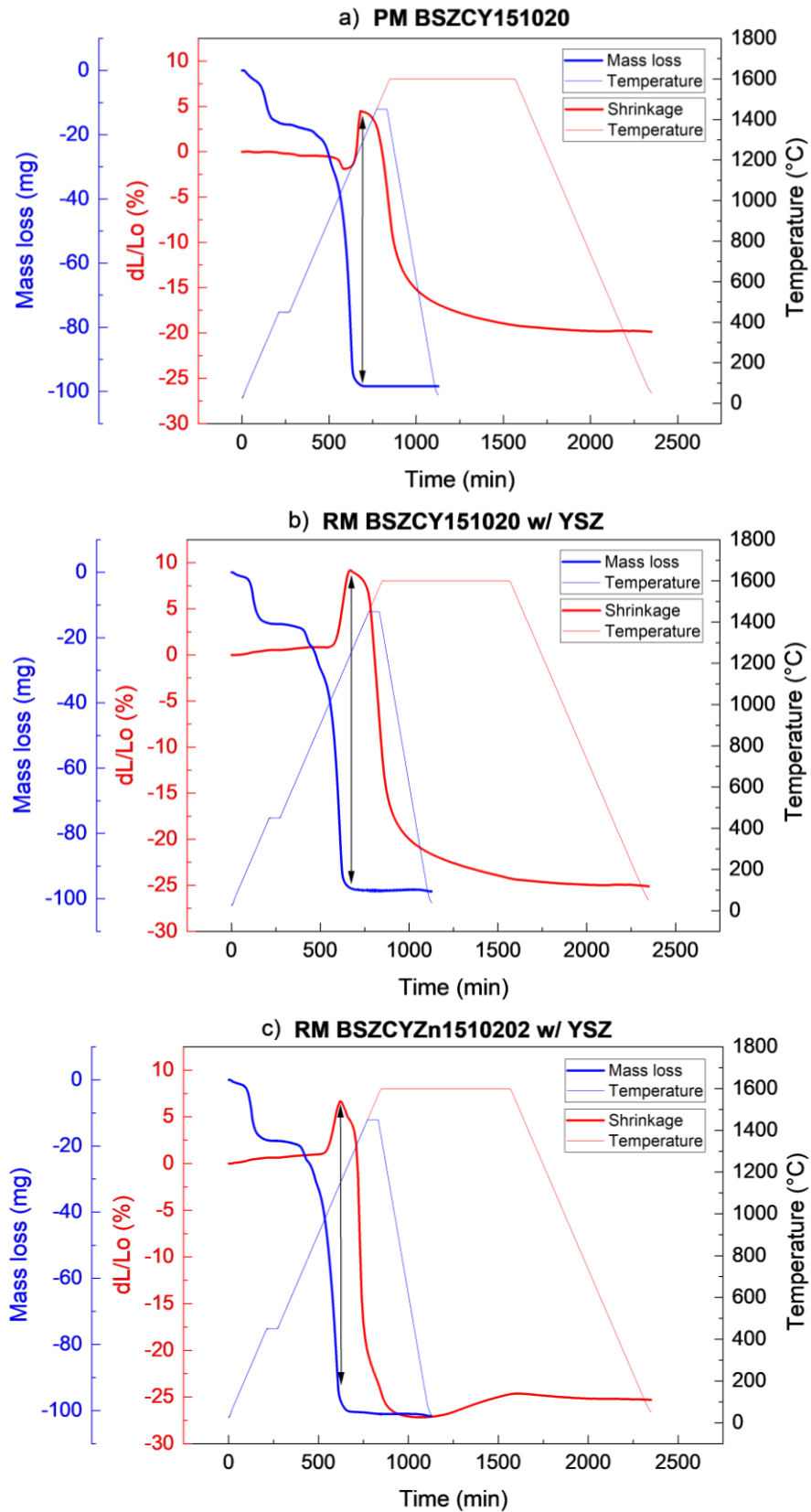
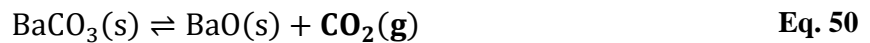


Fig. 27: The results of operando TGA of precursor of relative green body, combining the DIL experiments of the green body.

5.1.3.1 CO₂ Exiting due to BaCO₃ Decomposition

From the figures above, we observe identical behavior in the TGA curves for all samples. There is some mass loss in the start phase and significant mass loss at about 850 °C and 750 °C. Surprising enough, for all samples, the significant mass loss happens when the samples start to expand significantly, mass loss stops at the start of the samples shrinkage, see the arrow indication in **Fig. 27**. This behavior can be understood by analyzing BaCO₃ decomposition. From [21], decomposition of BaCO₃ happens above 750 °C while CO₂ exits following the chemical reaction below,



DIL measurement show a sharp expansion due to the CO₂ accumulating in the sample and exiting, which is detected by TGA the mass loss measurement. After CO₂ exiting completes in a short period, the push rod in DIL will return and follow the slow shrink of solid-state reaction, which gives a significant shrink of the sample just after the CO₂ exiting.

5.1.3.2 Impact of ZnO Evaporation

As we have seen from **Fig. 23 d)** the concave appears in the DIL curve. This only happens when we use ZnO as additive. It is well known that ZnO can evaporate at an elevated temperature. Babilo et al. reported the same dependence (**Fig. 28**), which has been explained with the following reaction equation [23].



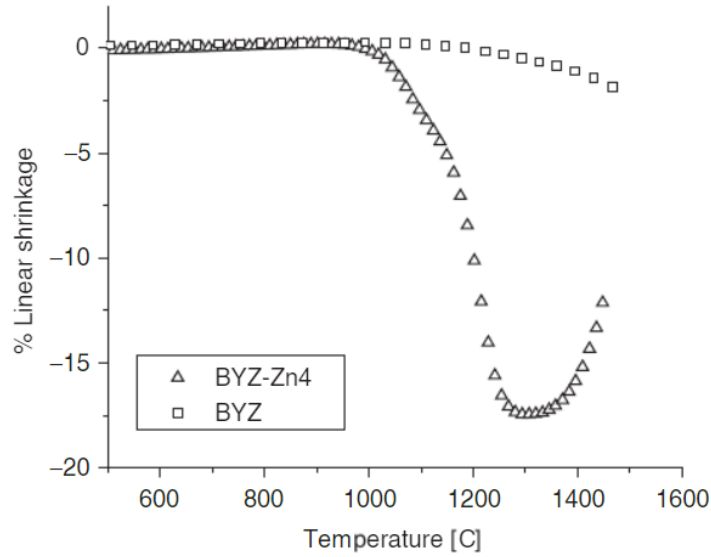


Fig. 28: The concave in the DIL curve reported by Babilo et al. [23]

5.1.4 Completion of Sintering Process.

After the sintering process mentioned in chapter 4.1, the samples were examined by both XRD and SEM at room temperature. The **Fig. 29** below shows the PXRD patterns for all samples.

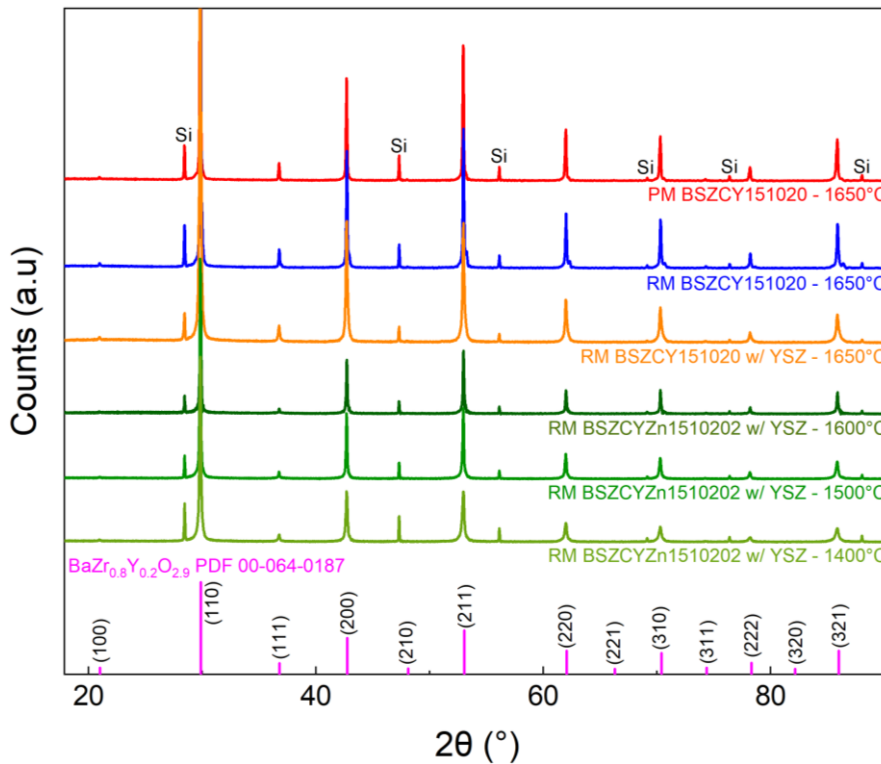
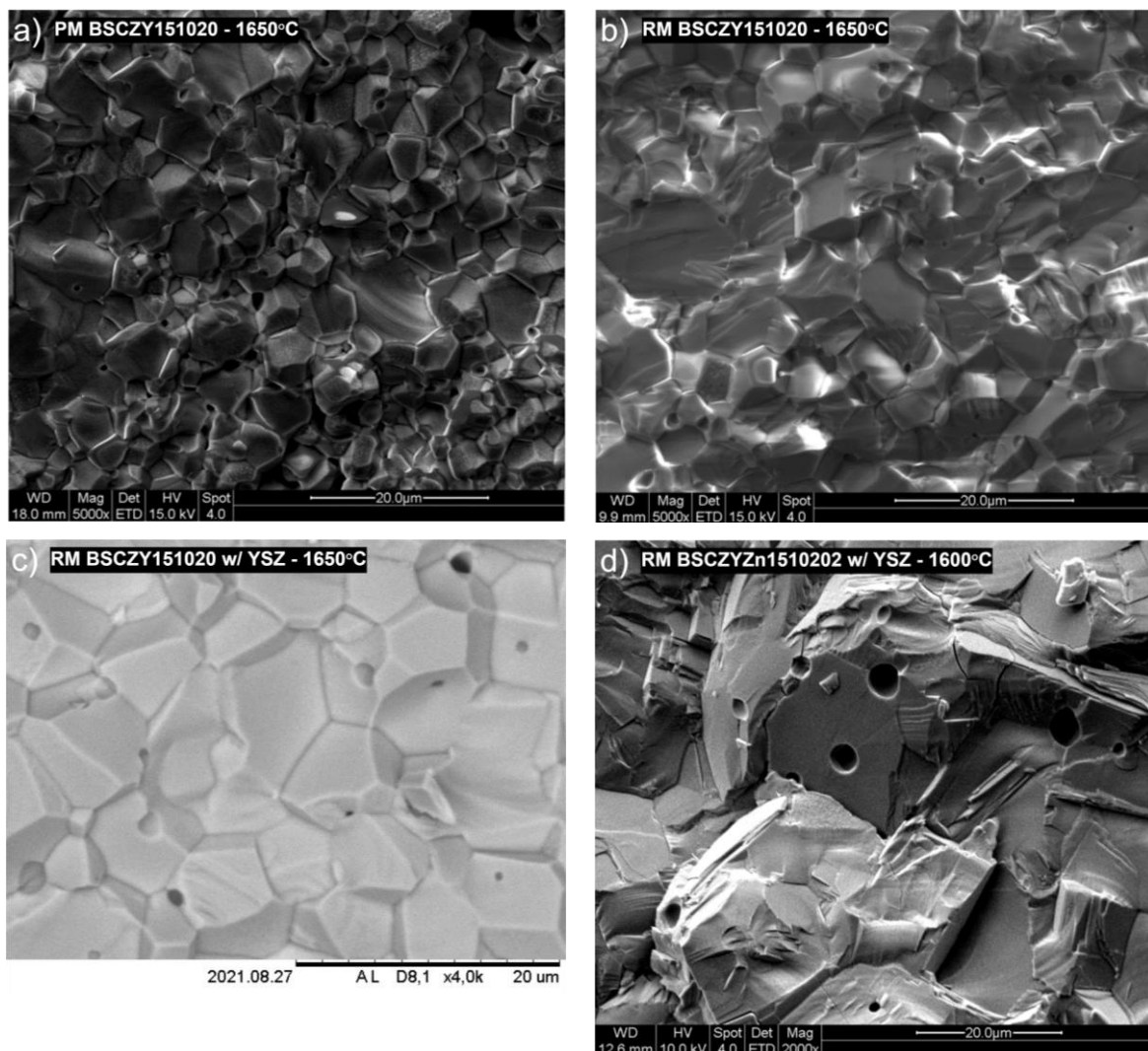


Fig. 29: PXRD pattern of all 5 samples plus XRD pattern from the data base «PDF-2 Release 2014 RDB» in Diffrac.eva software for cubic crystalline BZY

It is clear from **Fig. 29** that $\text{BaZr}_{0.8}\text{Y}_{0.2}\text{O}_{2.8}$ cubic crystalline is formed when the sintering temperature was above $1400\text{ }^{\circ}\text{C}$. The SEM images of fractured cross-sections from all samples are shown in **Fig. 30** below. For the sample sintered at $1400\text{ }^{\circ}\text{C}$ **Fig. 30 f)**, we see powders of some precursors. Combining the XRD and SEM results, it is proved that SSRS does not complete at $1400\text{ }^{\circ}\text{C}$ in about 40 hours process. Increase the sintering temperature above $1500\text{ }^{\circ}\text{C}$, the SSRS completes for all samples. The polycrystalline is the typical structure of all designed PCCs. The distribution of the crystal grains and grain boundary can be better displayed using the thermal etched cross-section (**Fig. 31**).



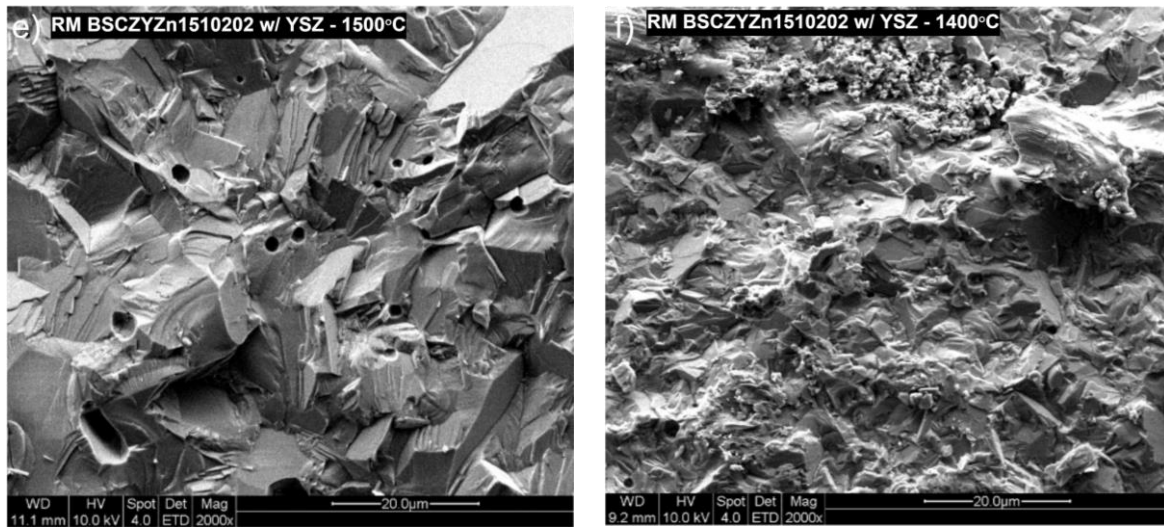


Fig. 30: SEM pictures of fractured cross section of the 6 samples

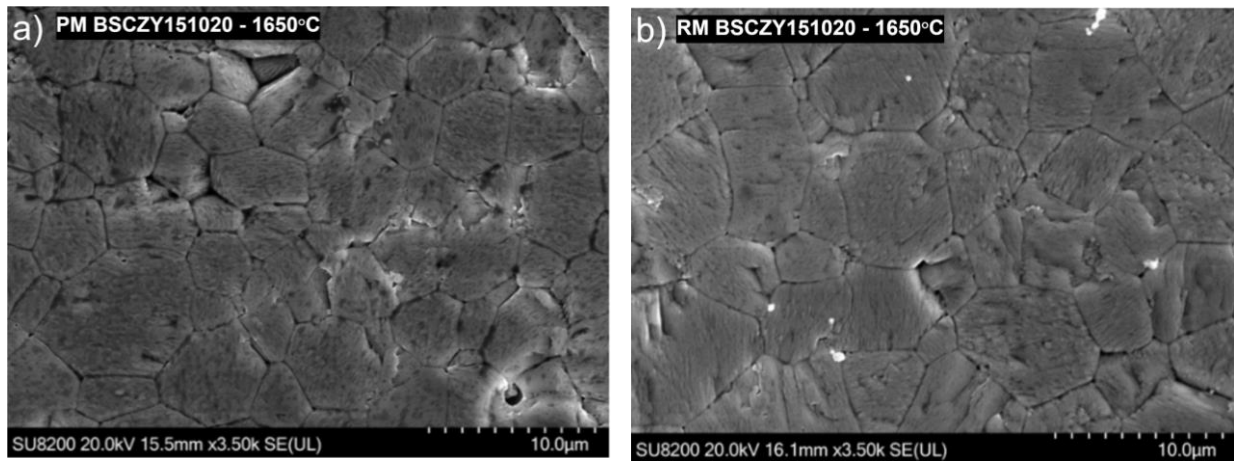


Fig. 31: SEM pictures of thermally etched cross sections

From figure **Fig. 31**, we see ball-milling method do have the effect to the microstructure of the samples. The grain distribution for both PM and RM samples is quite homogeneous after the completion of the sintering process. It seems that the grain dimension of PM is slightly smaller than that of RM, which is due to the PM is high energy milling comparing to the RM. The grain size distribution estimated by SEM of the thermal etched cross-section are given in **Fig. 32** for the 2 samples. The data were calculated by using 20 grains in each sample. For the length measurement, each grain was measured from several angles.

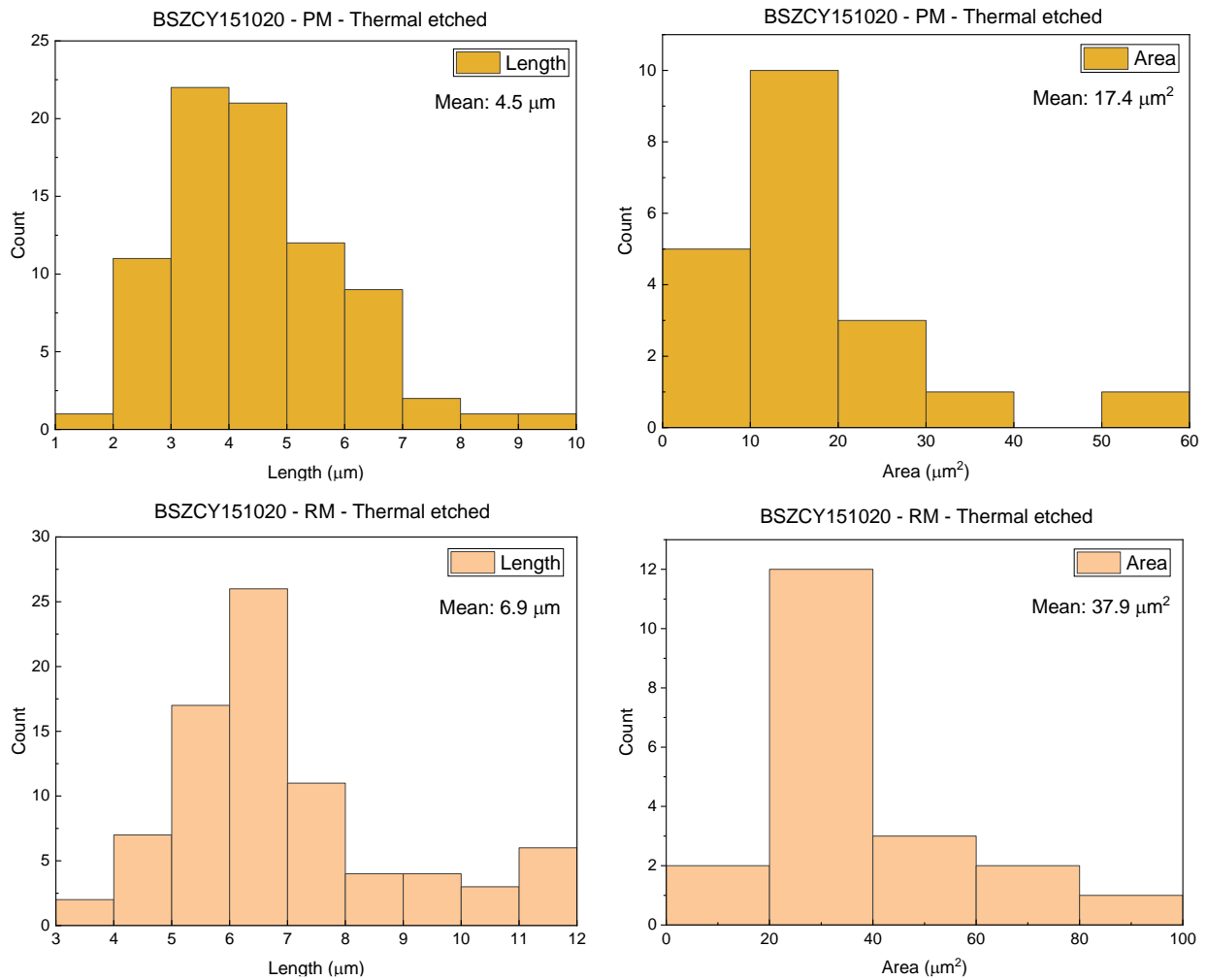


Fig. 32: The grain size distribution estimated by SEM of thermal etched cross-section.

5.1.5 Relative densities of PCCs after the sintering

Relative densities were calculated by using the theoretical density for BSZCY151020, $6.1 \frac{\text{g}}{\text{cm}^3}$.

The sample densities before and after sintering are listed in **Table 15**.

Table 15: Sample densities before and after sintering

Sample name	Pellet	Green density ($\frac{\text{g}}{\text{cm}^3}$)	Experimental Density ($\frac{\text{g}}{\text{cm}^3}$)	Relative density (%)
PM BSZCY151020 1650 °C	a)	-	5.99	98
	b) cracked	-	5.65	93
RM BSZCY151020 1650 °C	a)	-	5.94	97
	b) cracked	-	5.56	91
RM BSZCY151020 w/ YSZ 1650 °C	a) cracked	2.78	5.85	96
	b)	2.78	5.81	95
	c) cracked	2.78	5.77	95
	d) cracked	2.77	5.72	94
RM BSZCYZn1510202 w/ YSZ	a)	2.7	5.7	93
	b)	2.7	5.8	94

1600 °C	c)	2.8	5.7	94
RM BSZCYZn1510202 w/ YSZ 1500 °C	a)	2.8	5.8	95
	b) cracked	2.8	5.4	91
	c)	2.7	5.8	95
RM BSZCYZn1510202 w/ YSZ 1400 °C	a)	2.9	5.5	89
	b)	2.8	5.5	90
	c)	2.8	5.5	90

The data show that at the sintering temperature of 1400 °C, the relative density of the sample was only equal to 90%. Considering XRD and SEM results above, this low relative density supports the conclusion that the SSRS does not complete, and the powders of precursors existing in the sintered sample reduce the relative density. Although the sintering temperatures and sintering time are different, for samples RM BSZCY151020 w/ YSZ-1650 °C, 3/4 sintered pellets had a vertical crack, but when ZnO was doped as sintering aid, only 1/9 sintered pellets had a vertical crack. This is a significant increase in success rate of sintered pellets, from 25% to 89% while using more effective sintering profiles.

Summary, the sintering shoulder was discovered the first time in our research group. The mechanisms for the sintering shoulder were studied in detail, and we find that ZrO₂ phase transition at 1170 °C is the most likely reason for the sintering shoulder. The behaviour of the sintering after the sintering shoulder is well understood after this thesis work by analysing the HT-XRD of the green bodies, the DIL curves of designed materials, mass loss TGA analysis, the SEM of the sample microstructure, and the relative densities of the sintered samples. The BaCO₃ decomposition result in the significant expansion and sharply shrinking just after the sintering shoulder. ZnO evaporation causes the concave in the DIL curve just after the sharply shrinking. The PM will result in a smaller crystal grain and homogeneous distribution.

5.2 The TEC of the PCCs.

The challenge of using PCCs in a fuel cell is the mismatch of the TEC of different materials. The TEC of PCC is smaller than the TEC of the metal electrodes and packaging materials, which will cause short lifetime of the fuel cell in operation. Increasing the TEC of PCC to match that of the electrode metal is one of the topics when we develop the high conductivity PCCs. In material designs, additives such as Sr and Ce substituting Ba and Zr aim to increase the TEC of BZY, so that BSCZY151020 is designed and tailored with dopant ZnO₂ or with precursor YSZ instead of ZrO₂. HT-XRD experiments were done to determine the TEC of the PM

BSCZY151020-1650 °C. Unfortunately, we are not able to access the HT-XRD facility for studying other 3 designed materials due to the lab responsible engineer moved to another job.

5.2.1 Lattice Constants of the Samples at Room Temperature

At room temperature, the sintered samples all went through PXRD measurement. The results are given in **Fig. 29**, from which we can determine the lattice constant of each sample as shown in **Table 16**.

Table 16: Lattice parameter extracted from refinement

Sample	Lattice parameter a (Å)	Error
PM BSZCY151020 – 1650 °C	4.2313	0.0002364
RM BSZCY151020 – 1650 °C	4.2285	0.0002051
RM BSZCY151020 w/ YSZ – 1650 °C	4.2430	0.01033
RM BSZCYZn1510202 w/ YSZ – 1600 °C	4.2328	0.001180
RM BSZCYZn1510202 w/ YSZ – 1500 °C	4.2323	0.002756
RM BSZCYZn1510202 w/ YSZ – 1400 °C	4.2372	0.005001

In **Table 16**, the biggest error marked with yellow field happens for the sample RM BSZCY151020 w/ YSZ - 1650°C, which we do not know the reason. From above discussion, we know that the sample RM BSZCYZn1510202 w/ YSZ – 1400 °C was not fully sintered. Considering the other 4 samples, we can conclude that the lattice constant of fully sintered BSZCY samples is about 4.2299 ± 0.0014 Å, and RM BSZCYZn1510202 samples is about 4.2326 ± 0.0002 Å. Comparing to the lattice constant of cubic BZY 4.2268 Å from «PDF-2 Release 2014 RDB» in Diffrac.eva software. It is clear that by doping Sr and Ce, the lattice constant of BSZCY is slightly bigger than that of BZY. The Sr has smaller atom size than Ba (1.18 Å versus 1.61 Å). However, Ce with a relatively larger atom size than Zr (0.87 Å versus 0.72 Å). It is clear that Ce should be the reason for increased lattice constant after the doping in BZY. The increased lattice constant for BSZCY comparing to BZY has also discovered (4.2273 Å versus 4.2268 Å) [7]. The sintering aid ZnO enables the low sintering temperature for sample RM BSZCYZn1510202 w/ YSZ which has a very similar lattice constant at both sintering temperature 1600 °C (4.2328 Å) and 1500 °C (4.2323 Å). Without ZnO, the lattice constants of PM BSZCY151020 and RM BSZCY151020 both sintered at 1650 °C are 4.2318 Å and 4.2285 Å respectively, which are smaller than that of the samples with ZnO. Therefore,

ZnO sintering aid will lower the sintering temperature to 1500 °C and increase slightly the lattice constant.

5.2.2 HT-XRD and TEC

Operando HT-XRD experiment in the temperature range of 25 °C to 1200 °C have been done on the sample PM BSCZY151020-1650 °C. The XRD patterns were recorded during heating and cooling in dried air in the condition of waiting 10 min at each measurement temperature. The results are shown in **Fig. 33**.

PM BSZCY151020 - 1650 °C after water uptake

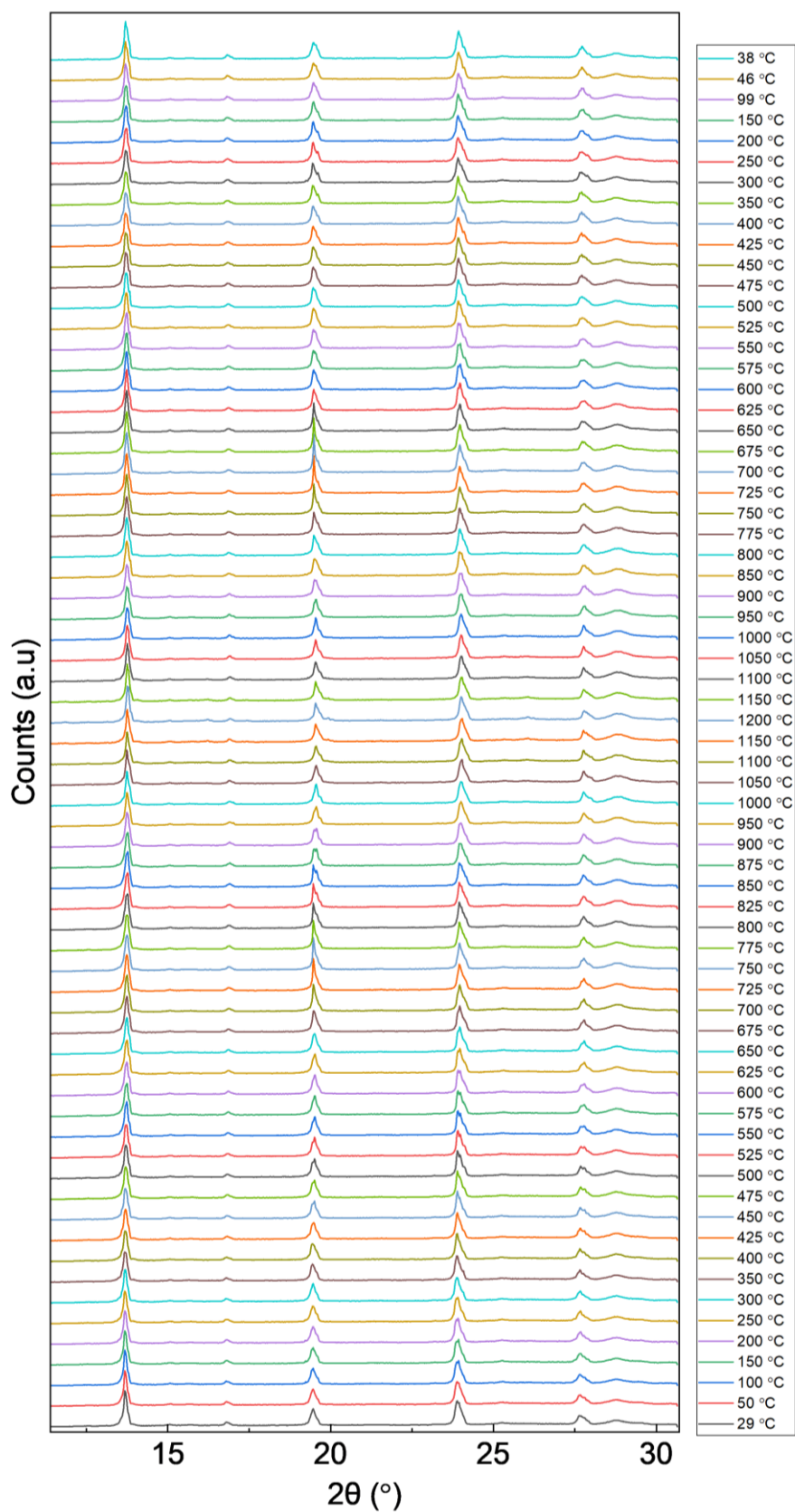


Fig. 33: HT-XRD experimental results for sample PM BSZCY151020 – 1650 °C at temperatures from 29 °C to 1200 °C and from 1200 °C to 38 °C

A single-phase were observed from all the XRD patterns within the applied temperature range, which could be indexed according to the cubic $Pm\bar{3}m$ space group. The lattice parameter of the PM BSCZY151020-1650 °C versus temperature is presented in **Fig. 34**.

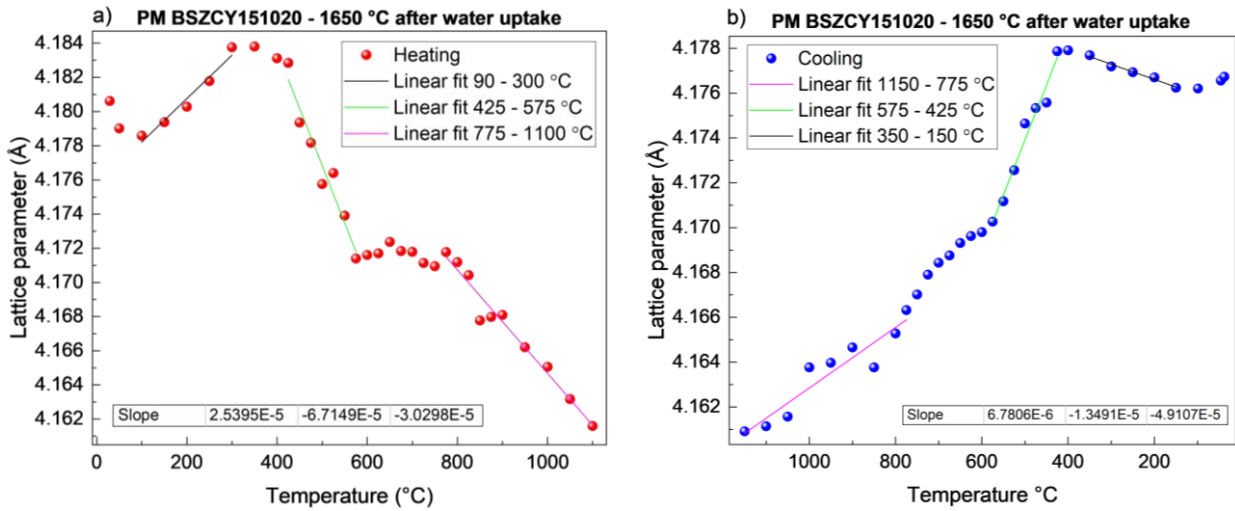


Fig. 34: Lattice parameter of PM BSCZY151020-1650 °C versus temperature. a) measured as temperature rising, b) measured as temperature decreasing.

From figure **Fig. 34**, we find that in a large temperature range, the sample shrinks with temperature increase when measurements were done in heating process and the sample expands with temperature decrease when measurements were done in cooling process. In other words, the negative TEC was observed in both cooling and heating processes. To our knowledge, PM BSCZY151020-1650 °C is not a material with negative TEC, which is also approved by Masoud's results who published the normal TEC of around 10 ppm/K for the same composition measured on the same apparatus [7]. We do observe the positive TEC (60ppm/K) in the heating process from room temperature to 200 °C, but positive TEC does not appear in the cooling process from 200 °C to room temperature. One can also find that the two segments in **Fig. 34** are well repeated in both heating and cooling processes. We are sure the negative TEC is the correct results achieved in our measurement condition although the results sound odd. The discussion within our group on these results is given below.

The sample used in our HT-XRD measurement was after TGA measurement, which means that hydration has fully occurred in the sample before HT-XRD. It is hard to understand that we find the negative TEC of the sample under test (SUT) in a large temperature range. Perhaps, the dehydration in the heating process could happen and the negative TEC was resulted. In the

cooling process, the hydration may have occurred due to lack of humid atmosphere, in which, however, we see the negative TEC too.

1. David: Odd, these materials aren't usually negative thermal expanders. I've checked the original data and you definitely haven't confused the temperatures. The initial change up to around 200 °C on heating is probably due to dehydration. It also seems to reverse to some extent on cooling (this seems to have been done under normal atmosphere- I'm assuming the water uptake means the sample would be pre-loaded with high levels of water). The results of the fitting agree with the raw data. You haven't made a mistake that I can see. This is just a weird result. Have you seen anything similar for other compositions close to this?
2. Prof. Truls Norby comments as the following: Thanks, David and Henry, for working to sort this out. I look forward to Masoud's response, but he has published the normal TEC of around 10 ppm/K for the same composition measured on presumably the same apparatus. I have never heard of anything like this. What is the value of the negative TEC?
3. Masoud: As Prof. Truls Norby mentioned, we have examined the TEC of this material. One thing that I am wondering about is that the peaks at ~18 and ~24 degrees are a little odd. It seems they are not repressive of a single-phase or a cubic structure! How long was the dwell time at each temperature? In my case, before the XRD measurement, we stayed for 30 min at each temperature to reach the equilibrium

As a conclusion, we have observed surprising experimental results that indicate a negative TEC of the SUT in our measurement conditions. We have not achieved agreement within our team on the reason to interpret the results. Unfortunately, we did not get time and facility to repeat the measurements for verifying the findings. This shall be an important task for the next master project.

5.3 The conductivity of the PCCs

5.3.1 Defect Concentration Analysis Using TGA

Operando TGA experiment is a particularly useful approach for studying hydration reaction in the samples. It provides us with highly effective tool for measuring the water uptake versus temperature, thus the concentration $[\text{OH}'_0]$ versus temperature. All 6 samples after completing the sintering were measured and the results are shown in **Fig. 35**.

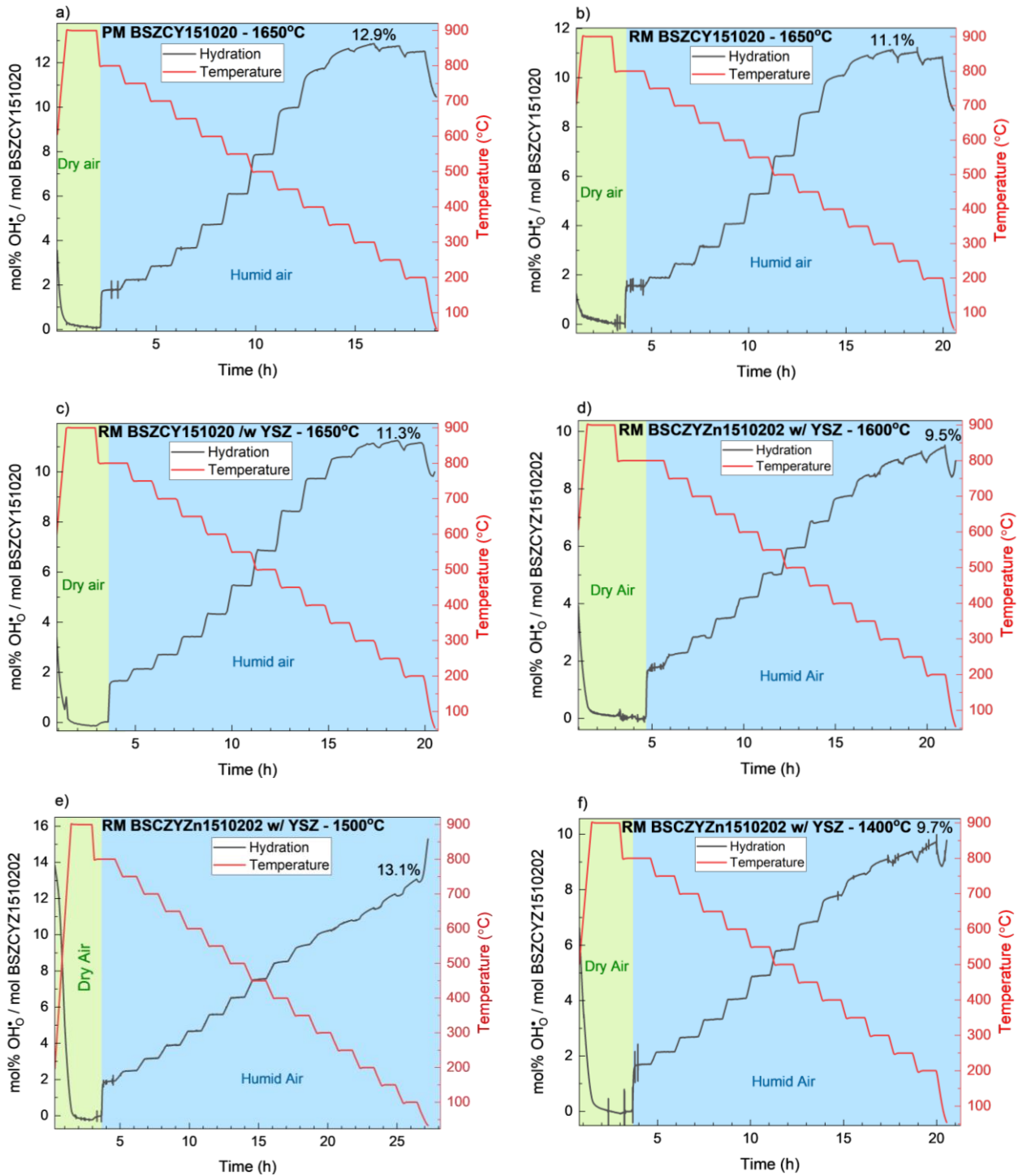


Fig. 35: Water uptake of a) PM BSZCY151020 sintered at 1650°C, b) RM BSZCY151020 sintered at 1650°C, c) RM BSZCY151020 w/ YSZ sintered at 1650°C, d) RM BSZCYZn1510202 w/ YSZ sintered at 1600 °C, e) RM BSZCYZn1510202 w/ YSZ sintered at 1500°C, f) RM BSZCYZn1510202 w/ YSZ sintered at 1400 °C

From the **Fig. 35**, we see that the water uptake behavior for the sample RM BSZCYZn1510202 w/ YSZ -1500°C and RM BSZCYZn1510202 w/ YSZ -1400 °C is different from the other samples in which the saturation of water uptake appears after 12 to 14 hours process. As we

discussed above, the RM BSZCYZn1510202 w/ YSZ -1400 °C did not complete the SSRS process due to the relative low sintering temperature of 1400 °C. For the sample sintered at 1500 °C, we did not observe the precursor powder in its SEM picture. However, the similar water uptake behavior tells us that both samples did not complete the SSRS process. Further analysis, thus, will focus on the rest 4 samples PM BSZCY151020-1650 °C, RM BSZCY151020 w/ YSZ-1650°C, and RM BSZCYZn1510202 w/ YSZ-1600 °C.

The water uptake process is determined by the chemical reaction at humid atmosphere, which has been described in paragraph 5 of section 2.2.3. The chemical reaction equation and its equilibrium constant are given by **Eq. 20** and **Eq. 21**, with following site restriction (**Eq. 52**) and electroneutrality (**Eq. 53**).

$$\begin{aligned} [O_{\text{O}}^{\times}] + [v_{\text{O}}^{\bullet\bullet}] + [OH_{\text{O}}^{\bullet}] &= 3 \\ [O_{\text{O}}^{\times}] &= 3 - [v_{\text{O}}^{\bullet\bullet}] - [OH_{\text{O}}^{\bullet}] \end{aligned} \quad \text{Eq. 52}$$

$$\begin{aligned} 2[v_{\text{O}}^{\bullet\bullet}] + [OH_{\text{O}}^{\bullet}] - S &= 0 \\ [v_{\text{O}}^{\bullet\bullet}] &= \frac{-[OH_{\text{O}}^{\bullet}] + S}{2} \end{aligned} \quad \text{Eq. 53}$$

where S is the effective dopant concentration $[Y'_{\text{Zr}}]$ and presents the rate of hydration.

Put **Eq. 52** in **Eq. 53**, then electroneutrality term can be expressed as,

$$[O_{\text{O}}^{\times}] = 3 - \frac{-[OH_{\text{O}}^{\bullet}] + S}{2} - [OH_{\text{O}}^{\bullet}] \quad \text{Eq. 54}$$

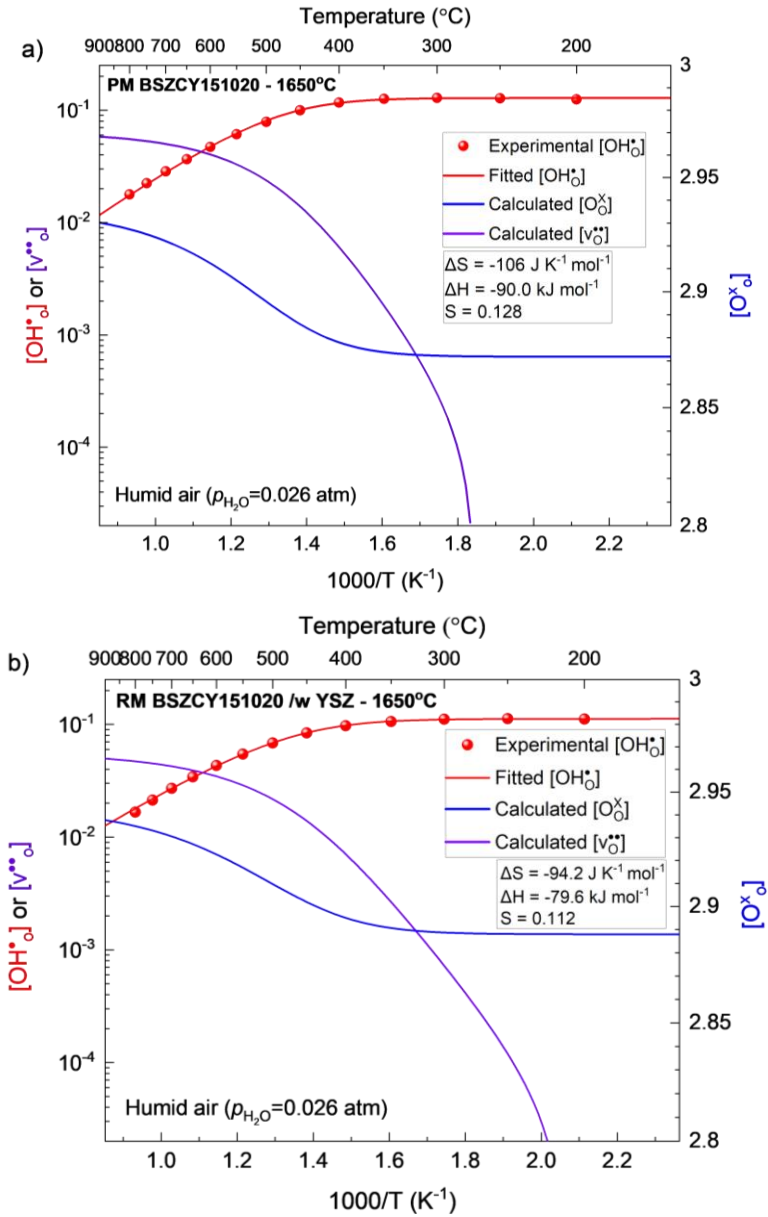
Put **Eq. 53** and **Eq. 54** in **Eq. 21** we get,

$$K = \frac{[OH_{\text{O}}^{\bullet}]^2}{\left(\frac{-[OH_{\text{O}}^{\bullet}] + S}{2}\right) \left(\frac{-[OH_{\text{O}}^{\bullet}] + S}{2} - [OH_{\text{O}}^{\bullet}]\right) p_{\text{H}_2\text{O}}} \quad \text{Eq. 55}$$

We rewrite **Eq. 55** in terms of proton concentration $[OH_{\text{O}}^{\bullet}]$,

$$[OH_{\text{O}}^{\bullet}] = \frac{3Kp_{\text{H}_2\text{O}} - \sqrt{Kp_{\text{H}_2\text{O}}(9p_{\text{H}_2\text{O}} - 6p_{\text{H}_2\text{O}}S + Kp_{\text{H}_2\text{O}}S^2 + 24S - 4S^2)}}{Kp_{\text{H}_2\text{O}} - 4} \quad \text{Eq. 56}$$

We can apply the TableCurve 2D-fitting software to fit the experimental results shown in **Fig. 35**. For example, fitting measured results for $[OH_{\text{O}}^*]$ in figure **Fig. 35** with **Eq. 56**, we can get S the concentration of effective acceptor dopant $[Y'_{Zr}]$ e.g. the amount of hydration, and temperature dependency of K (the equilibrium constant). By fitting the K temperature dependence with **Eq. 9**, we can find the process thermodynamic parameters e.g., standard entropy and enthalpy changes ΔS° and ΔH° . Moreover, we also can determine the concentration $[O_{\text{O}}^{\times}]$ and $[v_{\text{O}}^{**}]$ versus temperature respectively using **Eq. 52** and **Eq. 53**. The results are shown in **Fig. 36**, and **Table 17**.



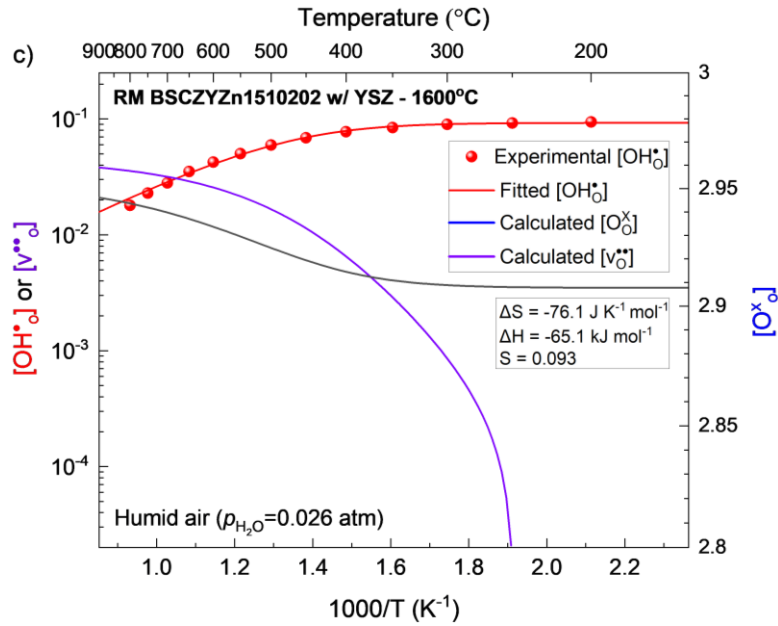


Fig. 36: Simulation results for process thermal dynamic parameters and concentrations of the different defects.

We can see that the simulation fits the experimental data very well. Below about 400 °C, the water uptake is saturated and the proton concentration $[\text{OH}_0^\bullet]$ becomes a constant for 3 analyzed samples. We also observed the significant reduction in the concentration of $v_0^{\bullet\bullet}$ below 400 °C. In humid condition at above 400 °C up to 800 °C, both oxygen vacancies and protons will contribute to the conductivity, when temperature below 400 °C, the protons dominate the conductivity in the SUT, no conductivity contribution from electrons or holes can be seen in measurement conditions.

Table 17: Results from the fitting of hydration curves

Sample	Max hydration (mol fraction)
PM BSZCY151020-1650 °C	0.128
RM BSZCY151020 w/ YSZ-1650 °C	0.112
RM BSZCYZn1510202 w/ YSZ-1600 °C	0.093

From **Table 17**, we see that the rate of hydration for PM BSZCY151020-1650 °C, RM BSZCY151020 w/ YSZ-1650 °C, and RM BSZCYZn1510202 w/ YSZ-1600 °C equals to 0.128, 0.112, and 0.093 respectively, which indicate the highest concentration of OH_0^\bullet in sample PM BSZCY151020-1650°C.

5.3.2 Conductivity of PCCs Analyzed by EIS

Samples with fired contact pads will form a capacitor configuration. The PCC as the proton conductive electrolyte makes the distinguish of the capacitor different from the electrostatic

capacitor such as ceramic capacitors. The contact resistance, the charge transfer resistance, and a double layer capacitance will be the elements for modelling the PCC capacitor. Because the PCC is a polycrystalline material, more elements will be involved to model the PCC capacitor. The EIS is a powerful tool to find the performance of the PCC capacitor and thus the properties of the PCC. By using “Novocontrol Alpha” impedance was measured from 1 MHz to 0.01 Hz using 10mV rms in various humid atmospheres at temperatures of a wide range. Different contributions to the total conductivity can be identified by the EIS results.

5.3.2.1 Temperature Dependency of EIS

For temperature dependency of conductivity, **Fig. 37**, **Fig. 38** and **Fig. 39** below, present the EIS results measured in a humid Ar atmosphere from 100 °C to 700 °C.

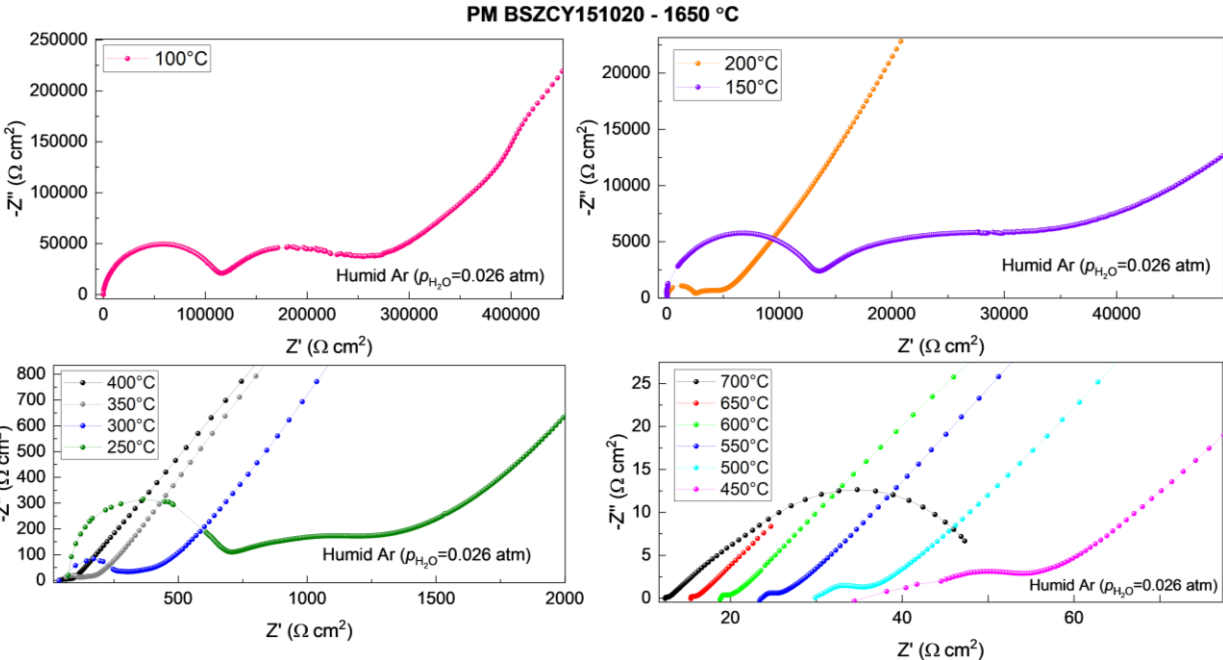


Fig. 37: EIS plots for conductivity dependency on temperature measurements on sample PM BSZCY151020 – 1650 °C

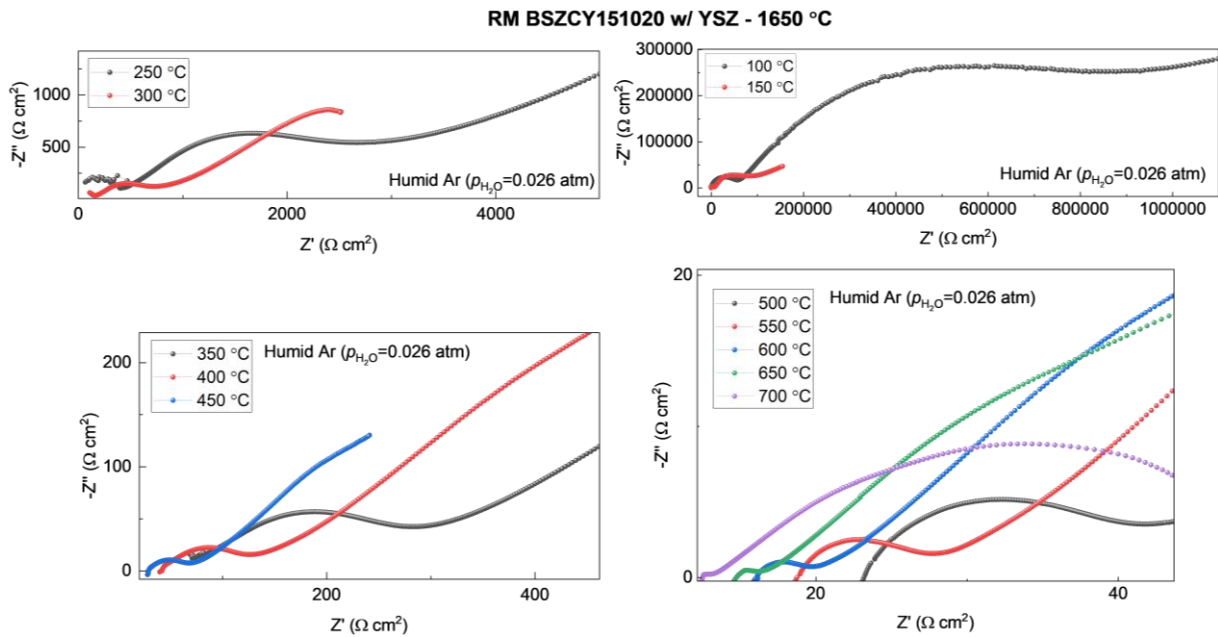


Fig. 38 : EIS plots for conductivity dependency on temperature measurements on sample RM BSZCY151020 w/ YSZ – 1650 °C

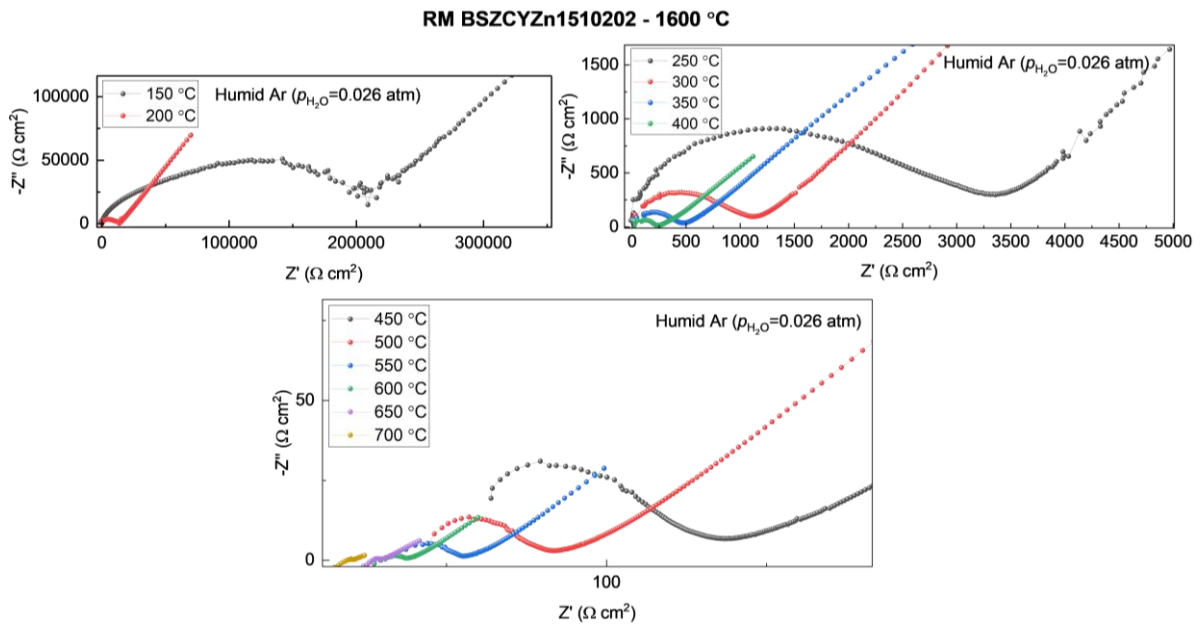


Fig. 39: EIS plots for conductivity dependency on temperature measurements on sample RM BSZCYZn1510202 w/ YSZ– 1600 °C

All three samples show that at low temperature 100 °C to 250 °C, well defined multi Randles cells can be observed. At higher temperatures (350-700 °C) only the semi-circle for grain boundary contribution is observed. The semicircles shift toward left with reduced radius when temperature increases. Therefore, the real impedance such as contact resistance, bulk resistance and the grain boundary resistance presented by specific semicircle certainly decreases with the

temperature increasing. Referring to the theory in chapter 2 and the charge carriers in the PCC in humid Ar discovered in **Fig. 36**, we can understand that the increased number of charge carriers $[\text{OH}_0^\bullet]$ and their hopping mobility with increasing temperature are the reason for low resistance of both bulk and grain boundary. The change of $[\text{OH}_0^\bullet]$ is a thermal active process and its mobility is with hopping characteristics, which can be discussed by analysing the temperature dependency of the total conductivity in the PCC.

5.3.2.2 p_{O_2} Dependency of EIS

Before we discuss the temperature dependency of conductivity, we need to confirm the charge carriers involving the conductivity in the measurement condition. For this purpose, partial pressure of O_2 dependence of EIS was measured in a humid Ar atmosphere mixed with different O_2 concentrations at 600°C . The results for PM BSZCY151020- 1650°C sample are shown below.

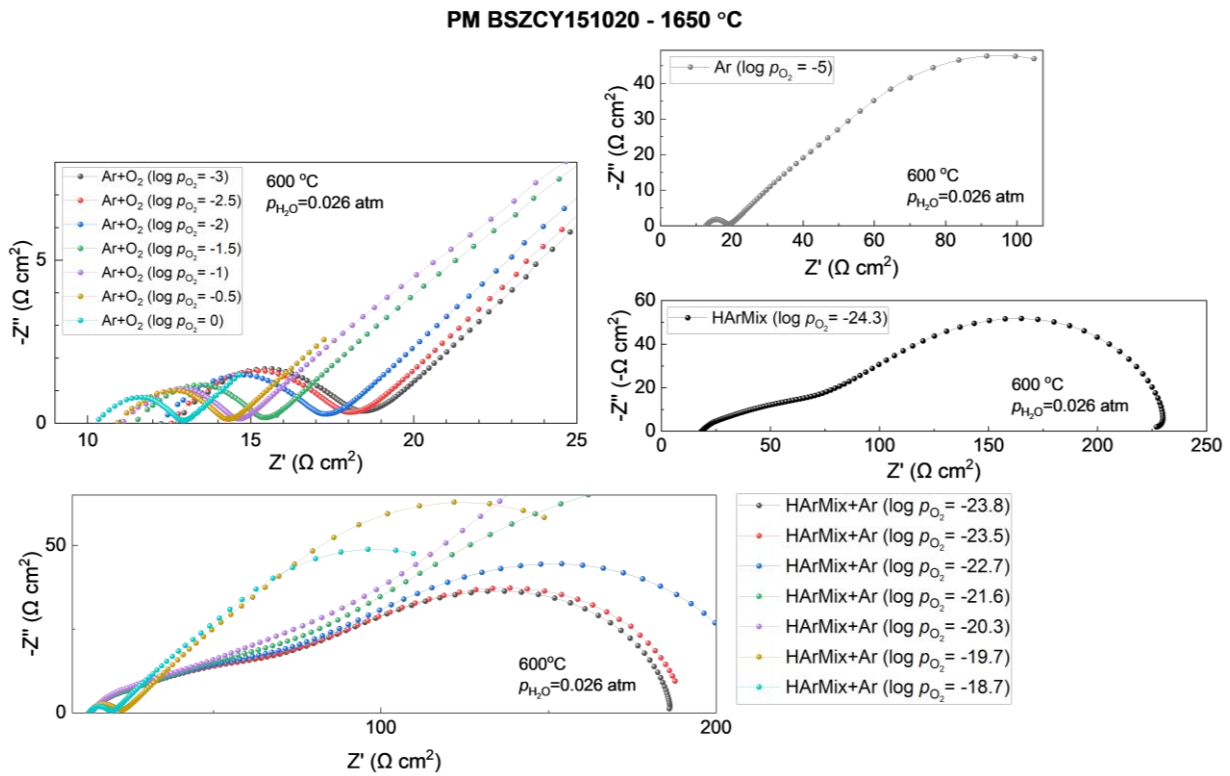


Fig. 40: p_{O_2} dependency of EIS measurements on PM BSZCY151020- 1650°C

Fig. 40 shows that the real impedance from the first semicircle reduces quickly with the p_{O_2} increases to high level, which indicates a high conductivity at high level of p_{O_2} .

5.3.2.3 Temperature Dependency of Conductivity

Based on the EIS results shown in **Fig. 37**, **Fig. 38**, **Fig. 39** and **Fig. 40**, we apply multi Randles-circuits model in combination of capacitors value identifying the specific Randles circuits, so that the measured EIS curves above can be deconvoluted, seeing plots in **Fig. 41** as an example.

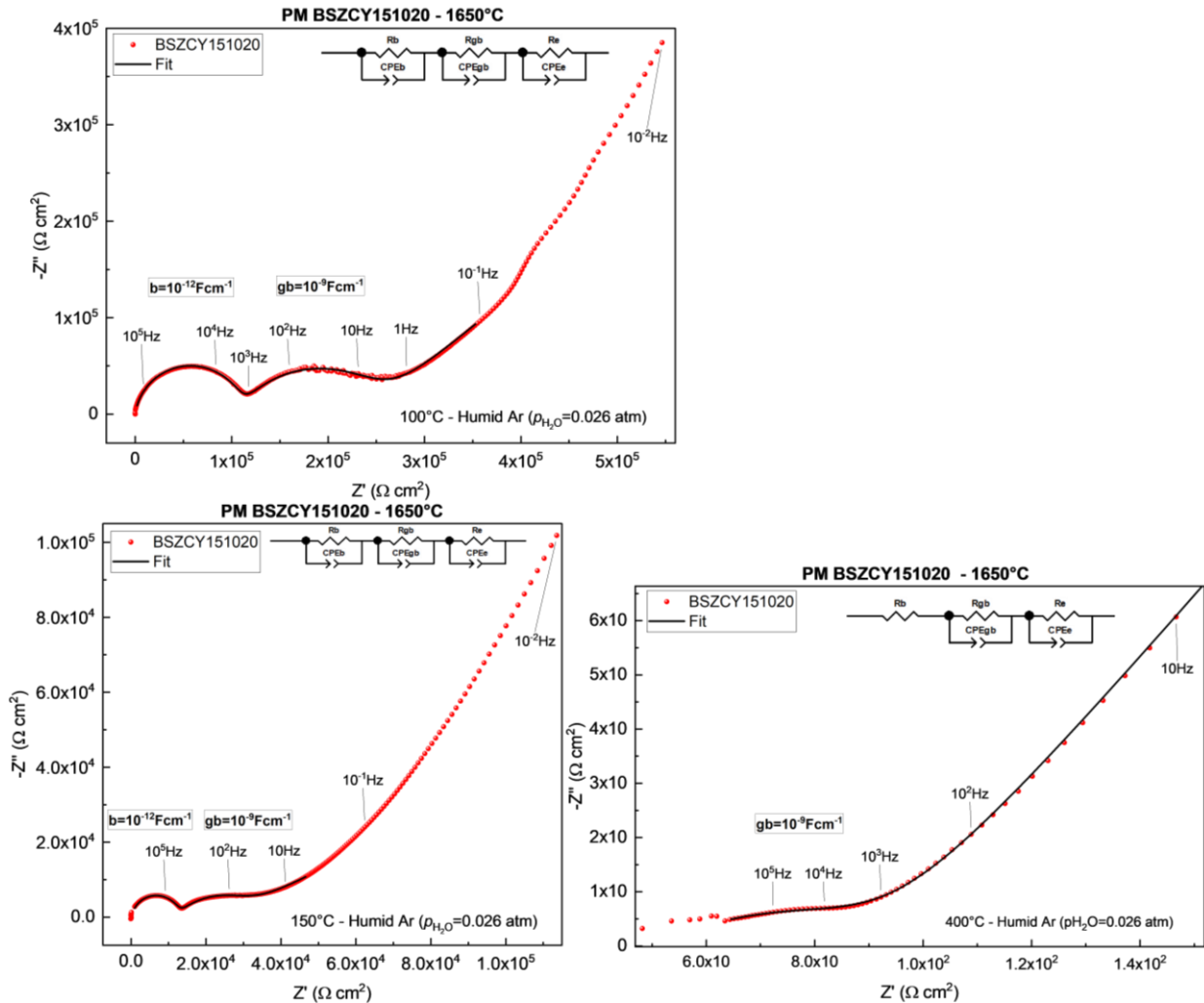


Fig. 41: Deconvolution of EIS measurements on sample PM BSZCY151020-1650 °C at 100 °C, 150 °C and 400 °C.

At low temperature, an equivalent circuit consisting of all three Randles cells are used, however at higher temperatures the bulk contribution is not well defined, thus we only report the R_b . By using this deconvolution technique, the following **Fig. 42** and **Fig. 43** for conductivity plots were achieved.

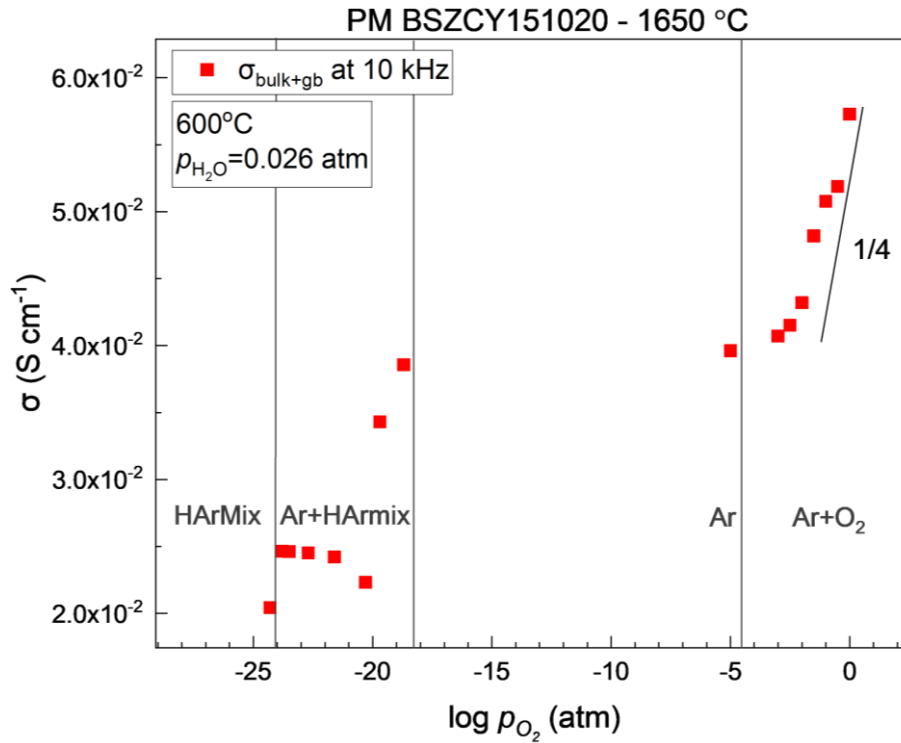
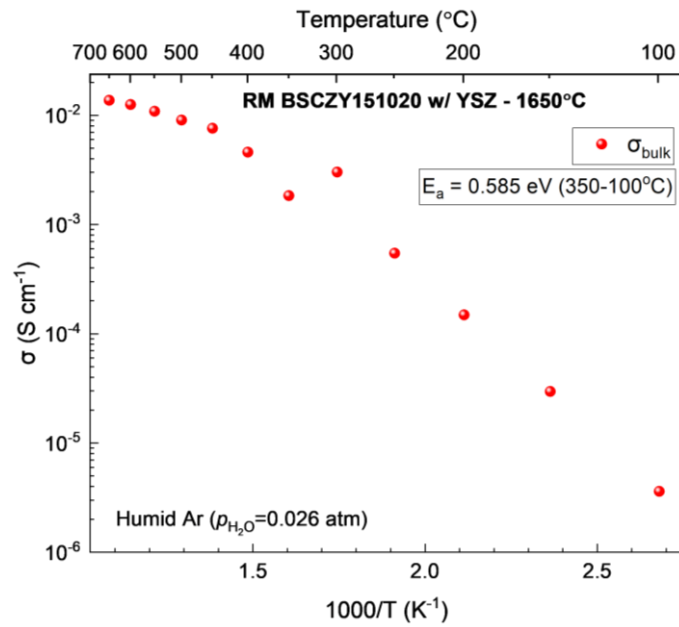
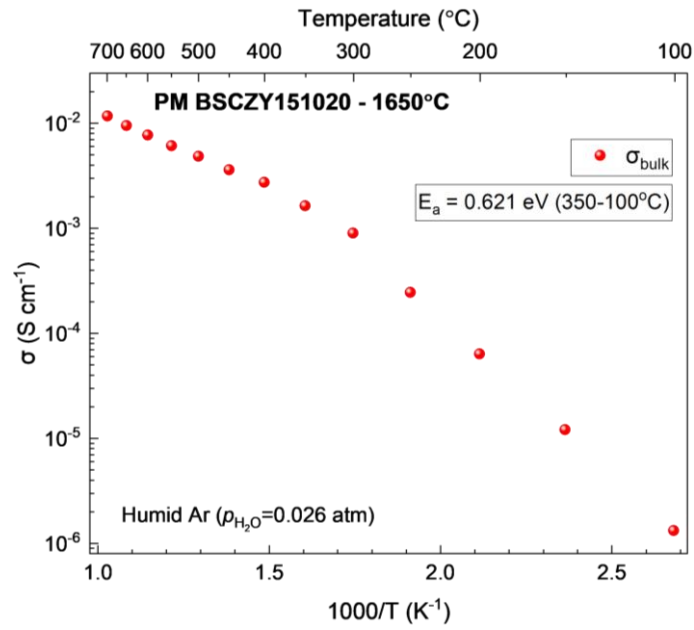


Fig. 42: The p_{O_2} dependency of conductivity at 600 °C. The sharp increase presents the hole contribution.

From p_{O_2} dependency of conductivity shown in **Fig. 42**, we see an $1/4$ increase in conductivity at higher p_{O_2} . According to the Brouwer diagram in humid atmosphere **Fig. 6** hole concentration is increasing $1/4$ at low oxygen levels (higher p_{O_2}). Knowing this we can conclude that ionic conductivity dominates in our measurement condition for temperature dependency of EIS, which were done at humid Ar without O₂. Hole conductivity is negligible. Therefore, the EIS shown in **Fig. 37**, **Fig. 38** and **Fig. 39** only involve the ionic conductivity that is deconvoluted and shown in **Fig. 42**.



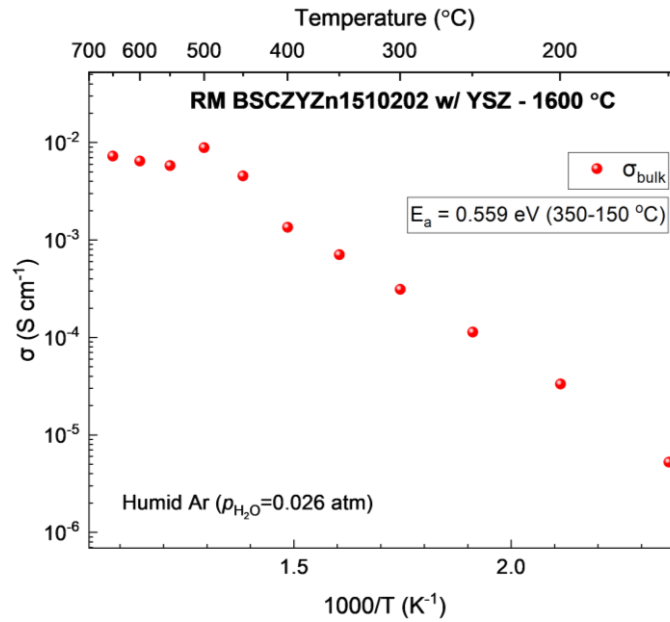


Fig. 43: The temperature dependency of bulk conductivity

From above plots in **Fig. 43**, we find that the temperature dependency of the bulk conductivity for all three samples consists of 2 linear sections marked by the red lines. One line is in the temperature range of >350 °C and the another is in the temperature range < 350 °C, which will give two different activation energies. As we see from **Fig. 36**, there are two charge carriers, e.g., $v_{O}^{\bullet\bullet}$ and OH_{O}^{\bullet} , taking part in conducting the current with different contributions at different temperatures. Considering only ionic conductivity, we fit the total conductivity $\sigma_{\text{bulk+gb}}$ obtained from EIS by using $[OH_{O}^{\bullet}]$ and $[v_{O}^{\bullet\bullet}]$ value in **Fig. 36** as inputs. The results are given in **Fig. 43**.

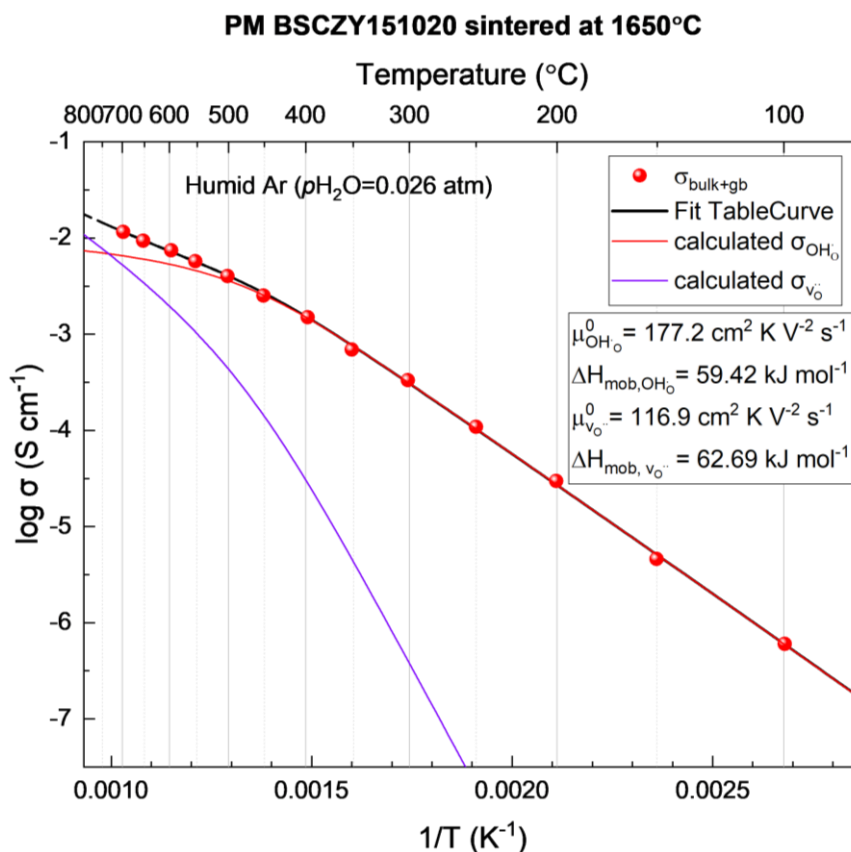


Fig. 44: Fitting of total conductivity and ionic partial conductivities

From **Fig. 44**, the fitting for total conductivity and each contribution of conductivity it is clear that both **Fig. 36** and **Fig. 44** tell us that OH_0^\bullet dominates the conductivity in the bulk PCC when temperature < 350 °C, and when temperature > 350 °C the conductivity is contributed by both OH_0^\bullet and $\text{V}_0^{\bullet\bullet}$. Therefore, the activation energy below 350 °C found from Fig. 40 is for bulk OH_0^\bullet hopping process, and above 350 °C found from Fig. 40 is meaningless because of two mixed thermal activation processes. As a summary, conductivity at different temperatures and the activation energy for bulk OH_0^\bullet hopping is summarized in **Table 18** for all samples.

Table 18: The activation energy for bulk OH_0^\bullet hopping

Sample	Bulk (eV)	Total (eV)
PM BSZCY151020-1650 °C	0.621(350-100 °C)	0.247 (700-100 °C)
RM BSZCY151020 w/ YSZ-1650 °C	0.254 (350-100 °C)	0.209 (700-100 °C)
RM BSZCYZn1510202-1600 °C	0.243 (350-150 °C)	0.239 (700-150 °C)

Table 19: Conductivity at different temperatures for sample PM BSZCY151020-1650 C, RM BSZCY151020 w/ YSZ, and RM BSZCYZn1510202 w/ YSZ-1600 C

Temp (°C)	PM BSZCY151020-1650 °C Conductivity (S cm ⁻¹)	RM BSZCY151020 w/ YSZ-1650 °C Conductivity (S cm ⁻¹)	RM BSZCYZn1510202 w/ YSZ-1600 °C Conductivity (S cm ⁻¹)
400	0.001772	0.001977	0.0008188
500	0.004085	0.005109	0.002388
600	0.007367	0.01034	0.005720

5.3.3 Transport Number by EMF

EMF measurements were done on the sample PM BSZCY151020-1650 °C in a hydrogen concentration cell. From the EMF data, we can plot the EMF vs time and EMF vs $\ln\left(\frac{p_{H_2}}{p'_{H_2}}\right)$

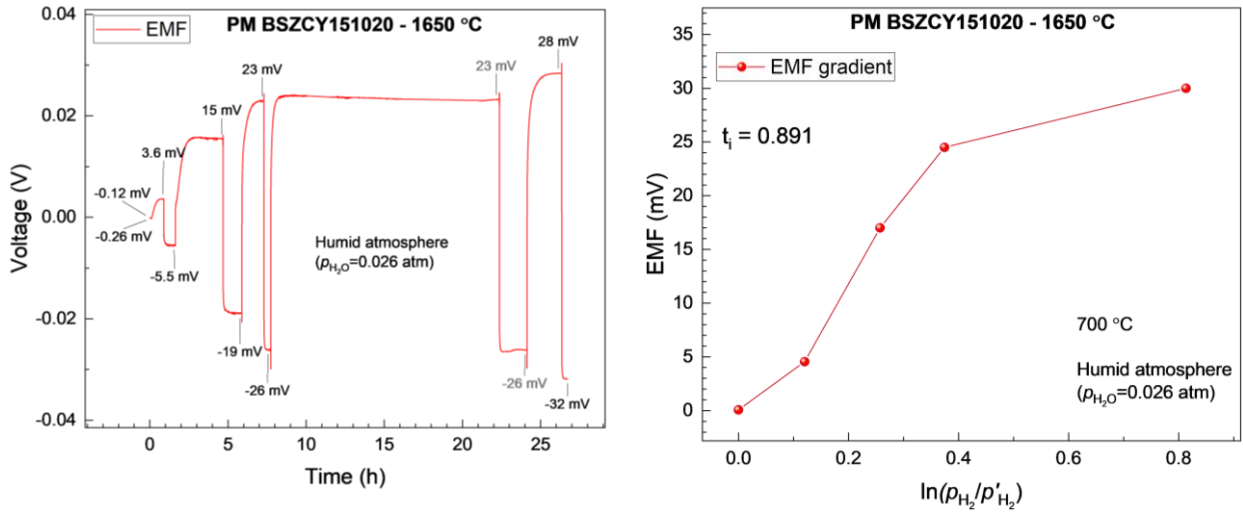


Fig. 45: EMF measurements

From the EMF vs $\ln\left(\frac{p_{H_2}}{p'_{H_2}}\right)$ plot, the transport number t_i can be found using **Eq. 49**. t_i was calculated from the slope of 5 points to be $t_i = 0.891$. This describes how much of the transported carriers are due to ionic conductivity.

The last two points in **Fig. 45 b)** show significant deviation from a linear curve, therefore, the average if the two are used when conducting linear fit on the EMF data, which gives a transport number that is closer to literature, $t_i = 1.08$ (**Fig. 46**).

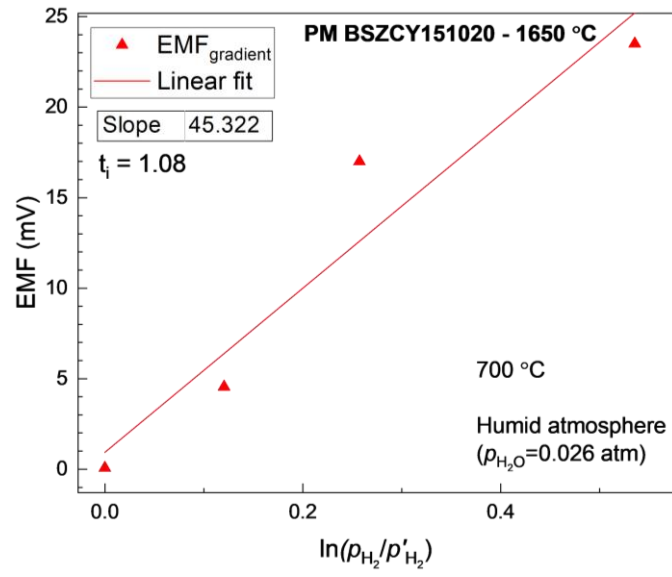


Fig. 46: Linear fit of EMF curve with corrected points

6 Summarizing Discussion

In this section, the main discoveries from the discussion above will be summarized as the following. In the thesis project, we use PXRD to ensure the sintering phase was achieved. From the diffractograms, all sintered pellets show sintered single phase. However, this was not enough to conclude whether the pellets were well sintered or not. Additional efforts were invested by doing the morphology study with SEM.

From SEM pictures of fractured and thermal etched cross-sections we observe well defined crystal grains and grain boundaries, which suggest successful sintering for pellets sintered at 1600 °C and above. For RM BSZCYZn1510202 w/ YSZ the ZnO is supposed to work as sintering aid, thus lower sintering time and temperatures should be feasible, therefore, pellets were sintered at 1400 °C, 1500 °C and 1600 °C. For samples sintered below 1500 °C, the SEM pictures show precursor powder, suggesting the pellet is not totally sintered even though the PXRD shows the sintered single phase.

DIL experiment were done on the 4 batches. This was initially for studying the sintering behavior to achieve optimal sintering profiles. However, a significant sintering shoulder were discovered for 2 of the batches without YSZ. The causes for this sintering shoulder have been investigated in more detail by combining DIL and TGA experiments of raw powders, in addition, HT-PXRD of the raw powders were done. From these experiments we have learned, the sintering shoulder must be related to ZrO₂ since this is the most significant variable, we can also say that the expansion after the sintering shoulder is due to decomposition of BaCO₃ or more precisely, CO₂ gas accumulation and exiting the sample. This CO₂ gas may also be responsible for the pinholes that can be seen in the morphology. The batches with YSZ instead of ZrO₂ had a higher success rate of sintering. We suspect that the sintering shoulder has a negative effect on sintering since it applies more stress and tension on the pellets to expand and shrink several times during sintering. Thus, we conclude that using YSZ instead of ZrO₂ and doping with ZnO as sintering aid can increase the sinter ability of our BSZCY151020.

By using TGA, the hydration of the different sintered samples was measured. From these results, different defect concentrations were obtained as a function of temperature. Using this we can get a better understanding of our conductivity measurements. As the sample is heated in the TGA experiment, the proton concentration is decreasing, while oxygen vacancy is

increasing. From our conductivity plots, we see a decrease in temperature dependency at the same temperatures. With this we conclude that the conductivity dependency starts to decrease at intermediate temperatures (350-400 C) due to the change in defect concentration.

For conductivity study, the EIS measurements were done on three samples. PM BSZCY151020-1650 C, RM BSZCY151020 w/ YSZ-1650 C, and RM BSZCYZn1510202 w/ YSZ. From the EIS data, conductivity plots were made, and the activation energy for proton hopping in bulk at low temperatures were found. The activation energy becomes lower for RM BSZCY151020 w/ YSZ-1650, and it becomes even lower for RM BSZCYZn1510202 w/ YSZ/1600. This means that by using YSZ, not only the sintering ability increases, but also the proton mobility increases. By using ZnO as sintering aid doped into the structure, the sintering temperature and time decrease, which results in an optimization of the sintering profile while increasing the charge carrier mobility. However, because of this lowered sintering time and temperature, the conductivity reduces significantly in the sample with ZnO as the sintering aid, it has the lowest conductivity value among the three samples. The reason for this can be understood by conducting TGA measurements. The sample with ZnO as the sintering aid has the lowest hydration. The low hydration means that there is less proton concentration in the sample, thus the conductivity becomes lower.

HT-PXRD results show that the TEC of sample PM BSZCY151020-1650 °C was surprisingly found to be negative. The material BSZCY151020 are not known for having negative TEC from literature review. Dayaghi et al. do find an increased TEC for the similar material [7]. Unfortunately, we did not get chance to repeat the measurements. This negative TEC temperature dependency was discussed among the group, but no conclusion could be made. Thus, we suggest that this will have to be investigated in more detail by the next master project.

7 Conclusion

In the thesis research, we have discovered a phenomenon termed “the sintering shoulder” at the heating stages of the sintering process, which may have a negative effect due to excessive shrinkage and expansion of the sample. The cause of this sintering shoulder has been analyzed in detail and is due to ZrO_2 transitioning from monoclinic to tetragonal phase at 1200 °C. By using yttria-stabilized zirconia instead of ZrO_2 in $(\text{Ba}_{0.85}\text{Sr}_{0.15})(\text{Zr}_{0.7}\text{Ce}_{0.1}\text{Y}_{0.2})\text{O}_{3-\delta}$ the sintering shoulder is eliminated resulting in less strain and stress on the sample pellets during sintering. By further doping with 2 mol% ZnO as sintering aid, the success rate of sintering green bodies was increased significantly, even when using more effective sintering profiles with lower a shorter sintering time (1600 °C for 12 hours). We also find that the solid-state reactive sintering cannot be complete in below 1600 °C within 12 hours. By using yttria-stabilized zirconia instead of ZrO_2 the activation energy for proton transport is lowered at temperatures of 100-350 °C from 0.621 eV to 0.585 eV, doping with ZnO further lowers the activation energy to 0.559 eV. The conductivity is increased for samples with yttria-stabilized zirconia, however further doping with ZnO as sintering aid lowered the conductivity due to relatively lower hydration rates. High-temperature X-ray diffraction measurements showed a negative thermal expansion coefficient, which is not expected for this kind of materials. The negative thermal expansion coefficient must be investigated in detail by the next master project.

References

- [1] R. Lindsey, "Climate Change: Atmospheric Carbon Dioxide," 14 August 2020. [Online]. Available: <https://www.climate.gov/news-features/understanding-climate/climate-change-atmospheric-carbon-dioxide>. [Accessed 26 September 2021].
- [2] R. Lindsey and L. A. Dahlman, "Climate Change: Global Temperature," 15 May 2021. [Online]. Available: <https://www.climate.gov/news-features/understanding-climate/climate-change-global-temperature>. [Accessed 26 September 2021].
- [3] NATO Advanced Study Institute Assessment of Hydrogen Energy for Sustainable Development, Assessment of Hydrogen Energy for Sustainable Development, 1st ed., J. W. Sheffield and C. Sheffield, Eds., Dordrecht: Springer, 2007, pp. 1-3.
- [4] M. Milikin, "Toyota FCV Mirai launches in LA; initial TFCS specs; \$57,500 or \$499 lease; leaning on Prius analogy," 18 November 2014. [Online]. Available: <http://www.greencarcongress.com/2014/11/20141118-mirai.html>. [Accessed 25 January 2022].
- [5] U.S Department of Energy, "Department of Energy Hydrogen Program Plan," 2020.
- [6] University of Illinois at Urbana-Champaign, "Scientists discover new way to make water," 31 October 2007. [Online]. Available: <https://phys.org/news/2007-10-scientists.html>. [Accessed 3 February 2022].
- [7] A. M. Dayaghi et al., "Increasing the thermal expansion of proton conducting Y-doped BaZrO₃ by Sr and Ce substitution," *Solid State Ionics*, no. 359, p. 1, 2021.
- [8] B. J. Kennedy, C. J. Howard, G. J. Thotogood and J. R. Hester, "The Influence of Composition and Temperature on the Phases in Sr_{1-x}BaxZrO₃ Perovskites: A High-Resolution Powder Diffraction Study," *Journal of solid state chemistry*, vol. 161 (1), pp. 106-112, October 2001.
- [9] Y. Zhao and D. J. Weidner, "Thermal Expansion of SrZrO₃ and BaZrO₃ Perovskites," *Physics and Chemistry of Minerals*, vol. 18, pp. 294-301, 2 August 1991.
- [10] S. Loidant and G. Lucazeau, "High-pressure Raman study of the perovskite BaCeO₃," *Journal of Raman Spectroscopy*, vol. 30, pp. 485-492, June 1999.
- [11] S. YAMANAKA, M. FUJIKANE, T. HAMAGUCHI, H. MUTA, T. OYAMA, T. MATSUDA, S.-I. KOBAYASHI and K. KUROSAKI, "Thermophysical properties of

- BaZrO₃ and BaCeO₃," *Journal of alloys and compounds*, Vols. 359 (1-2), pp. 109-113, 2003.
- [12] S. Nikodemski, J. Tong and R. O'Hayre , "Solid-state reactive sintering mechanism for proton conducting ceramics," *Solid State Ionics* , vol. 253, 16 September 2013.
- [13] H. Iwahara, "Technological challenges in the application of proton conducting ceramics," *Solid state ionics*, vol. 77 (C), pp. 289-298, 1995.
- [14] K. Singh, A. K. Baral and V. Thangadurai, "Grain Boundary Space Charge Effect and Proton Dynamics in Chemically Stable Perovskite-Type Ba_{0.5}Sr_{0.5}Ce_{0.6}Zr_{0.2}Gd_{0.1}Y_{0.1}O_{3-δ} (BSCZGY): A Case Study on Effect of Sintering Temperatur," *Journal of the American Ceramic Society*, vol. 99 (3), pp. 866-875, March 2016.
- [15] S. J. Madhuri, N. Murali, K. B. Vijay and V. Veeraiah, "Effect of Strontium the phase structure of Ba_{1-x}Sr_xCe_{0.65}Zr_{0.2}Y_{0.15}O_{3-δ} (0≤x≤0.25) proton conductor by citrate-EDTA complexing sol-gel method," *Journal of Asian Ceramic Societies*, vol. 5 (1) , pp. 19-30, March 2017.
- [16] M. A. Peña and J. L. G. Fierro, "Chemical Structures and Performance of Perovskite Oxides," *Chemical reviews*, vol. 101, pp. 2-3, 11 July 2001.
- [17] T. Norby, "Defects and Transport in Crystalline Materials," 2015.
- [18] B. A. Boukamp, "Electrical Impedance Spectroscopy," Enschede, 2008.
- [19] NORECS AS, "ProboStat, overview," NORECS, [Online]. Available: <https://www.norecs.com/index.php?page=Overview>. [Accessed 18 04 2022].
- [20] D. Han, X. Liu, T. S. Bjørheim and T. Uda, "Yttrium-Doped Barium Zirconate-Cerate Solid Solution as Proton Conducting Electrolyte: Why Higher Cerium Concentration Leads to Better Performance for Fuel Cells and Electrolysis Cells," *Advanced Energy Materials*, 2021.
- [21] D. S. a. S. S. Arvanitidis, "A Study of the Thermal Decomposition of BaCO₃," *Metallurgical and Materials Transactions B*, Vols. 416-Volume 27B, June 1996.
- [22] W. contributors, "Wikipedia," [Online]. Available: https://en.wikipedia.org/w/index.php?title=Zirconium_dioxide&oldid=1085196482. [Accessed 15 May 2022].

- [23] P. a. H. S. M. Babilo, "Enhanced Sintering of Yttrium-Doped Barium Zirconate by Addition of ZnO," *Journal of the American Ceramic Society*, vol. Vol.88, pp. p.2362-2368, September 2005.
- [24] NATO Advanced Research Workshop on Fuel Cell Technologies, Fuel Cell Technologies: State and Perspectives, vol. 202, N. Sammes, A. Smirnova and O. Vasylyev, Eds., Dordrecht: Springer, 2005, p. 19.
- [25] Y. G. Lyagaeva et al., "Thermal expansion of materials in the barium cerate-zirconate system," *Physics of the solid state*, vol. 57, pp. 285-289, 18 February 2015.
- [26] linseis Inc., "How does a pushrod dilatometer work?," Linseis GmbH, 2022. [Online]. Available: <https://www.linseis.com/en/wiki-en/how-does-a-pushrod-dilatometer-work/>. [Accessed 17 03 2022].
- [27] R. D. Shannon , "Revised effective ionic radii and systematic studies of interatomic distances in halides and chalcogenides," *Acta Crystallographica Section A*, vol. 32 (5), pp. 751-767, 9 January 1976.

Figures

Fig. 1: Picture of a hydrogen-powered car at Høvik hydrogen fueling station in Norway (pictured 09.04.2022, established in 2019)	3
Fig. 2: Schematic of a PCFC in operation	5
Fig. 3: C) BZY20 after sintering at 1500 °C for 12 h RD ~34.1%, B) BCZY63 after sintering at 1500 °C for 12 h RD ~60%, from the work of Nikodemski et al. [12]	7
Fig. 4: a) Vacancy, b) substitutional defect, c) host interstitial defect and d) foreign interstitial defect.	11
Fig. 5: Defect equilibrium coefficient for the defect reaction described by Eq. 10	14
Fig. 6: a) Brouwer diagram describing BZY-defects dependency on pO_2 in dry atmosphere b) Brouwer diagram describing BZY-defects dependency on pO_2 in humid atmosphere c) Brouwer diagram describing BZY-defects dependency on humidity	19
Fig. 7: Nyquist plot with equivalent circuit of a simplified Randles cell	25
Fig. 8: Typical equivalent circuit and EIS of PCC	26
Fig. 9: a) CAPCO Ball Mill Model 12VS b) Retsch® PM 100	28
Fig. 10: Picture of muffle furnaces, a) Nabertherm LVB524 b) Nabertherm HT LVB533	29
Fig. 11: NETZSCH DIL 402C Dilatometer	29
Fig. 12: Picture of XRD instruments, a) Rigaku MiniFlex600 b) RECX-DIFF5 c) RECX1	31
Fig. 13: NETZSCH STA 449 F1 Jupiter® Thermal Gravimetric Analyzer	32
Fig. 14: Picture of SEMs used in this thesis project. a) HITACHI SU8230 SEM b) FEI Quanta 200 c) HITACHI TM3000 Tabletop Microscope	33
Fig. 15: Brooks® Gas Mixer Flowmeters	33
Fig. 16: Schematic of gas mixer setup	34
Fig. 17: a) Picture of ProboStat during measurement, b) setup, c) schematic of setup	35
Fig. 18: Flowchart describing the sequence of actions done in this project	36
Fig. 19: The picture of a green body sample PM BSZCY151020.	38
Fig. 20: Plot of sintering profiles, a) PM BSZCY151020 – 1650 °C, RM BSZCY151020 – 1650 °C, RM BSZCY151020 w/ YSZ – 1650 °C, b) RM BSZCYZn1510202 w/ YSZ – 1600 °C, c) RM BSZCYZn1510202 w/ YSZ – 1500 °C, d) RM BSZCYZn1510202 w/ YSZ – 1400 °C.	40
Fig. 21: Schematic plot for the hydrogen concentration cell	49
Fig. 22: SEM picture of fractured cross-section that shows pinholes in the structure.	51
Fig. 23: Results from Dilatometer measurements on the samples, a) PM BSCZY151020, b) RM BSZCY151020, c) RM BSZCY151020 w/ YSZ, and d) RM BSZCYZn1510202 w/ YSZ.	52
Fig. 24: Diffractograms for HT-PXRD of PM BSZCY151020 - 1650°C	54
Fig. 25: XRD pattern of PM BSZCY151020 – 1650 °C and BZY pdf from the Diffraction data base	55
Fig. 26: Results from Dilatometer measurements on the samples, a) PM BSZCY151020 and b) BaCO ₃ .	55
Fig. 27: The results of operando TGA of precursor of relative green body, combining the DIL experiments of the green body.	57

Fig. 28: The concave in the DIL curve reported by Babilo et al. [23]	59
Fig. 29: PXRD pattern of all 5 samples plus XRD pattern from the data base «PDF-2 Release 2014 RDB» in Difffrac.eva software for cubic crystalline BZY	59
Fig. 30: SEM pictures of fractured cross section of the 6 samples	61
Fig. 31: SEM pictures of thermally etched cross sections	61
Fig. 32: The grain size distribution estimated by SEM of thermal etched cross-section.	62
Fig. 33: HT-XRD experimental results for sample PM BSZCY151020 – 1650 °C at temperatures from 29 °C to 1200 °C and from 1200 °C to 38 °C	66
Fig. 34: Lattice parameter of PM BSCZY151020-1650 °C versus temperature. a) measured as temperature rising, b) measured as temperature decreasing.	67
Fig. 35: Water uptake of a) PM BSZCY151020 sintered at 1650°C, b) RM BSZCY151020 sintered at 1650°C, c) RM BSZCY151020 w/ YSZ sintered at 1650°C, d) RM BSZCYZn1510202 w/ YSZ sintered at 1600 °C, e) RM BSZCYZn1510202 w/ YSZ sintered at 1500°C, f) RM BSZCYZn1510202 w/ YSZ sintered at 1400 °C	69
Fig. 36: Simulation results for process thermal dynamic parameters and concentrations of the different defects.	72
Fig. 37: EIS plots for conductivity dependency on temperature measurements on sample PM BSZCY151020 – 1650 °C	73
Fig. 38 : EIS plots for conductivity dependency on temperature measurements on sample RM BSZCY151020 w/ YSZ – 1650 °C	74
Fig. 39: EIS plots for conductivity dependency on temperature measurements on sample RM BSZCYZn1510202 w/ YSZ– 1600 °C	74
Fig. 40: pO_2 dependency of EIS measurements on PM BSZCY151020-1650°C	75
Fig. 41: Deconvolution of EIS measurements on sample PM BSZCY151020-1650 °C at 100 °C, 150 °C and 400 °C.	76
Fig. 42: The pO_2 dependency of conductivity at 600 °C. The sharp increase presents the hole contribution.	77
Fig. 43: The temperature dependency of bulk conductivity	79
Fig. 44: Fitting of total conductivity and ionic partial conductivities	80
Fig. 45: EMF measurements	81
Fig. 46: Linear fit of EMF curve with corrected points	82

Tables

Table 1: Volumetric TEC of SrZrO ₃ , BaCeO ₃ and BaZrO ₃	6
Table 2: Linear TEC of SrZrO ₃ , BaCeO ₃ and BaZrO ₃	6
Table 3: Boundary conditions at different atmospheres.	17
Table 4: The samples investigated in this thesis project	37
Table 5: Information about the precursors	37
Table 6: Temperature profiles for sintering of the four samples.....	38
Table 7: Temperature Profile for DIL experiments	41
Table 8 : Temperature Profiles	41
Table 9: Program for PXR experiment	42
Table 10: Program for HT-PXR experiment.....	43
Table 11: Temperature profile for HT-PXR.....	43
Table 12: Temperature profiles for water uptake experiments	44
Table 13: Temperature profiles for TGA experiments on raw powders.	45
Table 14: Initial Values and Results.....	52
Table 15: Sample densities before and after sintering	62
Table 16: Lattice parameter extracted from refinement	64
Table 17: Results from the fitting of hydration curves	72
Table 18: The activation energy for bulk OHO • hopping.....	80
Table 19: Conductivity at different temperatures for sample PM BSZCY151020-1650 C, RM BSZCY151020 w/ YSZ, and RM BSZCYZn1510202 w/ YSZ-1600 C	81